A PROBABILITY BASED UNIFIED MODEL FOR PREDICTING ELECTRICAL, MECHANICAL AND THERMAL CHARACTERISTICS OF STRANDED OVERHEAD-LINE CONDUCTORS

By

VISNJA FILIPOVIC-GLEDJA, Dipl. Eng.

A Thesis

Submitted to the School of Graduate Studies

in Partial Fulfilment of the Requirements

for the Degree

Doctor of Philosophy

McMaster University

UNIFIED MODEL FOR STRANDED OVERHEAD-LINE CONDUCTORS

DOCTOR OF PHILOSOPHY (1997)
(Electrical and Computer Engineering)

McMaster University
Hamilton, Ontario

TITLE: A Probability Based Unified Model for Predicting Electrical, Mechanical and Thermal Characteristics of Stranded Overhead-line Conductors

AUTHOR: Visnja Filipovic-Gledja, Dipl. Eng. (University of Sarajevo)

SUPERVISOR: Dr. Raymond D. Findlay

NUMBER OF PAGES: xxii, 168

ABSTRACT

This thesis is a report on a Unified Model to predict the performance of Aluminum Conductor Steel Reinforced (ACSR). The Model combines electromagnetic, mechanical, radial conduction, and steady-state thermal models, and uses a probabilistic method to take account of system loads and the stochastic nature of the meteorological parameters. The four models, developed during the past thirty years, have been used by the industry individually to predict the electrical, mechanical and thermal behaviour of stranded overhead conductors. Each aspect was analyzed separately, neglecting dependencies of the involved variables on other aspects of the conductor behaviour. Most results obtained in this way were acceptable while conductors were operating at lower temperatures. However, at high temperatures, the effects that each aspect of the behaviour has on another are no longer negligible. Until now there has not been a feasible mechanism to link the models in order to predict all aspects of the behaviour of the conductor simultaneously, and to take into consideration all the interdependent influences among models.

The Unified Model, developed as a result of this work, is a new approach for the simultaneous prediction of all the aspects of conductor behaviour. For the first time all four models: electromagnetic, mechanical, steady-state thermal, and radial conduction models, are coupled such that the conductor is viewed as a whole.

In addition, the statistical distribution of system loads, ambient temperature, and

rise of conductor temperature above ambient are included in the Unified Model to determine a realistic thermal history of the conductor and to assess annealing in the aluminum layers. This has not been done before. The usefulness of the probability based Unified Model for predicting characteristics of the conductor, such as sag, power loss and loss of tensile strength of nonferrous wires is demonstrated.

An example of application of the Model to an ACSR conductor is given. The results are used to study the sensitivity of the electrical, mechanical, and thermal characteristics of the conductor to various parameters and to determine how the electrical, mechanical, and thermal characteristics affect each other. The results are presented in the form of recommendations for the design of the overhead conductors.

ACKNOWLEDGMENTS

I would like first and foremost to thank my supervisor, Dr. Raymond Findlay for his guidance, support, patience, and understanding at different stages of this work. I would also like to thank to Dr. Vincent Morgan for his invaluable help and guidance throughout the course of this research.

I thank all my friends and colleagues at McMaster, who have made the time spent here most enjoyable. Their zeal and endeavour have been contagious.

I thank my husband and my family for all their understanding and support.

TABLE OF CONTENTS

LIST OF FIGURES

LIST OF TABLES

NOMENCLATURE

A	contact area (m^2)
A_{al}	aluminum crossectional area (m^2)
A_g	area of the air gaps (m^2)
A_m	area of true metallic contacts (m^2)
$A_{qn(n+1)}$	apparent area of each contact (m^2)
A_S	steel crossectional area (m^2)
A_t	actual total area of the contact (m^2)
A_v	area of voids (m^2)
B	half of the span (m)
CRP_A	aluminum strain (m/m)
CRP_S	steel strain (m/m)
d	wire diameter (m)
D	overall diameter of conductor (m)
D	sag (m)
D_n	outer diameter of layer n (m)
D_p	outer diameter of layer p (m)
DT_A	thermal elongation of aluminum (m/m)
DT_S	thermal elongation of steel (m/m)

E	actual arc elongation (m/m)
E_A	aluminum modulus of elasticity (MPa)
E_S	steel modulus of elasticity (MPa)
F	ground with albedo
F_m	total radial force in layer n (N)
F_m'	total radial force on the wires in layer n (N)
F_{rqn}	radial force per contact (N)
f_y	compressive yield stress (Pa)
g	acceleration due to gravity (m/s^2)
Gr	Grashof number
Gr.Pr	Rayleigh number
Gr_{lim}	limiting Grashof number
h	heat transfer coefficient ($Wm^{-2}K^{-1}$)
H	microhardness of the softer material (Pa)
H	magnetic field of the conductor (A/m)
H	height above sea level (m)
H	horizontal component of tension (N)
h_g	conductive heat transfer coefficient for the air gaps between asperities ($Wm^{-2}K^{-1}$)
h_m	conductive heat transfer coefficient for metal-metal contacts ($Wm^{-2}K^{-1}$)
H_n	magnetic field strength produced by current in layer n (A/m)
H_S	solar altitude (deg)

h_v	conductive heat transfer coefficient for the air voids ($Wm^{-2}K^{-1}$)
I	total current (A)
I_0	extraterrestrial intensity of solar radiation (W/m^2)
I_B	intensity of solar radiation normal to the beam (W/m^2)
I_{B0}	intensity of the direct beam (W/m^2)
I_d	intensity of the diffuse sky radiation (W/m^2)
I_n	current in layer n (A)
k	thermal conductivity ($Wm^{-1}K^{-1}$)
k_{ion}	factor related to thermal diffusion
k_{ln}	length factor
L	conductor length (m)
L_0	unstressed conductor length at room temperature (m)
L_{nn}	self inductance (H/m)
m_n	number of the wires in layer n
N	number of conductor layers
N	day of the year
N_S	clearness ratio
Nu	Nusselt number
P	average conductor tension (N)
P_{con}	heat losses due to convection (W/m)
P_{ion}	heating due to ionization (W/m)
P_J	Joule or resistive heating (W/m)

P_n	power gain layer n (W/m)
p_q	mean pressure over apparent area (Pa)
Pr	Prandtl number
P_R	heat losses due to radiation (W/m)
P_S	solar heat gain (W/m)
P_W	heat losses due to evaporation (W/m)
q	number of contacts
R_{AC}	ac resistance per unit length (Ω/m)
Re	Reynolds number
Re_{eff}	effective Reynolds number
Re_{eq}	equivalent Reynolds number
Re_{lim}	limiting Reynolds number
R_n	dc resistance of the layer n (Ω/m)
s_n	lay length of the layer n (m)
ST_A	settlement strain in aluminum (m/m)
ST_S	settlement strain in steel (m/m)
t	time (year)
T	conductor temperature (°C)
T^*	absolute temperature (K)
T_A	aluminum temperature (°C)
T_{amb}	temperature of the ambient (°C)
tan θ	mean slope of the asperities

t_{eq}	equivalent time (year)
T_f	film temperature (°C)
T_{gr}	ground temperature (°C)
T_S	steel temperature (°C)
T_{sky}	sky temperature (°C)
T_{sur}	temperature of the surface of the conductor (°C)
T'	total axial tension (N)
U	wind velocity (m/s)
W	conductor weight per unit length (N/m)
W	loss of tensile strength (%)
W_a	loss of the strength in the fully-annealed state (%)
X	total strain (m/m)
X_A	total strain of the aluminum (m/m)
X_{nn}	self reactance (Ω/m)
X_{pq}	mutual reactance from layer q to an inner layer p (Ω/m)
X_S	total strain of the steel (m/m)
Y	separation distance between the mean lines of two surfaces in contact (m)
α_S	absorptivity of the conductor surface for short-wave radiation
β_n	angle of lay of wires in layer n (deg)
γ_L	azimuth of the conductor axis (deg)
γ_S	azimuth of the sun axis (deg)
δ_S	declination of the sun (deg)

Δt	time interval (year)
δ_v	effective length of the void (m)
ϵ_S	emissivity of the conductor
ζ	angle of conductor inclination to the horizontal (deg)
η	angle between the solar beam and the axis of the conductor (deg)
λ_f	thermal conductivity of the air at the surface of the conductor (W/mK)
μ_0	permeability of free space (H/m)
μ_s	relative magnetic permeability of the steel (H/m)
ν_0	kinematic viscosity of air at sea level (m^2/s)
ν_H	kinematic viscosity at the altitude H (m^2/s)
ρ	resistivity of the material of the layer (Ωm)
σ	r.m.s. height of the asperities (m)
$\sigma\psi$	standard deviation of mean angle of attack of the wind (deg)
σ_A	aluminum axial stress (MPa)
σ_B	Stefan-Boltzman constant (5.66997×10^{-8} $Wm^{-2}K^{-4}$)
σ_S	steel axial stress (MPa)
ϕ	angle between the natural and forced flows (deg)
ψ^*	effective mean angle of attack (deg)
ψ_{mean}	mean angle of attack of the wind with respect to the conductor axis (deg)
Ψ_n	longitudinal flux produced by current in layer n (Wb)
$\Psi_{n,INNER}$	inner circular flux of the aluminum layer n (Wb)
$\Psi_{n,OUTER}$	outer circular flux of the aluminum layer n (Wb)

ω	angular velocity $2\pi f$ (rad/s)
ω_s	hour angle of the sun (deg)
φ	geographical latitude north positive (deg)

CHAPTER 1

INTRODUCTION

1.1 BACKGROUND INFORMATION

The demand for electric power, still growing in developed countries, is rapidly increasing in third world countries. Bare overhead lines are the most economical means for the transportation from the generation site to the consumer. However, financial and environmental constraints often restrict the construction of new transmission lines. Additionally, the length of time to obtain permissions and for construction may add to the cost.

During the last fifteen years environmental concerns such as the impact of overhead power lines on the landscape and flora and fauna have focused public attention on the problem, resulting in impediments to right of way. Also, widened urban area right of way can represent a severe obstacle for the planning of the new transmission lines. It has become essential for utilities to fully utilize existing lines and to increase their load transmission capacity. In addition, deregulation with the inevitable competition between providers, resulting in smaller marginal costs, has increased the need to minimize both capital and maintenance costs of new lines, and to increase their efficiency as well. The load capacity, capital and maintenance cost, and the efficiency of the overhead line are greatly determined by the behaviour of the overhead line conductor.

Safety and reliability of the line depends also on the performances of the conductor.

Standard overhead conductors consist of stranded conductors wrapped in layers helically around a core, which may be either steel or a metal alloy, Fig. 1. Materials which are usually used in conductors are aluminum, aluminum alloys, and steel. Copper has been rarely used because of its price. Conductors are made from one or more materials. The monometallic conductors consist of strands that are helically wrapped about the core, which is a single strand made from the same material as the outer strands. Bimetallic conductors usually consist of the layers of the conducting material, such as aluminum and aluminum alloy, wound around the core made from the reinforcing material, such as steel, aluminum clad steel or aluminum alloy. For increased efficiency the reinforcing material is usually placed in a core. However, some specially designed conductors may have reinforcing strands mixed with the conducting strands in the outer layers.

The most commonly used standard overhead conductor is aluminum conductor steel reinforced (ACSR). This bimetallic conductor consists of one or more aluminum layers wound alternatively right and left handed around the steel core. The steel core may have from one strand to several layers wound alternatively right and left-handed over the king wire, which is the centre steel strand. The steel core reinforces the conductor and enables greater tension, and consequently longer spans of the conductor. In addition, the presence of the core increases the conductor diameter and thus decreases the corona

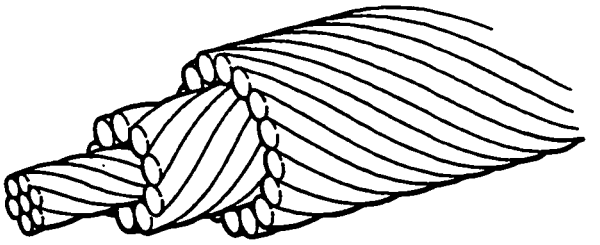

Figure 1 Stranded overhead conductor

effects at high voltages. However, as the increase of the diameter results in larger wind and ice loads we must seek means to minimize the effect.

The maximum load capacity of an overhead line is greatly determined by the maximum temperature of the conductor, the sag, and the loss of tensile strength of the nonferrous part of the conductor. Efficiency of the line depends on power losses in the conductor, which are determined by the ac resistance of the conductor. Capital and maintenance costs are greatly determined by the maximum sag, the forces in the conductor, and the loss of tensile strength of the nonferrous part of the conductor. Safety is determined by the maximum sag of the conductor, often reached at maximum temperature. Reliability of the line depends on the loss of tensile strength of the nonferrous part of the conductor.

When load capacity is considered, overhead lines can be divided into long and short lines. The load capacity of long lines depends mostly on system stability, voltage drop and energy losses. The load capacity of shorter lines is limited by the maximum permissible conductor temperature, the sag, and the long-term loss of tensile strength of the nonferrous part of the conductor due to annealing. Bigger load demands very often require transportation of the energy from remote power plants to the consumers by long transmission lines. However, the development of national and continental networks and increasing numbers of substations and interconnections in North America and Europe have increased the number of the short lines compared to longer ones. Today, the majority of overhead lines in North America are short lines.

Such factors as temperatures, sag, loss of tensile strength due to annealing, and power losses have to be determined to predict the load transfer. In this way shorter lines

can be reliably designed. Longer lines, subject to additional constraints, can also be designed to a large extent. At the same time these thermal, mechanical, and electrical characteristics of the conductor determine important performances of both short and long lines, such as the efficiency, cost, safety, and reliability.

1.2 PREVIOUS WORK

Four separate models have been developed during the past thirty years to predict the electrical, mechanical and thermal aspects of the behaviour of stranded conductors.

The Electromagnetic Model, which is particularly applicable to ACSR conductors, has been developed by Morgan and Price [1] and Barret *et al* [2]. The model gives a method for the calculation of ac resistance of the conductor and current redistribution within the conductor. Contrary to the traditional approach, which views the ACSR conductor as a hollow tube and adds skin and proximity effects and core loss to the dc resistance, this model calculates ac resistance considering the longitudinal and circumferential magnetic fields which take account of transformer effect, hysteresis and eddy current losses. Input values are the geometry of the conductor, the electrical and magnetic properties of the ferrous and nonferrous materials, the total current and the layer temperatures. Output variables are the complex layer currents and the ac resistance.

The Mechanical Model has been progressively developed by a number of authors [3-8]. Total elongation of the conductor due to the creep over a certain period of time is predicted based on the known or assumed load history. The forces in a conductor and the sag are then calculated for the given temperature. Input variables are the geometry

of the conductor, the physical properties of the materials, and the time distribution of the loads and temperature. Output variables are the strain, the sag, and the total creep. The model predicts compressive stress in aluminum wires at higher temperatures, and the risk of bird-caging, i.e. the separation of a layer of wires from its neighbours.

The Radial Conduction Model has been developed by Morgan and Findlay [9,10]. This model calculates the radial temperature distribution within stranded conductors. Input variables are the geometry of the conductor, the tension, the layer currents and resistances, and the yield stress of the nonferrous wires. Output variables are the radial forces, the power loss, and the temperature differences between layers, and the contact areas of the wires in adjacent layers.

The Steady-State Thermal Model has been progressively developed over many years, but its present form is mainly attributable to Makhlin [11], House and Tuttle [12], Webs [13], and Morgan [14-16]. The model calculates the conductor temperature when the conductor current and atmospheric data are known, or the thermal rating when the conductor temperature is given. Input variables are the geometry of the conductor, the current or the conductor temperature, the resistance, and the atmospheric variables, such as wind speed and its direction and the intensity of solar radiation. Output variables are the surface temperature of the conductor, if the current is input, or the current, if the surface temperature is the input.

In addition to the electrical, mechanical, and thermal characteristics of the conductor which are defined by four models, a very important aspect of behaviour of the conductor which has to be considered is the loss of tensile strength of nonferrous wires due to cumulative annealing. The method for calculating the loss of tensile strength of

the nonferrous wires and stranded conductors due to annealing is developed by Morgan [17]. The method calculates the reduction of the tensile strength of the conductor when it operates at higher temperatures over a certain period of time for a known thermal history. Inputs are the time distribution of the temperature and the temperature. Output is the percentage loss of the tensile strength of the nonferrous wires.

A combination of the first three models was first used to calculate the temperature distribution in a 54/6/3.5 mm + 1/3.675 mm Olive ACSR conductor on an outdoor test line [18].

1. 3 PROBLEM DESCRIPTION

In order to fully utilize transmission and distribution lines, it is important to determine accurately all aspects of the behaviour of the conductor at high temperatures pertaining to the maximum expected load transfers during the lifetime of the conductor.

Each of four models contains a number of variables, and some of these variables are common to two or more of the models. Some variables depend on the variables from the other models, others on the variables in the same model. However, each of the models is used separately, neglecting other aspects of the behaviour of the conductor and their influence on the variables used in a particular model. The Electromagnetic Model assumes that the temperatures of all layers are the same. The Radial Conduction Model usually neglects the differences between the stresses in steel and aluminum layers and the differences in power losses in layers. Both the Mechanical Model and the method for calculating the loss of tensile strength of the nonferrous wires of the conductor do not account for the different layer temperatures.

Introduced simplifications lead to approximate determination of the characteristics of the conductor, which is particularly important at high temperatures, as the errors in the model become more significant. Hence, the design of overhead line conductor is usually undertaken in a rather piecemeal fashion.

The calculation of the loss of tensile strength of the nonferrous wires of the conductor is often neglected in design practice. Besides, for both the Mechanical Model and the calculation of the loss of tensile strength, the thermal history of the conductor has to be known. It can be monitored or assumed. Often when the conductor history is not known, the calculation of the permanent elongation of the conductor is based on the assumption that the conductor is at maximum load for some percentage of time, for some time at high temperature accepted as maximum conductor temperature, and the rest of its lifetime at mean daily temperature, without additional loadings. These arbitrary assumptions often predict smaller permanent elongation of the conductor and loss of tensile strength due to annealing than actually occur.

1.4 PRESENT WORK AND CONTRIBUTIONS

In this research, all four models are combined for the first time in the Unified Model. The method for calculating the cumulative loss of tensile strength due to annealing is incorporated in the Mechanical Model. The Unified Model predicts the electrical, mechanical and thermal characteristics of the conductors taking all the interdependences between the numerous variables into consideration. The model is particularly applicable to ACSR conductors because it incorporates the Electromagnetic Model which predicts the electrical behaviour of ACSR conductors. The procedure,

however, is applicable to other types of overhead conductors.

In addition to the combination of the four separate models, the probabilistic approach is employed to take account of the thermal history of the conductor. The conductor temperature depends on the system current, ambient temperature, and other meteorological parameters, such as wind speed and direction, and intensity of solar radiation. The wind speed and direction and the intensity of solar radiation determine the temperature rise of the conductor above ambient temperature. The conductor history can be determined taking into account the statistical distribution of these factors. Instead of the conventionally assumed short period at maximum temperature and the rest of the exposure time at everyday temperature, statistical distribution of the conductor temperature over the exposure period is calculated from the statistical distribution of typical loads with large systems [19], [20], normal distribution for the probability density function of ambient temperature [16], [21], and bimodal probability density function of the temperature rise of the surface of the conductor [22].

The Unified Model enables accurate prediction of electrical, mechanical, and thermal characteristics of the conductor. It explains for the first time how each aspect of the behaviour influences the others, and gives use to mechanisms for conducting various sensitivity analyses. It introduces the loss of tensile strength due to annealing as a criterion for the design of the conductor. The Model can be readily used to optimize overhead lines and to improve the characteristics of new conductors. The Unified Model is a basis for the development of powerful software that will greatly improve design practice.

This thesis gives the model which predicts all aspects of the behaviour of the

conductor with probabilistic approach to determine conductor thermal history. The Unified Model is used to determine the effects of various parameters on the current rating and the sag of a 54/3.77 mm + 19/2.27 mm ACSR conductor Grackle. In addition, the influence of miscellaneous variables coupled through the Unified Model and their dependencies is analyzed.

1.5 THESIS CONTENTS

Chapter two describes details of the existing models. The Electromagnetic, Mechanical, Steady-State Thermal, and Radial Conduction Models and the method for the calculation of the loss of tensile strength due to annealing are reviewed. The evolution of the models and the theoretical procedures with the explanations are given. The advantages, disadvantages, and limitations of the separate models are discussed. Some directions for further development are also pointed out. Chapter three describes the Unified Model. Interdependences among variables in the four models are shown, the couplings between the four models are defined, and assumptions introduced in each model are explained. The probabilistic approach employed in the Unified Model is described.

The Unified Model is presented and discussed together with all the adjustments and linkages in the separate models necessary for their implementation within the Unified Model. Specific details for the conductor used for the application of the Unified Model are also given. Chapter four contains the results of the application of the Unified Model to an ACSR conductor. The influence of various parameters on the electrical, mechanical, and thermal behaviour of the conductor is examined. Chapter five deals

with the discussion of the results obtained by the Unified Model. The influence of various parameters on the electrical, mechanical and thermal characteristics of the conductor are examined and the relations among different aspects of behaviour analyzed. A comparison of the results with the conventional approach is also included. Chapter six summarizes the work done in this thesis. It also includes some recommendations for the design of overhead line conductors. Suggestions for future work related to separate models as well as the Unified Model are given.

CHAPTER 2

EXISTING MODELS

2.1 ELECTROMAGNETIC MODEL

The resistance of a conductor carrying alternating current is higher than its dc resistance. For monometallic and bimetallic conductors with a core other than steel, that increment is attributed to skin and proximity effect. Ever since the tests and analyses by Kennelly, Laws and Pierce [23], Kennelly and Affel [24], Zaborszky [25], and Dwight [26] showed that the skin effect factor for stranded conductors is very close to that of solid conductor, the ac resistance of stranded monometallic conductors has been calculated using formulas for the skin-effect published by H.B. Dwight [26] and graphs based on these formulas prepared by Lewis and Tuttle [27].

The ac resistance of ACSR conductors is traditionally based on the assumption that the conductor is a hollow solid tube with the inner diameter equal to the diameter of the steel core. The dc resistance at the temperature of the conductor is then corrected for the skin and proximity effect. For single layer ACSR ac resistance is usually obtained from tables and curves that show test results at various load currents [28]. For conductors with an odd number of aluminum layers larger than one, a correction factor for core loss is also applied.

A more accurate electromagnetic model for the prediction of electrical

characteristics of ACSR conductors has been developed by Barret *et al.* [2]. It is a continuation and improvement of the model given by Morgan and Price [1]. Barret's model introduces the complex magnetic permeability to take account of core losses and their effect on the current redistribution in aluminum layers. Moreover, the inductances due to circular flux are calculated in a different way. The model showed very good agreement with test results for single, two layer, and three layer ACSR conductors.

In ACSR conductors the helical stranding of aluminum wires forms a magnetic field in the steel core, which carries only a small portion of the total axial current, approximately 2 %. The current carried by aluminum wires, according to Morgan [29], Findlay [30], and Findlay and Riaz [31], follows the helical path of the conductors with very little interstrand leakage. The magnetic field in the steel core strands caused by a particular aluminum layer is proportional to the layer current and the lay length. As the succeeding layers are wound in opposite directions, the magnetic field strength due to odd and even layers have different signs. In the steel core of even-number the magnetic fluxes for most designs cancel, resulting in a negligible axial magnetic flux in the core. For an odd number of layers however, the magnetic field in the core can be substantial.

The resultant magnetic field causes magnetic losses in the steel core due to eddy currents and hysteresis. Eddy current losses are induced mainly by the longitudinal flux produced in the core strands by the currents in the aluminum layers. Hysteresis losses are caused by the magnetic domain reorientation within the core. Furthermore, the magnetic field in the core causes the current redistribution in the aluminum layers to redistribute closer to the core. The fact that the current density is not the highest near the outer surface of the conductor, as predicted by skin effect only was noticed by

Morgan and Price [1], Findlay [30], and Findlay and Riaz [31].

The Electromagnetic Model defines the conductor as a combination of resistances, inductances due to longitudinal flux, and inductances due to circular flux, as shown in Fig. 2. It is assumed that the layer currents follow helical paths and produce longitudinal and circular magnetic fields. A complex magnetic permeability is used to describe the behaviour of the steel core. Its imaginary component takes account of the core losses induced mainly by longitudinal flux. The total voltage drop over the conductor is the same for every layer. The core losses produce a voltage drop across the longitudinal inductance in each layer and increase the layer resistance.

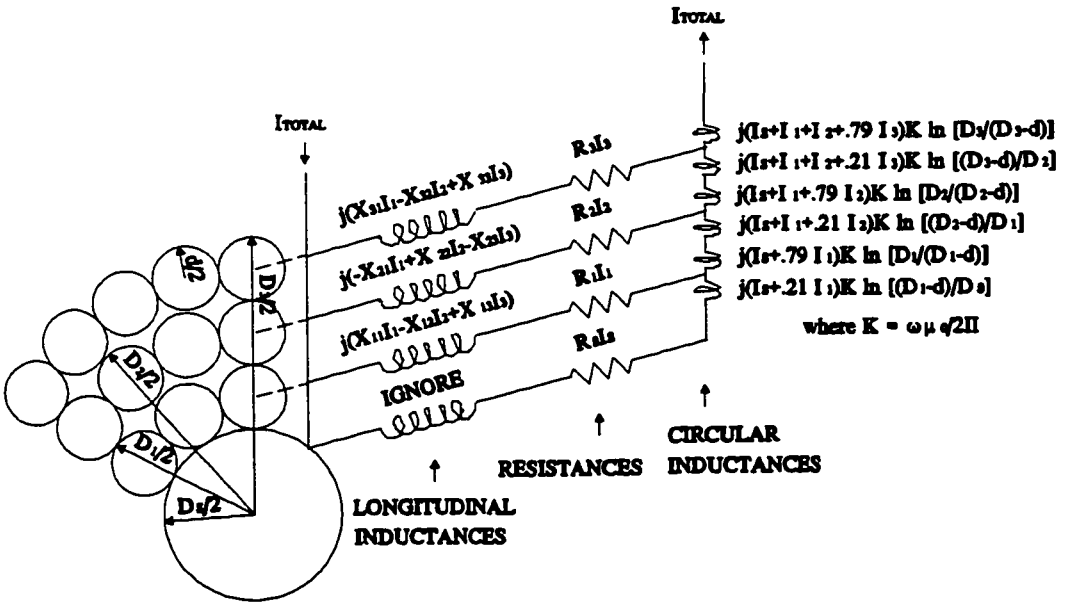

Figure 2 Model of resistances and inductances for a 3-layer ACSR conductor.

The temperature of the layers is assumed to be uniform, and the model is

confirmed by experiment at the temperature 20°C for a three layer "Grackle" conductor, and two layer and single layer conductors obtained by the removal of the successive aluminum layers.

The current in each aluminum layer is calculated from the current density at the centre of the layer. The current in a steel core is calculated assuming uniform distribution, and current density equal to the surface density. The resistance of the steel core is included, but the longitudinal inductance, which does not significantly change current redistribution in aluminum layers, is neglected.

DC resistances of layers are calculated taking into consideration the increase in length of the wires due to stranding. The length factor k_{ln} of the n-th layer is given by

$$k_{ln} = \sqrt{1 + \left[\frac{\pi (D_n - d)}{s_n}\right]^2}$$

where D_n (m) is the outer layer diameter, d (m) is the diameter of the wires in layer n, and s_n (m) is the lay length of the layer. The dc resistance R_n (Ω/m) of the layer n is then

$$R_n = \frac{4\rho}{\pi d^2}\left[\frac{k_{ln}}{m_n}\right] \quad \frac{\Omega}{m}$$

where m_n is the number of the wires per layer, and ρ (Ωm) the resistivity of the material of the layer corrected for the conductor temperature T.

$$\rho = \rho_{20}(1 + \alpha(T-20)) \quad \Omega\ m$$

The longitudinal inductances of the n-th aluminum layer consist of positive self inductance and mutual inductances which have positive signs for the layers spiralling in the same direction, and negative for the layers spiralling in the opposite direction. The current I_n (A) in layer n produces the magnetic field strength

$$H_n = I_n/s_n \quad A/m$$

The resultant longitudinal flux is then given by

$$\Psi_n = \mu_0[\mu_s A_S + ((D_n\text{-}d)^2\pi/4\text{-}A_S)]H_n \quad Wb$$

where μ_s is the relative magnetic permeability of the steel, μ_0 (H/m) the permeability of free space, A_S (m^2) is the steel area, and D_n (m) is the outer diameter of the aluminum layer n. The self inductance L_{nn} is equal to

$$L_{nn} = \Psi_n/I_n s_n = \mu_0[\mu_s A_S + ((D_n\text{-}d)^2\pi/4\text{-}A_S)]/s_n^2 \quad H/m$$

and self reactance X_{nn} is given by

$$X_{nn} = \omega\mu_0[\mu_s A_s + (A_{al}\text{-}A_S)]/s_n^2 \quad \Omega/m$$

or

$$X_{nn} = \omega \mu_0 [\mu_s A_S + (\frac{\pi}{4}(D_n-d)^2-A_S)] / s_n^2 \quad \frac{\Omega}{m}$$

The mutual inductive impedance from layer q to an inner layer p is found from

$$X_{pq} = X_{qp} = \omega \mu_0 [\mu_s A_S + (\frac{\pi}{4}(D_p-d)^2-A_S)] / s_p s_q \quad \frac{\Omega}{m}$$

where D_p (m) is a outer diameter of layer p.

The voltage, layer currents and consequently magnetic field strength, and the relative permeability of the steel core are complex values. In addition, μ_s is a function of the magnitude of the magnetic field. The magnetic field of a conductor with p aluminum layers is given by

$$H = \sum_{n=1}^{p} (-1)^{n+1} I_n / s_n \quad \frac{A}{m}$$

When the circular flux due to the current I_n is calculated assuming that the current is concentrated at the centre of the layer, then the layer produces the flux only outside itself. For a three layer conductor, for example, the outer flux of middle aluminum layer would be

$$\psi_{2,OUTER} = \frac{I_S+I_1+I_2}{2\pi} \mu_0 \ln \frac{D_2}{D_2-d} \quad Wb$$

and the inner flux of the outer aluminum layer would be

$$\psi_{3,INNER} = \frac{I_S + I_1 + I_2}{2\pi} \mu_0 \ln \frac{D_3 - d}{D_2} \quad Wb$$

In this way the contribution of the middle layer current I_2 to the flux $\Psi_{2,OUTER}$ is overestimated, and the contribution of the outer layer current I_3 to the flux $\Psi_{3,INNER}$ is neglected. The model corrected this practice and, assuming uniform current distribution over the layer assumes that 21 % of the layer current contributes to the inner flux of the layer, and 79 % contributes to the outer layer, as shown in Fig. 2.

The model can be used to determine either currents in filaments of the aluminum wires in the layers or the currents in complete layers. The results show that the current is redistributed even within the layer. The circular inductance causes the current density on the outer surface of the layer to be larger than that on the inner surface of the layer. The phase angles of the filament currents increase with distance from the centre of the conductor.

When the model is used to determine the layer currents, it represents a conductor with n aluminum layers through n+2 equations. n+1 equations are obtained from the constraint that the total voltage drop in each layer must be the same. The last equation is obtained from the fact that the sum of the currents in all layers must be equal to the total current. The system of the equations thus has n+2 unknowns, which are complex values: the steel core current, n currents in aluminum layers, and the total voltage drop. The ac resistance of the conductor is calculated when the real part of the total voltage drop is divided by the total current. As the layer currents determine the magnetic field strength H and the complex magnetic permeability is the nonlinear function of its

magnitude, the model equations have to be solved in an iterative way. The model is based upon rms values of current and results in the permeability for an rms value of the magnetic field strength H.

The relationships between the real and imaginary parts of magnetic permeability with magnetic field strength for the particular temperature of the steel core must be known. Furthermore, the complex magnetic permeability depends on tensile stress, diameter and alloy of the steel wires [1]. The lack of data on the permeability of the steel cores is the main reason why this model has not been used more often. In addition, the steel used in ACSR cores is not standardized. The most common type is 0.55 % carbon steel.

The model was verified by experiment on a three layer ACSR "Grackle" conductor for an ambient temperature of 20 °C, and also on two, and single layer conductors obtained by removing successive layers from the "Grackle" conductor. The real and imaginary parts of the permeability of the steel core were measured at this temperature. The measured values are shown in Fig. 3, and can be approximated by the following equations for the magnetic field up to 1000 A/m.

$$\mathrm{Re}(\mu_s) = 40 - 0.0243|H| + 0.000137|H|^2$$

$$\mathrm{Im}(\mu_s) = -(5 + 1.03\times10^{-10}|H|^4)$$

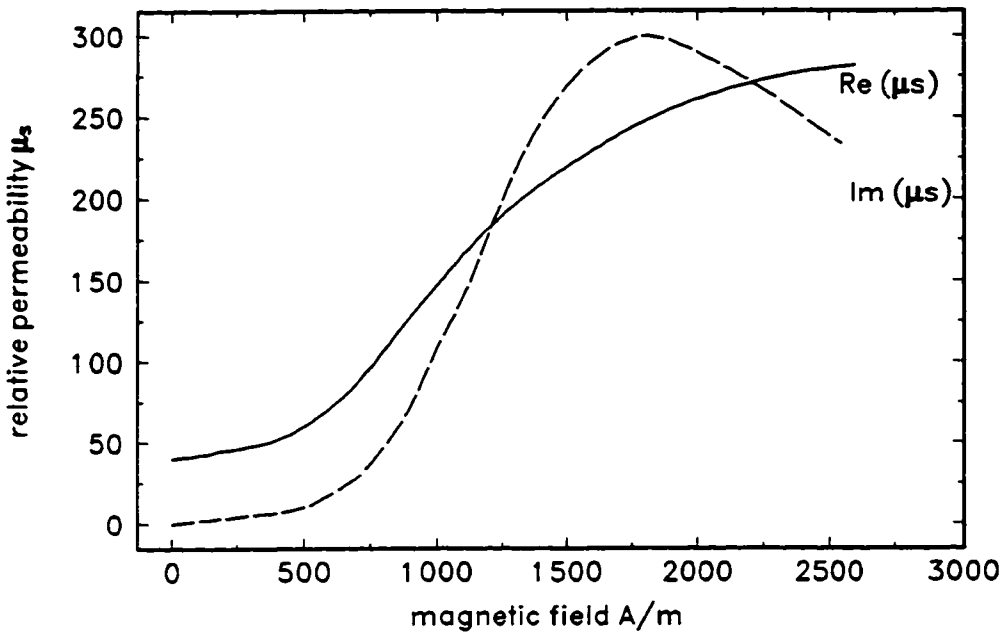

Figure 3 Variation of the real and imaginary parts of the steel core permeability of "Grackle" conductor at the temperature 20 °C, after Barret *et al.*

2.2 MECHANICAL MODEL

For a long period the main method for the calculation of sags and tensions, and the prediction of permanent elongation, was the Graphic Method [3]. The graphic method of sag-tension calculation is based on stress-strain curves and creep data given by manufacturers for the various composition of the conductors. It has the advantage that, though confusing, it can be applied manually. However, it does not account for the cumulative nature of the creep and is not appropriate for new conductors. Hence its use is deprecated.

The flexible conductor with an uniform weight supported at two points has the shape of a catenary. Hence, the calculation of the sag and tension of the conductor is

based on the catenary equation, the parameters for which include the length of catenary which changes with the conductor temperature, elastic elongation, and permanent elongation of the conductor during its lifetime. The biggest uncertainty in predicting the sag and tension of the conductor after some period of exposure is the accurate evaluation of the permanent conductor elongation which occurred till that time.

The conductor deforms permanently when subjected to tension over a period of time. Total permanent deformation consists of two components: metallurgical creep and geometrical settlement. The creep is the consequence of the change of the internal molecular structure of the material when it is exposed to a mechanical tension over time. Metallurgical creep is a function of tension, temperature of the conductor, time of exposure and prior creep. Settlement is caused by a specific composite structure of stranded conductors. During the stranding process the wires are left loose enough so that they tighten together and deform when force is applied. Although geometrical settlement is not completely independent of time, it mainly occurs in a short initial period which can be neglected when compared with the lifetime of the conductor. The settlement of the conductor is a function of the maximum mechanical tension on the conductor.

The CIGRE procedure from Working Group 22.05 for the prediction of permanent elongation of conductors and wires was published in Electra [5]. The elongation of the conductor due to creep and settlement are calculated based on empirical laws given for monometallic and bimetallic conductors. Two sets of predictor equations are given: one for the prediction of total elongation of the conductor, i.e. the sum of the settlement and the creep, and the other based on the elongation of the wires, which makes a distinction between the elongations due to the creep and the settlement. The

latter predictor equations neglect the creep which takes place in the steel core of ACSR conductors. For the assigned conductor history, the permanent elongation of the conductor is calculated in a cumulative way for both sets of predictor equations. The total evaluating time is divided into small intervals for which the stress may be considered constant. The change-of-state equation is used to calculate the stress at the beginning of the next interval from the stress and elongation in the previous one. The stress obtained by any of two sets of predictor equations at the end of the considered period is the average stress of the whole conductor.

The total elongation and the average stress of the complete conductor are sufficient data for most design practice. However, this is not enough for the prediction of the mechanical behaviour of ACSR conductors at high temperatures for which the need is to find the redistribution of the stresses within the conductor.

The Mechanical Model for the sag-tension calculations on ACSR conductors has been developed by a group of authors [6-8]. The separation of the aluminum and steel stresses has enabled an accurate prediction of the permanent elongation and the sag of ACSR conductors even at high conductor temperatures and bigger mechanical loads.

When the conductor operates at higher temperatures, the thermal expansion of aluminum layers is bigger than that of the steel core. As the conductor is clamped at both ends and the axial lengths of both aluminum and steel must be the same, the load in aluminum may change from a tension load to a compression load. Aluminum strands are capable of withstanding a certain compressive load. However, when the compression limit is resolved, birdcaging occurs, a phenomena in which each the aluminum layer is separated from its neighbours of larger diameter. The compressive stress in aluminum

remains constant after birdcaging has occurred. If the temperature is increased after birdcaging has occurred, the thermal expansion of the complete conductor continues at the rate of the steel core. Tests have showed [6] that aluminum strands support the compressive stresses from 6 to 12 MPa, but for sag-tension calculations 10 MPa can be taken.

The model predicts mechanical behaviour of the conductor at higher temperatures. It calculates the actual distribution of the stresses in the aluminum and steel, and enables the prediction of birdcaging and accurate conductor sags at high temperatures. At the same time, the model takes into account the compressive load in the aluminum at high temperatures during the prediction of the permanent elongation of the conductor. While the aforementioned methods assume that at high temperatures the stress-strain curve is the same as the steel curve, the Mechanical Model takes into account the compressive stress in the aluminum and calculates the stress-strain curve of the composite conductor below the steel curve.

Contrary to the assumption used in some other methods that the steel is almost perfectly elastic, the Model accounts for the permanent elongation of the steel core due to the creep which occurs under heavy loading conditions. In this way the calculation of the sag of the conductor under heavy loading conditions and at high temperatures is calculated more accurately.

The strain-summation equation applied separately for steel and aluminum [7] is the logical development of the procedure of CIGRE working group 22.05 [5]. Two coupled equations have to be solved for steel and aluminum stresses, which makes the problem difficult to solve. This problem is solved [7] by relating steel and aluminum

stresses through the equilibrium catenary relationship for the conductor length in the span and by introducing an inverted form of the equilibrium equation.

The total strain of both aluminum and steel is equal to the sum of thermal, elastic, settlement and creep strains of that particular part of ACSR conductor.

$$X_S = DT_S + \frac{\sigma_S}{E_S} + ST_S + CRP_S \quad m/m$$

$$X_A = DT_A + \frac{\sigma_A}{E_A} + ST_A + CRP_A \quad m/m$$

where X_S and X_A are the total strains of the steel and aluminum, DT_S and DT_A (m/m) are the thermal elongation of steel and aluminum, σ_S and σ_A (MPa) are the steel and aluminum axial stresses, E_S and E_A (MPa) are the steel and aluminum moduli of elasticity, ST_S and ST_A (m/m) are settlement strains in steel and aluminum, and CRP_S and CRP_A (m/m) are the steel and aluminum creep strains.

Thermal elongations [7] are given by

$$DT_S = [11.3(T_S-20) + 0.008(T_S^2-400)]\times 10^{-6} \quad m/m$$

$$DT_A = [22.8(T_A-20) + 0.009(T_A^2-400)]\times 10^{-6} \quad m/m$$

where T_S and T_A (°C) are steel and aluminum temperatures, 11.3×10^{-6} and 22.8×10^{-6} ($°C^{-1}$) are the linear terms, and 0.008×10^{-6} and 0.009×10^{-6} ($°C^{-1}$) are the quadratic terms

of the thermal expansion coefficients for steel and aluminum. The quadratic term accounts for the change of the moduli of elasticity with temperature.

The elastic strain is the ratio of the stress and the modulus of elasticity of the material. Moduli of elasticity of the steel and aluminum are obtained from the stress-strain curves for a particular ACSR conductor [7], but in general [8], it can be taken that

$$E_S = 55000 \text{ MPa}$$

$$E_A = 190000 \text{ MPa}$$

The settling strains of steel and aluminum are calculated from the initial 1-hour stress-strain curves. These curves represent the total elongation after one hour at the temperature 20 °C and include the settling strains, the elastic strains, and the one-hour room temperature creep strains. The initial 1-hour stress-strain curves depend on the steel to aluminum ratio of the particular ACSR conductor. However, if the initial curves for conductors with a wide range of steel to aluminum ratio are approximated with single curves for the steel and aluminum, the discrepancies are of the same magnitude as the variation of the results obtained by tests for the specific conductor [8].

The common initial 1-hour stress-strain curves for the steel and aluminum part of the ACSR conductor are given [8] by

$$ST_S = 5.75\text{x}10^{-6}\sigma_S + 9.7\text{x}10^{-22}\sigma_S^6 \quad \text{m/m}$$

$$ST_A = 3.1x10^{-5}\sigma_A + 2.5x10^{-16}\sigma_A^6 \quad m/m$$

The settling strains are the function of the maximum stress which has occured in the steel and aluminum parts until the time of evaluation.

The creep strains for the steel and aluminum components of ACSR conductors can be represented by the following general equations [8]

$$CRP_S = 7\times10^{-18}e^{0.02(T_s-20)}\sigma_S^{4.7}t^{0.13} \quad m/m$$

$$CRP_A = 9\times10^{-6}e^{0.03(T_A-20)}\sigma_A^{1.3}t^{0.2} \quad m/m$$

where t is the time equal to that which the steel or aluminum would spend under the specified stress and temperature till the evaluation moment.

The creep depends on the prior creep strain and is calculated in a cumulative way. The equivalent time t_{eq} necessary to yield the same amount of creep at the stress and temperature from the interval Δt is calculated from the creep strain gained before that interval. The total creep strain at the end of the interval is determined by the creep equation for the time $t = t_{eq} + \Delta t$. The creep during the interval Δt is calculated from the stress at the end of the interval.

The strain summation method is used for the calculation of the sag, stresses, and settling and creep strains. For the time interval Δt, one strain summation equation for the steel and the other for the aluminum component of the ACSR conductor are used. The total strain of the steel X_S is equal to the total strain of the aluminum X_A, as the two components are clamped together.

$$X = X_S = X_A$$

Knowing the temperatures T_S and T_A, an iterative procedure is used to find stresses σ_S and σ_A. As the stresses are assumed to be constant during the interval, Δt has to be small enough to provide the required accuracy. As the lengths of the conductor obtained by the tension and strain equations have to be the same, it is enough to iterate only for the stress σ_S. The following relations among the conductor length L (m), steel and aluminum crossectional areas A_S and A_{al} (mm), the horizontal component of tension H (N), the average conductor tension P (N), and sag D (m) are used in calculations [6]:

$$P = A_S\sigma_S + A_{al}\sigma_A \quad N$$

or

$$P = \frac{H}{2}\left[\cosh\frac{WB}{H} + \frac{\frac{WB}{H}}{\sinh\frac{WB}{H}}\right] \approx \frac{H}{1 - \frac{1}{6}\left[\frac{WB}{H}\right]^2} \quad N$$

where W (N/m) is the conductor weight per unit length and B (m) is half of the span. In order to obtain inverted form of the equilibrium catenary relationship, an approximate equation for P has been developed. The accuracy of this approximation is within 1/360 or 0.3% for $WB/H \leq 1$. This error is acceptable as it corresponds to sag < 1/4 span.

$$L = 2\frac{H}{W}\sinh\left[\frac{BW}{H}\right] \quad m$$

$$L = L_0(1 + X) \quad m$$

where L_0 (m) is unstressed conductor length at room temperature.

$$D = \frac{H}{W}\left[\cosh\left[\frac{BH}{W}\right] - 1\right] \quad m$$

The relation between the conductor length L and horizontal component of tension H is approximated using the equations for the calculation of the actual arc elongation E.

$$E = \frac{L}{2B} - 1$$

$$E = \frac{\sinh\left[\frac{WB}{H}\right]}{\frac{WB}{H}} - 1$$

When expanded, and solved for WB/H, the last equation becomes the inverted equilibrium catenary equation which enables the iteration on the steel stress alone, rather than on both steel and aluminum stresses. The accuracy of H is within 0.06% for WB/H $\leq$ 1.

$$\frac{WB}{H} = \sqrt{\sqrt{100 + 120E} - 10}$$

If birdcaging occurs, the aluminum stress σ_A is taken to be equal to -10 MPa. If the settling strain is less than in the previous interval, the latter is used instead. The unstressed length of the conductor L_0 at room temperature is usually obtained from the calculation in the first interval.

The Mechanical Model predicts the sag, steel and aluminum tensions, and the permanent elongations for the assumed or known chronological loading history. Various loading periods, usually design constraints, characteristic for the line are assumed in a sequence. The more realistic prediction of the loading history of the conductor, the more accurate the results. Each period is divided into intervals Δt for which the strain summation equations are progressively solved.

2.3 STEADY-STATE THERMAL MODEL

Under constant current and weather conditions, the conductor eventually reaches a steady-state temperature. The thermal rating is the current which produces the maximum permissible conductor temperature under specified conditions. The steady-state surface conductor temperature can be determined for the known current from the heat balance equation, by postulating that the total heat gains are identical to the total heat losses when the conductor is in equilibrium. In the same way the current can be determined for a known surface conductor temperature and specified conditions.

Electrical current, the electrical and physical characteristics of the conductor and meteorological parameters determine the surface conductor temperature. Various methods for the calculation of the heat transfer of the conductors differ mainly in the application of atmospheric data, the method of calculation and, to some extent, with the

range of the heat gains and losses.

The Steady-State Heat Model given by Morgan [14-16] provides an accurate method for the assessment of the heat transfer of the conductors. Makhlin [11] introduced Nusselt, Grashof, Prandtl and Reynolds numbers into a calculation of the forced convective heat loss, and noticed the effect of the angle of attack of wind on forced convection. House and Tuttle [12] gave a method for the calculation of the current-carrying capacity of ACSR conductors but without satisfactory wind angle implementation. Webs [13] made some improvements on the model.

Morgan's Model is a detailed method of the calculation which comprises all relevant factors and their relations and a comprehensive study of the factors which affect the heat transfer of overhead conductors. A sensitivity analyses of the steady state [16] shows that some factors have a very small influence on conductor temperature, when compared to other factors, and therefore can be neglected.

The heat balance equation for a unit length of conductor is given by

$$P_J + P_S + (k_{ion}P_{ion}) = P_{con} + P_R + (P_W)$$

where the left side represents the heat gains and the right side the heat losses. P_J (W/m) is Joule or resistive heating, P_S (W/m) is the solar heat gain, P_{ion} (W/m) is the heating due to ionization, and k_{ion} the factor related to thermal diffusion. P_{con}, P_R, and P_W (W/m) are the heat losses due to convection, radiation, and evaporation. If the corona and evaporation which occur randomly are neglected, the heat equation is

$$P_J + P_S = P_{con} + P_R$$

Joule heating is calculated from $P_J = I^2R_{AC}$, where I (A) is the total current and R_{AC} (Ω/m) is ac resistance per unit length corresponding to the actual surface temperature of the conductor and the total current.

2.3.1 SOLAR HEATING

For the conductor with an overall diameter D, inclination to the horizontal ζ, absorptivity of the conductor surface for short-wave radiation α_S, and which is above ground with albedo F, the solar heat gain for isotropic diffuse sky radiation is given by [15]

$$P_S = \alpha_S D \left[I_B \left[\sin\eta + \frac{\pi}{2} F \sin H_S \cos^2 \frac{\zeta}{2} \right] + \frac{\pi}{2} \cos^2 \frac{\zeta}{2} I_d \left(1 + F\right) \right]$$

where I_B (W/m^2) is the intensity of the direct solar beam on a surface normal to the beam, H_S (deg) is the solar altitude, η (deg) is the angle between the solar beam and the axis of the conductor, and I_d (W/m^2) is the intensity of the diffuse sky radiation. The above equation accounts for the beam, diffuse, and reflected radiations, but the long-wave radiation is not included because its contribution to the total solar heating is small. It can be neglected because the incoming long-wave flux is low and the surface absorptivity of the bright conductor for long-wave radiation is ten times less than the absorptivity for short waves. The short-wave absorptivity of the conductor surface depends on the type of the metal and increases with the aging and oxidation. The albedo

of ground differs for various types of soil and vegetation, or other kinds of the covering bellow the transmission line.

The intensity of solar radiation depends on the position of the sun in the sky which changes since the earth revolves around the sun in an ellipse and rotates on its polar axis tilted to the ecliptic axis.

The angle of the solar beam with respect to the conductor axis is calculated by [16]

$$\cos\eta = \cos\zeta \cos H_S \cos(\gamma_S - \gamma_L) + \sin\zeta \sin H_S$$

where γ_S and γ_L (deg) are the azimuths of the sun and conductor axis positive from south through west and γ_S is found from [16]

$$\cos\gamma_S = \frac{\sin\varphi \sin H_S - \sin\delta_S}{\cos\varphi \cos H_S}$$

where φ (deg) is the geographical latitude north positive. The declination of the sun δ_S depends on the day of the year N.

$$\delta_S = 23.45 \sin[360(284+N)/365.24] \quad \text{deg}$$

The solar altitude H_S (deg) is calculated from [15,16]

$$\sin H_S = \sin\delta_S \sin\varphi + \cos\delta_S \cos\varphi \cos\omega_S$$

where ω_S (deg) is the hour angle of the sun which is zero at solar noon and increases by 15 degrees for every hour, being negative after noon. It depends on the geographical latitude and longitude, day of the year, and the clock time.

The intensity of solar radiation normal to the beam I_B, at the height H above sea level, is given by [16]

$$I_B = N_S I_{BO}[1 + 1.4\times10^{-4}H(I_0/I_{BO} - 1)] \quad W/m^2$$

where N_S is the clearness ratio which varies from 1 for the clear sky in nonurban atmosphere to 0 for the sky with thick clouds. The extraterrestrial intensity of solar radiation I_0 is calculated from the solar constant which has a mean value 1353 W/m^2. The earth revolves around the sun in an ellipse and the distance between them varies so that I_0 fluctuates by up to ±3.3 % from its mean value. For N-th day of the year it is [16]

$$I_0 = 1353\ [1 + 0.033\ \cos(2\pi N/365)] \quad W/m^2$$

The intensity of the direct beam at sea level under standard atmospheric conditions is given by [15,16]

$$I_{BO} = 1280\ \sin H_S/(\sin H_S + 0.314)\ W/m^2$$

The diffuse solar radiation occurs due to the complex scattering of the beams by the atmosphere particles and multiple reflections from the ground. When it is assumed

that the diffuse radiation is isotropic, and that the effects of the clear sky can be neglected, I_d is calculated by [16]

$$I_d = (430.5 - 0.3288I_B)\sin H_S \quad W/m^2$$

2.3.2 CONVECTIVE COOLING

The convective cooling occurs when the fluid adjacent to the hot conductor heats and its density decreases causing the fluid flow. If there is no wind the fluid flows upwards and the heat is lost by natural convection. When the wind blows, the fluid is carried away and forced convection takes place. The convective heat loss is given by [15,16]

$$P_{con} = \pi \, Nu \, \lambda_f (T_{sur} - T_{amb}) \quad W/m$$

where Nu is the unitless Nusselt number, T_{sur} and T_{amb} (°C) are the temperatures of the surface of the conductor and the ambient. The temperature of the fluid at the surface of conductor, called film temperature T_f is

$$T_f = 0.5(T_{sur} + T_{amb}) \quad °C$$

and the thermal conductivity of the air at the surface of the conductor, λ_f, is, for temperatures up to 100°C [15,16]

$$\lambda_f = 2.42\times10^{-2} + 7.2\times10^{-4}T_f \quad W/m\,K$$

The calculation of the Nusselt number differs for natural and forced convection. The Nusselt number depends on the kinematic viscosity of the air which changes with the height above sea level. For temperatures up to 100°C, the kinematic viscosity of air at sea level ν_0 is given by

$$\nu_0 = 1.32\times10^{-5} + 9.5\times10^{-8}T_f \quad m^2/s$$

The kinematic viscosity ν_H at the altitude H (m) is

$$\nu_H = \nu_0(1 - 6.5\times10^{-3}H/288.16)^{-5.2561} \quad m^2/s$$

The total or mixed convection, which actually occurs in practice, occurs due to both natural and forced convection. The method for calculation of mixed convection [15,16], used in the Unified Model, combines both natural and forced convection procedures to determine the Nusselt number.

NATURAL CONVECTION

In the case of natural convective cooling, the Grashof number Gr, the Prandtl number Pr, and their product, known as a Rayleigh number Gr.Pr are used to obtain the Nusselt number. All of these numbers are unitless. The Nusselt number for an isothermal horizontal cylinder in the range $10^{-10} \leq Gr.Pr \leq 10^{10}$ may be found from [15,16]

$$Nu = A\,(Gr.Pr)^m$$

where the coefficients A and m from [16] are given in Table 1.

The above formula gives results which are in good agreement with experimental results for stranded conductors in the range $10^2 \leq Gr.Pr \leq 5x10^5$. Therefore, it can also be applied to stranded overhead conductors, despite the increased surface area of the conductor.

Table 1 Coefficients for Nusselt Number for Natural Convection

Range of Gr.Pr From	To	A	m
10^{-10}	10^{-4}	0.675	0.058
10^{-4}	10^{-1}	0.889	0.088
10^{-1}	10^{2}	1.020	0.148
10^{2}	10^{4}	0.850	0.188
10^{4}	10^{7}	0.480	0.250
10^{7}	10^{12}	0.125	0.333

$0.7 \leq Pr \leq 5$

The Grashof number for the conductor with diameter D is calculated from [15]

$$Gr = D^3 g(T_{sur} - T_{amb})/(T_f + 273)\nu_H^2$$

where g (m/s^2) is the acceleration due gravity.

For moderate temperatures up to 100°C, the Prandtl number may be approximated by [15,16]

$$Pr = 0.715 - 2.5x10^{-4}T_f$$

The Nusselt number for a conductor inclined at angle ζ (deg) to the horizontal is obtained by multiplying the Nusselt number by the factor $(\cos\zeta)^{1-3m}$, except for $\zeta \rightarrow 90°$ [15].

FORCED CONVECTION

The Nusselt number for a wind of velocity U, blowing at 90° to the axis of the stranded conductor is given by [16]

$$Nu(90) = 1.1\ C\ Re^n$$

where Re is the Reynolds number [16]

$$Re = UD/\nu_H$$

and C and n are coefficients which depend on Re. The values of C and n from [16] are given in Table 2.

The formula for the Nusselt number for the crossflow wind attack holds for Re less than the critical Reynolds number Re_{cr}. The surface roughness of the conductor due to the helical spiralling of the outer wires channels the fluid flow and affects the forced convective cooling, and thus the Nusselt number. For $100 \leq Re \leq Re_{cr}$, the overall heat transfer from stranded conductors, and consequently the Nusselt number, are 10% higher than that for the smooth conductors. The factor 1.1 in the equation above allows for this. When the Reynolds number exceeds Re_{cr}, the heat transfer from the stranded

conductor increases at a greater rate, and the factor 1.1 is no longer valid. The critical Reynolds number depends on the roughness ratio of the conductor H_r/D = d/2(D-d), where D and d (m) are conductor and wire diameter, [16]

Table 2 Coefficients for Nusselt Number for Forced Convection

Reynolds Number, Re			
From	To	C	n
$1x10^{-4}$	$4x10^{-3}$	0.437	0.0895
$4x10^{-3}$	$9x10^{-2}$	0.565	0.136
$9x10^{-2}$	1	0.800	0.280
1	35	0.795	0.384
35	$5x10^{3}$	0.583	0.471
$5x10^{3}$	$5x10^{4}$	0.148	0.633
$5x10^{4}$	$2x10^{5}$	0.0208	0.814

$$Re_{cr} = 1500\, e^{\frac{0.035}{H_r/D}}$$

The effect of turbulence in the flow is not taken into consideration, as it does not affect the forced convective cooling of outdoor overhead line conductors [32]. The effect of temperature loading which occurs when the high temperature of the surface changes the physical properties of the air can be neglected being less than 3% [16]. When bundle conductors are used, the forced convective heat loss of the leeward conductors increases due to the additional flow caused by the windward conductors. The increase depends on the position of the conductors in a bundle. For horizontally placed conductors it is 10% to 30% for typical spacing distances.

The angle of attack of the wind with respect to the conductor axis is not a

constant value. It fluctuates about a mean value ψ_{mean} (deg) with standard deviation $\sigma\psi$ which depends on the terrain. The fluctuation in the wind results in an effective mean angle of attack ψ^*, higher than ψ_{mean} according to the following [16]:

$$\psi^* = \frac{1}{\sqrt{(2\pi)}} \left[2(\sigma\psi) e^{-\frac{\psi_{mean}^2}{2(\sigma\psi)^2}} + \sqrt{2\pi}\ |\psi_{mean}|\, \mathrm{erf}\left[\frac{|\psi_{mean}|}{\sqrt{2}(\sigma\psi)} \right] \right] \quad \text{deg}$$

When the wind blows at some effective mean angle of attack ψ^* to the conductor axis less than 90°, the ratio of the Nusselt number for that angle Nu(ψ^*) and the Nusselt number for the crossflow Nu(90) may be approximated from [16]:

$$Nu(\psi^*)/Nu(90) = A_1 + B_1(\sin\psi^*)^p$$

where $A_1 = 0.42$, $B_1 = 0.68$ and $p = 1.08$ for $0° \le \psi^* < 24°$, and $A_1 = 0.42$, $B_1 = 0.58$ and $p = 0.90$ for $24° \le \psi^* < 90°$. Even though the crossflow component of the vector of the wind velocity $U\sin\psi^*$ is equal to zero when $\psi^* = 0°$, the heat convective loss does not fall bellow 42 % [14,16].

MIXED CONVECTION

When the wind velocity is very low, neither the natural convection nor the forced convection are negligible compared to one another. They are combined in a mixed convection. The Nusselt number for mixed convection is obtained from the effective Reynolds number Re_{eff}, the vectorial sum of Reynolds numbers for the forced and natural

flows. The equivalent Reynolds number Re_{eq} for the natural convection is the one which would result in the same amount of heat transferred by forced convection. Consequently, Re_{eq} is given by [16]

$$Re_{eq} = \left[\frac{A}{C}(GrPr)^m\right]^{\frac{1}{n}}$$

where A and m are defined in Table 1 and C and n are defined in Table 2.

The natural convective flow is vertical. For the angle ϕ (deg) between the natural and forced flows, the effective Reynolds number, Re_{eff} for a mixed flow is given by [15,16]

$$Re_{eff} = [(Re_{eq} + Re\cos\phi)^2 + (Re\sin\phi)^2]^{1/2}$$

The wind usually fluctuates close to the horizontal. When $\phi = 90°$, the effective Reynolds number is [15,16]

$$Re_{eff} = (Re_{eq}^2 + Re^2)^{1/2}$$

The Nusselt number with mixed flow is found from the effective Reynolds number.

The boundary between natural convection and mixed convection is determined by the limiting Grashof number Gr_{lim} [16].

$$Gr_{lim} = C_1 Re^{n/m}$$

Table 3 Constants for the Limiting Grashof and Reynolds Numbers for Mixed Convection (ϕ = 90°)

Gr.Pr		Re			
From	To	From	To	C_1	C_2
10^{-10}	10^{-2}	$1x10^{-4}$	$4x10^{-3}$	$4.68x10^{-4}$	72.7
		$4x10^{-3}$	$9x10^{-2}$	0.0629	3.1
		$9x10^{-2}$	1	221	0.784
10^{-2}	10^{2}	$4x10^{-3}$	$9x10^{-2}$	0.0258	51.0
		$9x10^{-2}$	1	0.633	3.05
		1	35	1.33	3.1
10^{2}	10^{4}	$9x10^{-2}$	1	1.99	1.51
		1	35	3.55	1.86
		35	$5x10^{3}$	1.21	4.03
10^{4}	10^{7}	1	35	27.9	0.396
		35	$5x10^{3}$	12.4	1.14
		$5x10^{3}$	$5x10^{4}$	0.125	13.6
10^{7}	10^{12}	35	$5x10^{3}$	411	0.0616
		$5x10^{3}$	$5x10^{4}$	13	1.55
		$5x10^{4}$	$2x10^{5}$	0.0813	21.9

The limiting Reynolds number Re_{lim} is the boundary between pure forced convection and mixed convection [16].

$$Re_{lim} = C_2 \, Gr^{m/n}$$

The values of the coefficients C_1 and C_2 from [16], for ϕ = 90°, are given in Table 3.

2.3.3 RADIATIVE COOLING

Radiative cooling is calculated from [15,16]

$$P_R = \pi D\sigma_B\epsilon_S[(T_{sur} + 273)^4 - 0.5(T_{gr} + 273)^4 - 0.5(T_{sky} + 273)^4] \quad W/m$$

where T_{gr} and T_{sky} (°C) are ground and sky temperatures, σ_B is the Stefan-Boltzman constant equal to 5.66997×10^{-8} $Wm^{-2}K^{-4}$, and ϵ_S is the emissivity of the conductor, which depends on the type of metal and increases with aging and oxidation. For the aluminum surface of stranded conductor the emission may increase up to 0.95 for the weathered conductor in an industrial environment. However, since the radiative heat loss for a typical conductor does not exceed 30% of the total heat loss, as an approximation, the ground and sky temperatures may be equated to the ambient air temperature T_{amb} (°C), and the radiative heat loss is then

$$P_R = \pi D\sigma_B\epsilon_S[(T_{sur} + 273)^4 - (T_{amb} + 273)^4] \quad W/m$$

The effect of the bundle conductors on radiative cooling can be neglected for the same reason.

2.4 RADIAL CONDUCTION MODEL

Although the metals comprising overhead line conductors have high thermal conductivities, the radial thermal conductivity of stranded conductors is significantly less than that of solid metal, about one hundredth of the value for a solid metal. As the heat generated due to the Joule heating within the conductor is conducted radially to the conductor surface where it is dissipated to the air, the temperature within the conductor drops from the centreline to the surface of the conductor. The temperature falls radially

in the steps across the conductor as the heat flows through the strands with low thermal resistances and the contacts between strands with high temperature resistances. The radial temperature difference depends on the current, the resistance, the construction of the conductor, and the effective radial thermal conductivity and is independent of the thermal power loss.

Morgan pointed out the significance of the radial temperature gradients [14] and related the increase of radial thermal conductivity to the increase of conductor tension and hence to the rise of contact pressure and resultant increase in contact areas between the wires. Morgan first formulated an analytical model for radial temperature difference in stranded conductors [33]. Foss *et al.* [34] also noticed the effect of conductor tension on the radial thermal conductivity. However, Foss also stated that the wind speed affects the thermal conductivity, and that the radial thermal conductivity does not depend on the material of the conductor, which has since been proven wrong by Morgan, discussion to [35] and [9].

Black *et al.* [35] developed a mathematical model, solved by a numerical technique, for temperature gradients within overhead conductor and showed that the vast majority of the temperature drop in an ACSR occurs in the conducting strands, while the steel core layers are practically isothermal. He pointed out that the effective thermal conductivity of ACSR conductors can be a function of the conductor temperature when the high temperature causes birdcaging of the conductor.

The Radial Conduction Model developed by Morgan and Findlay [9,10] determines the temperature differences between the layers assuming that the heat flows radially towards the surface of the conductor through a number of parallel paths formed

by the micro-contacts between strands and the air voids between strands in adjacent layers. The micro-contacts between the strands consist of numerous direct metal to metal contacts at the crests of the asperities and the air gaps in between. Due to the low thermal resistance of the metal, the temperature differences within the strands are very small comparing to the differences between the layers, and thus it can be assumed that each strand is isothermal.

The heat is transferred by conduction at the metal to metal contacts and by conduction, convection and radiation in air gaps and air voids. However, the heat transfer by radiation up to 200 °C and by convection is negligible so that the heat flows radially by conduction through the metal to metal contacts, air gaps, and air voids in parallel.

The total contact area between two layers depends on the number of contacts per unit length and the area of each contact. The number of contacts depends on the construction of the conductor and the area of contact depends on the radial force and the type of the wire material. The total contact area between two layers then in fact depends on the total radial force on the wires of the inner layer and the value of the compressive yield stress for the material of the wires.

If the king wire of a monometallic conductor is denoted with 0, succeeding layers with numbers growing from 1, and all the values are calculated per unit length of the conductor, then the difference between temperatures of layers n and n+1 denoted by subscript n(n+1) is given by

$$T_n - T_{n+1} = \sum_{i=o}^{n} P_i / \Sigma (hA)_{n(n+1)} \quad °C$$

where $\sum_{i=o}^{n} P_i$(W/m) is the total power gain up to the layer and including layer n, and

$\Sigma(hA)_{n(n+1)}$ (W/°C) is the sum of the products of the heat transfer coefficients due to the conduction h ($Wm^{-2}K^{-1}$) and contact area A (m^2) between layers n and n+1 per unit length. For the subscripts m, g, and v which denote the metal to metal contacts, air gaps, and air voids respectively

$$\Sigma(hA)_{n(n+1)} = \Sigma(h_m A_m)_{n(n+1)} + \Sigma(h_g A_g)_{n(n+1)} + \Sigma(h_v A_v)_{n(n+1)} \quad W/°C$$

The sum of the area of true metallic contacts A_m and the area of the air gaps between them A_g is equal to the product of the number of contacts q between wires in layers n and n+1 and apparent total area of each contact A_q.

$$A_{mn(n+1)} + A_{gn(n+1)} = q_{n(n+1)} A_{qn(n+1)} \quad m^2$$

The ratio

$$A_{mn(n+1)}/A_{gn(n+1)} = A_{tn(n+1)}/(A_{qn(n+1)} - A_{tn(n+1)})$$

shows that A_m is proportional to the actual total area of the of each contact A_t and A_g is proportional to the rest of the apparent area of the contact. The actual area of the metal-metal contact is that area which is sufficient to withstand the pressure without exceeding the yield stress of the metal.

The area of voids A_v between layers n and n+1 is given by

$$A_{vn(n+1)} = \pi d(2n+1) - q_{n(n+1)}A_{qn(n+1)} \quad m^2$$

The total radial temperature difference for a conductor with N layers is given by

$$T_0 - T_N = \sum_{n=0}^{N-1} (T_n - T_{n+1}) \quad °C$$

NUMBER OF CONTACTS BETWEEN TWO LAYERS AND AREA OF EACH CONTACT

The number of contacts between wires with diameter d in the layers n and n+1 with lay lengths s_n and s_{n+1} is obtained from

$$q_{n(n+1)} = m_n^2 \left[\frac{1}{s_n} + \frac{1}{s_{n+1}} \right]$$

where m_n is the number of the wires in layer n, and $1/s_0 = 0$ for the king wire.

For the total axial tension T′ in a conductor with N layers, the tension in layer

n is given by

$$T_n' = 6nT' \cos^2\beta_n \left[1 + \sum_{n=1}^{N} 6n\cos^3\beta_n\right]^{-1} \quad N$$

where β_n (deg) is the angle of lay of wires in layer n , and

$$\cos\beta_n = s_n[s_n^2 + (\pi nd)^2]^{-1/2}$$

The total radial force F_m in layer n is calculated by

$$F_m = T_n' \sin^2\beta_n/nd \quad N$$

The total radial force on the wires in layer n F_m' is obtained as the sum of the radial forces of all layers above the layer n

$$F_m' = \sum_{i=n+1}^{N} F_m \quad N$$

The radial force per contact F_{rqn} is then

$$F_{rqn} = F_m'/q_{n(n+1)} \quad N$$

and the apparent area of each contact

$$A_{qn(n+1)} = F_{rqn}/f_y \quad m^2$$

where f_y (Pa) is the compressive yield stress which depends on a type of wire material.

As the metal-metal contacts are estimated to be a very small portion of the contact area, the main heat transfer occurs through the air gaps between asperities. The very small air gap thickness contributes to the significance of the heat transfer via air gaps. The portion of the heat transfer through the air voids increases towards the surface of the conductor, as the number of the voids increases with the number of strands per layer.

The area of contacts, and hence the effective radial thermal conductivity of the conductor increases with increasing tension. The area of contacts increases and the air gap thickness decreases with time due to the creep of the metal, and hence the radial thermal conductivity of the conductor increases with time, but only if the radial force is maintained constant.

CONDUCTIVE HEAT TRANSFER ACROSS METAL-METAL CONTACTS

The conductive heat transfer coefficient for metal-metal contacts is decreased by the constrictions in the heat path. It may be approximated as:

$$h_m = \frac{1.13 k_{hm} \tan\theta}{\sigma} \left[\frac{p_q}{H}\right]^{0.94} \quad \frac{W}{m^2K}$$

where σ (m) is the r.m.s. height of the asperities, tan θ is their mean slope, and H (Pa) is the microhardness of the softer material. The harmonic mean of the bulk thermal

conductivities k_1 and k_2 of two metals in contact is given by

$$k_{tm} = 2k_1k_2/(k_1+k_2) \quad Wm^{-1}K^{-1}$$

and the mean pressure over apparent area p_q is found from

$$p_q = F_{rqn}/A_{qn(n+1)} \quad Pa$$

If the mean pressure over the actual total contact area $A_{tn(n+1)}$ during plastic deformation is assumed to be equal to H, then

$$\frac{p_q}{H} = \frac{A_{tn(n+1)}}{A_{qn(n+1)}}$$

The ratio of the actual to the apparent total contact area is found from

$$A_{tn(n+1)}/A_{qn(n+1)} = (1/2)\ \mathrm{erf}[Y/(\sqrt{2})\sigma]$$

where Y (m) is the separation distance between the mean lines of the two surfaces in contact.

CONDUCTIVE HEAT TRANSFER ACROSS AIR GAPS AT CONTACTS

The conductive heat transfer coefficient for the air gaps between asperities is found from

$$h_g = k_g/\delta_g \quad Wm^{-2}K^{-1}$$

where k_g ($Wm^{-1}K^{-1}$) is the air thermal conductivity and δ_g (m)is the effective length of the gap. The thermal conductivities of the metals and air depend on the temperature. The effective radial thermal conductivity of the conductor increases with increasing air pressure [10]. The effective thickness of the air gap is approximately 1 μm, and is calculated to be 0.6 μm at the contacts between inner and middle layer, and 0.15 μm between middle and outer layer [18], and is estimated to be between 0.75 μm and 0.9 μm [10].

CONDUCTIVE HEAT TRANSFER ACROSS VOIDS BETWEEN STRANDS

The conductive heat transfer coefficient for the air voids is found from

$$h_v = k_g/\delta_v \quad Wm^{-2}K^{-1}$$

The voids between the strands in adjacent layers are triangular between the king wire and first layer, and may be mainly triangular or mainly rectangular between other layers. The complex conductor geometry makes it difficult to estimate the conductive heat transfer via the voids. The effective length of the void δ_v can be determined as a mean spacing, the ratio of the area of the void and its maximum width. For triangular voids it is given by

$$\delta_v = \left[\frac{\sqrt{3}}{2} - \frac{\pi}{4}\right] d = 0.0806d \quad m$$

and for rectangular voids

$$\delta_v = (1 - \frac{\pi}{4})d = 0.2146d \quad m$$

Another way to determine the effective length of the void is to use the hydraulic diameter, i.e. 4(area/perimeter). For the triangular void the hydraulic diameter is found from

$$\delta_v = \left[\frac{2\sqrt{3}}{\pi} - 1\right] d = 0.1027d \quad m$$

and for the rectangular void it is found from

$$\delta_v = (\frac{4}{\pi} - 1)d = 0.2732d \quad m$$

The effective radial thermal conductivity for the conductor with the rectangular voids is smaller than that for the same conductor with triangular voids. The calculated effective thermal conductivity is less when the effective length of void is found as the hydraulic diameter than when it is found as the mean spacing.

The model evaluates the radial temperature differences between the layers for the axial tensile forces which result in compressive radial forces in each layer. The area of

contact can be calculated only for the compressive radial force. The effective lengths for the air gaps and air voids is estimated and verified by tests only for the compressive radial force. In the case of ACSR conductors, the aluminum layers may come under compression. The aluminum withstands the axial compressive pressure up to approximately 10 MPa, meaning that the aluminum layers will not separate. However, the radial forces in aluminum layers change direction, crossing zero for zero axial load. It is unknown precisely what happens with the contact areas, and how much the effective lengths of air gaps and air voids increase when the aluminum comes under compression at high temperatures. When the compressive axial pressure exceeds 10 MPa, and birdcaging occurs, the separation of the layers may result in the total loss of contact areas and deformation of air voids at some instances of conductor length. The compressive aluminum stress and birdcaging decrease the effective radial thermal conductivity of ACSR conductors [9]. More research is necessary to evaluate both stages of this phenomena, and to give an analytical method for its evaluation. However, under birdcaging conditions only small portion of the conductor is usually affected.

2.5 METHOD FOR CALCULATING THE LOSS OF TENSILE STRENGTH

During the service life, the nonferrous wires of the conductor exposed to elevated temperatures lose tensile strength due to annealing. The steel wires do not lose strength by annealing at temperatures up to 250 °C [17]. During drawing the material of the wires is severely cold worked and a considerable amount of energy is stored in the form of defects. This stored energy causes plastic deformation through the recovery and subsequent recrystallization. When the material is subjected to stress during annealing,

conditions are favourable for the occurrence of creep and recovery proceeding subsequently to recrystallization. During recrystallization the material is significantly softened, the strain-free grains form and grow, decreasing the hardness and tensile strength. Recovery and recrystallization can overlap. The hardness and tensile strength decrease slightly during recovery, but decrease significantly during recrystallization with increasing temperatures and time of duration.

Morgan [17,19] developed a method for the evaluation of the loss of tensile strength of the conductor due to annealing. The loss of tensile strength of wires and stranded conductors operating at high temperatures depends on the temperature, time duration of that temperature, initial chemical composition, and the amount of the cold work during the process of drawing. Usually the conductor wire is drawn from the draw rod of standard diameter so that the smaller the wire diameter, the bigger the degree of cold working.

The loss of tensile strength W (%) of the conductor for the given absolute temperature T^* (K) and time duration t (hours) is given by [17]:

$$W = W_a\{1 - \exp[-\exp(A' + (B'/T^*)\ln t + C'/T^* + D'\ln(R/80))]\}$$

where W_a is the percentage loss of the strength in the fully-annealed state, A′, B′, C′, and D′ are constants which depend on the conductor material, and R is the percentage reduction in cross-sectional area during wire drawing. Some evidence shows that D′ may depend on the time duration at constant temperature. The value of W_a depends on the material, for example, for aluminum, $W_a = 56$ %.

For the evaluation of the loss of tensile strength due to annealing, the thermal history of the conductor has to be known or assumed. As the annealing is cumulative process, the temperatures T_1, T_2, $T_3..T_n$ of the conductor and their time durations t_1, t_2, $t_3..t_n$ will result in a total loss of tensile strength W_n' over the total period of exposure. The total cumulative loss is found by the following steps:

$$W_1 = f(T_1^*, t_1) = f(T_2^*, t_{2eq})$$

$$W_2' = f(T_2^*, t_2 + t_{2eq}) = f(T_3^*, t_{3eq})$$

.....

$$W_{n-1}' = f(T_{n-1}^*, t_{n-1} + t_{(n-1)eq}) = f(T_n^*, t_{neq})$$

$$W_n' = f(T_n^*, t_n + t_{neq})$$

where t_{eq} is the equivalent time which the conductor should have spent at the succeeding temperature to result in the same loss of strength as produced by the preceding temperature and its corresponding time duration.

CHAPTER 3

UNIFIED MODEL

3.1 OVERVIEW

This work links electromagnetic, mechanical, steady-state thermal, and radial conduction models for the first time in the Unified Model. These models were used separately in the past. Each of the models has been experimentally verified. The Unified Model takes into consideration their mutual influences and dependencies. Interrelations among the variables of the models are identified and ties between the models are explained in 3.2. Input to the Unified Model consists of the same variables that are used as input to the individual models, except for the variables that are produced as the output of one of the models and are used as the input to any other model. These variables, shown in Fig. 4, are called the coupling variables and are carried from the model that outputs them to the next model that uses them as the input. Contrary to the assumption used by an individual model that the coupling variables are fixed inputs, the Unified Model calculates values of coupling variables that satisfy both the mutual dependencies between models and the individual models. This process is called equilibration of variables. In order to connect the four existing models, each of them has been developed further. Implementation of the models and premises that are introduced are discussed in 3.3.

Connection of all four models and coupling of all aspects of the behaviour of the conductor enabled implementation of the probabilistic approach for the evaluation of the conductor history, as described in 3.4. Furthermore, the coupling of the models and the introduction of a probabilistic approach made an assessment of the loss of tensile strength of aluminum layer due to annealing possible. All this improved the accuracy of the prediction of the conductor characteristics beyond the sole combination of the four existing models, and removed some of the constraints of the individual models.

The constraints of individual models corresponding to the mutual influence of the models as well as to the accurate evaluation of the conductor history are thus removed now in the Unified Model. However, other inherent limitations of the individual models remain. For example, neither corrosion, nor the effects of corona have been considered in the Unified Model.

The method developed for the coupling of existing models using the probabilistic approach is a general procedure that is particularly applicable to ACSR conductors. Flowcharts given in 3.5 explain the procedure for the coupling of four models into the Unified Model and the implementation of the probabilistic approach and the method for the assessment of annealing of aluminum wires.

For the time interval with the probabilistic ambient temperature and current selected from the probability density function, coupling of the four models starts with the initial assumption that the conductor is isothermal and is at the surface conductor temperature. The Steady-State Heat Transfer Model and Electromagnetic Model are combined together to calculate the total power losses (E) and the surface temperature (C) that satisfy both models. It also outputs layer power losses (D). The surface

temperature (C) is passed then to the Mechanical Model that calculates stresses in steel and aluminum (A). Steel and aluminum stresses (A) from the Mechanical Model and layer power losses (D) are then carried to the Radial Conduction Model which calculates radial temperature differences (B). These are looped back to the Electromagnetic Model to obtain more accurate layer power losses (D) still using the same surface conductor temperature (C) calculated at the beginning, but with layers at different temperatures. New layer power losses (D) are used again in the Radial Conduction Model to calculate more accurate radial temperature differences (B). These more accurate temperature differences (B) are then looped back to the Steady-State Heat Transfer Model in combination with the Electromagnetic Model to obtain a more accurate surface conductor temperature (C). The same procedure is repeated again to obtain more accurate layer power losses (D) and radial temperature differences (B). At the end of this procedure (step), radial temperature differences (B) and surface temperature (C) are carried into the Mechanical Model for more accurate calculation of the stresses in steel and aluminum (A). These are again, together with more accurate layer power losses (D) from the Electromagnetic Model, used for calculation of more accurate radial temperature differences (B) in the Radial Conduction Model. The procedure called the step is repeated again until the successive iterations indicate negligible further change in coupling variables. Then, the next time interval is started. The whole process is repeated until the required total exposure time has been obtained.

The flowcharts from 3.5 are the basis for the software that is created as a result of this work. This complete computer program runs smoothly and is used for the calculation of all results presented in this thesis. The software is of modular type that

will easily allow for future changes and improvements of individual models and input data. The purpose of this Model is to integrate the current state of knowledge and to enable the inclusion of factors that may be addressed by industry in the future. Input data that are used in the Model to produce the results are given in 3.6.

3.2 VARIABLES

The Unified Model takes into account all the interrelations among the variables in separate models. Each of the four models includes a set of variables. The list of input and output variables for the four separate models are given in Tables 4 and 5. Variables related to the calculation of the loss of tensile strength of the nonferrous wires due to annealing are included in the Mechanical Model. Since the Electromagnetic Model and the Mechanical Model are particularly applicable for ACSR conductors, the listed variables are given for the steel-cored conductor.

Some of the input variables are common for two or more models. Others, like complex relative permeability, depend on the variables from an individual model or on the variables from one or more of the other models. Some outputs from one model are used as inputs to another model.

Some variables from Tables 4 and 5 denote a group of characteristics. The construction includes the details related to the conductor data, such as overall diameter, diameters of wires, lay lengths, number of layers, number of wires per layer, bare conductor weight, and cross-sectional areas of the conductor, aluminum and steel.

For the Unified Model the set of output variables is uniform. All variables from Tables 4 and 5 except these which are output variables are input variables. The output

variables from any of the four models which are input variables for any other model represent the couplings between the models in the Unified Model. These are the stresses in aluminum and steel, the radial temperature differences between layers, the surface conductor temperature, electrical currents in the steel core and the aluminum layers, the voltage, and ac resistance of the conductor. The aluminum and steel stresses are the outputs from the Mechanical Model and the inputs for the Radial Conduction Model. The radial temperature differences between layers are the outputs from the Radial Conduction Model and the inputs for both the Mechanical Model and the Electromagnetic Model. For the known current, the surface temperature of the conductor is the output from the Steady-State Heat Transfer Model, and the input for both the Mechanical Model and the Electromagnetic Model. The outputs of the Electromagnetic Model are used as inputs for the Steady-State Heat Transfer and the Radial Conduction Models. The complex currents in a steel core and aluminum layers and complex voltage are used as input for calculation of the power losses per layers in the Radial Conduction Model. The ac resistance of the conductor is used for the calculation of power loss per unit length of the complete conductor, i.e. the Joule heating in the Steady-State Heat transfer Model. The direct coupling among the four models in the Unified Model is shown on Fig. 4. The coupling among the Mechanical Model and the Electromagnetic Model through the dependence of magnetic permeability of steel core on the steel stress is not considered. Information about the variation of the magnetic permeability with both temperature and stress are still unknown.

Table 4 Input and output variables in mechanical (M), electromagnetic (EM), radial conduction (C), and steady-state heat transfer (H) models

Variable	M	EM	C	H
Ac resistance of the conductor		★		*
Air gap at contacts			*	
Air pressure			*	*
Albedo				*
Altitude				*
Ambient temperature				*
Annealing coefficients	*			
Axial current		*		*
Azimuth				*
Clearness ratio				*
Complex magnetic field		★		
Complex relative magnetic permeability		★		
Complex currents in steel and aluminum layers		★	*	*
Complex voltage		★	*	*
Creep strains in aluminum and steel	★			
Electrical frequency			*	
Inclination	*			*
Latitude				*
Loading history	*			
Loss of tensile strength in aluminum layers	★			
Number of day in year				*
Power loss		★	*	*
Radial temperature differences	*	*	★	
Reduct. in crossect. area due to wire drawing	*			
Sag	★			
Settling strains in aluminum and steel	★			
Span length	*			
Standard deviation of wind angle				*
Stress in aluminum	★		*	
Stress in steel	★	*	*	
Surface temperature	*	*		★
Tension	★	*		
Time duration	*			
Total length of the conductor	★			
Total strain	★			
Wind angle to axis				*
Wind speed				*

* = input variables, ★ = output variables

Table 5 Input and output variables - construction of the conductor and characteristics of materials in mechanical (M), electromagnetic (EM), radial conduction (C), and steady-state heat transfer (H) models

Variable	M	EM	C	H
Absorptivity				*
Coeff. of linear expansion of alum. and steel	*			
Construction	*	*	*	*
Dc resistances of aluminum and steel at 20°C		*		
Elasticity moduli of aluminum and steel	*			
Emissivity				*
Loss of strength of alum., fully annealed	*			
Permeability data for different temperatures		*		
Temp. coeff. of resist. of alumin. and steel		*		
Thermal conductivity of aluminum, steel, air	*			
Yield stress of aluminum and steel	*			

* = input variables, ★ = output variables

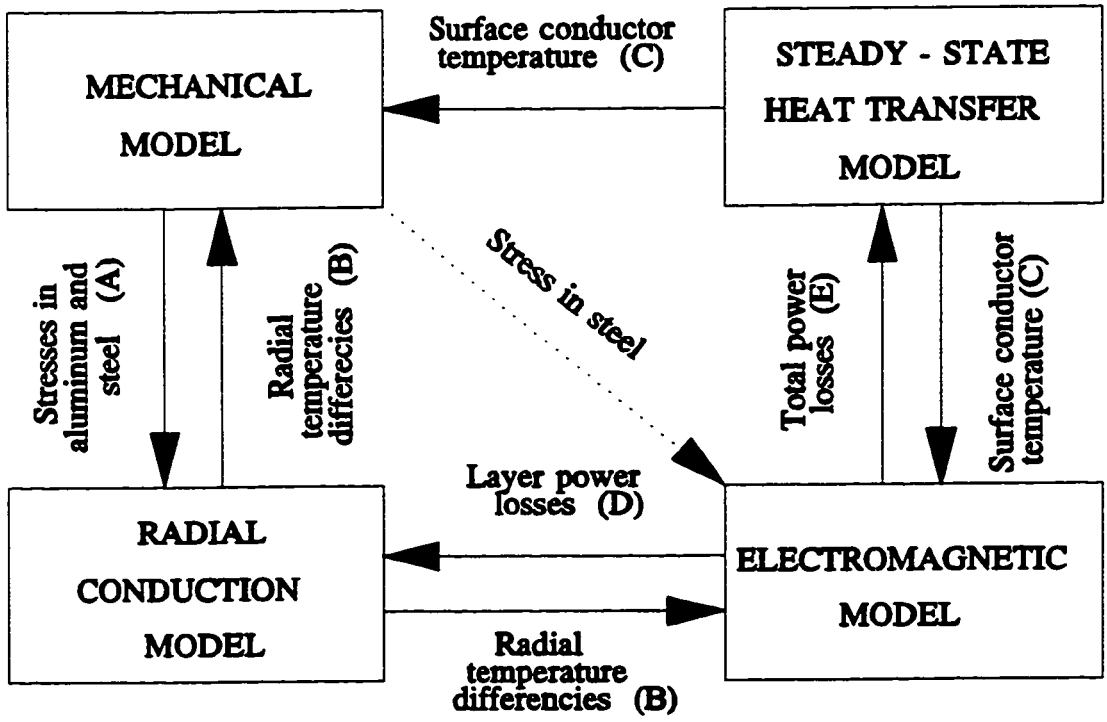

Figure 4 Direct coupling among the four models in the Unified Model

3.3 IMPLEMENTATION OF THE MODELS

The Mechanical Model distinguishes the stresses in aluminum and steel, but not the stresses in each layer. That would enable the exact prediction of the mechanical, electrical and thermal characteristics of the stranded conductors by the Unified Model. This drawback of the Mechanical Model introduces a certain amount of uncertainty in the results of the Unified Model. The mean temperatures of the aluminum and steel components of the conductor, T_A and T_S, are calculated from the radial temperature differences between layers and the surface temperature of the conductor. The temperature of the layer i of the conductor with N layers is given by

$$T_i = \sum_{n=i}^{N-1} (T_n - T_{n+1}) + T_{sur} \quad °C$$

The temperature of the outer layer of the conductor is equal to the surface temperature $T_N = T_{sur}$. If the conductor has N_S steel layers, the steel and aluminum temperatures are given by

$$T_S = \sum_{i=0}^{N_S} T_i \, (nw)_i \; / \sum_{i=0}^{N_S} (nw)_i$$

$$T_A = \sum_{i=N_S+1}^{N} T_i \, (nw)_i \; / \sum_{i=N_S+1}^{N} (nw)_i$$

where $(nw)_i$ is the number of the wires in the layer number i.

The calculation of the loss of tensile strength of aluminum layers due to annealing

is included in the Mechanical Model, as for both the Mechanical Model and the annealing calculation the history of the conductor has to be known. However, to obtain accurate values for the loss of tensile strength of the aluminum layers, the temperatures of the layers are used.

The temperatures of the layers are used for the calculation of dc resistances of the layers in the Electromagnetic Model. The relative magnetic permeability of the steel core depends on the temperature, wire diameter, and stress. The modulus of the complex relative magnetic permeability increases with increasing temperature, decreases with increasing wire diameter, and decreases with increasing stress [1]. There is little data on the variation of the complex magnetic permeability of the steel core for these conductors pertaining as functions of temperature and stress. Moreover, the effect of the frequency on the complex permeability has not been investigated in the literature, although it has been found that a ac to dc resistance ratio increases nonlinearly with increasing frequency. The complex permeability of the steel core is a function of the magnetic field strength, which depends on a current redistribution within the conductor. The current redistribution depends on the temperature in the layers. For a given current, layer temperatures, and data on the relative permeability for the whole range of magnetic field strength, the equilibrium between the complex permeability and the magnetic field strength is found by an iterative procedure.

The Unified Model uses the published data for the relative permeability of the galvanized steel wires [1,2,16]. Variation of the modulus of the relative permeability of steel wires with magnetic field strength for various tensile stresses at temperature 20 °C and for various temperatures at tensile stress 0 MPa are given in References [1] and [16].

There are no published data on the variation of the relative magnetic permeability of steel wires with magnetic field strength for both tensile stress and temperature simultaneously. As there is no way to relate existing permeability data for various tensile stresses and various temperatures in some reliable way, only one of these variations can be considered. One of the main purposes of Unified Model is the prediction of the behaviour of the conductor at high temperatures. For that reason only the variation of relative permeability of steel wires with magnetic field strength for various temperatures is considered. However, the modulus of relative permeability does not change significantly with tensile stresses up to 320 MPa for the magnetic field strength up to 1000 A/m [1,16] and the final results are not affected significantly. Should the variation of the permeability for the steel cores be available for both stresses and temperatures, these data can be readily implemented in the Unified Model.

In that case, there would be direct coupling between the Mechanical Model and the Electromagnetic Model. The steel stress from the Mechanical Model would be used as only one additional criterion in the iterative procedure for the balancing of the complex permeability and magnetic field strength. The steel stress increases with the time of exposure, as the aluminum transfers the load to the steel, and this effect would be interesting to explore.

The permeability curves for 20, 80, and 130 °C are used for the temperatures of the steel core up to 60 °C, between 60 °C and 100 °C, and above 100 °C, respectively. Only the data for these temperatures were available [1,2,16]. The mean temperature of the steel core is calculated from the temperatures of the steel layers in the same way as for the Mechanical Model.

The Thermal Conduction Model assumes a uniform distribution of the steel and aluminum stresses. Triangular voids are assumed and the effective spacing of the voids is calculated using the hydraulic diameter. If the effective spacing of the voids had been calculated using the mean spacing, the effective spacing of the voids between the outer steel layer and next aluminum layer would have been smaller than those between steel-steel layers. As the area of the voids between steel wires of smaller diameter and aluminum wires of bigger diameter should be bigger than the area of the voids between steel wires only, the method that uses the mean spacing is not used. Results are acceptable when the hydraulic diameter is used. The characteristics pertaining to Thermal Conduction Model from [9] used in the Unified Model are given in Table 6.

Table 6 Variables used in Thermal Conduction Model

Thermal conductivity k		
air	0.0318	$Wm^{-1}K^{-1}$
steel	48	$Wm^{-1}K^{-1}$
aluminum	220	$Wm^{-1}K^{-1}$
Mean slope of asperities tan θ	0.05	
R.m.s. height of asperities σ	10^{-6}	m

When the aluminum layers are under tension, the r.m.s. height of the asperities or air gap thickness at the contacts is available from [9,10,18]. When the aluminum layers are under compression and before birdcaging occurs, there is no available data on the effective thickness of the air gap at the contacts. To enable the application of the Unified Model for the stresses in aluminum -10 MPa $< \sigma_A \leq 0$ MPa it is assumed that the effective thickness of the air gap is ten times bigger than that without compression in

aluminum. The contact area in such cases is calculated from the maximum stress which occurred in aluminum during the whole time of exposure, and direct metal contact area is assumed to be equal to zero. The Radial Conduction Model does not describe the heat transfer in a stranded conductor when the birdcaging occurs, and the layers of wires separate from their neighbours. The model can not be used when the aluminum stresses are less than -10 MPa, and therefore, the Unified Model fails under birdcaging conditions. However, the model does predict the onset of conditions leading to birdcaging.

The power loss in each aluminum layer is calculated from the complex values of the layer currents and complex voltage per unit length. The power losses of the steel layers are obtained from the current in the steel core and the axial voltage, assuming a uniform distribution of the steel current.

To combine the Steady-State Heat Transfer Model with other models in the Unified Model, it is assumed that the inclination of the conductor for the calculation of solar heating and convective cooling can be neglected, since its effect is small for the angles up to 60 degrees [16]. The angle between forced and natural flows is taken to be 90°. Although the solar absorptivity and emissivity change with time as the surface of the conductor oxidize and became weathered they are kept constant during the whole time of the exposure, because it is shown that when their values are similar, the influence on the thermal rating is negligible [16].

3.4 PROBABILISTIC APPROACH

The Steady-State Model gives the surface temperature of the conductor at some moment in the lifetime of the conductor, for the applied current and given ambient conditions, and after equilibrium between the heat losses and heat gains is achieved. The time necessary to reach the steady state depends on the thermal inertia of the conductor. The Radial Conduction Model and the Electromagnetic Model are applicable for the particular instant in a conductor life while the input data are valid.

The Mechanical Model predicts the mechanical behaviour of the conductor at some moment during the conductor lifetime based on the loading history of the conductor. The loading history is the summary of the information about the periods in the conductor lifetime with the constant temperature, additional loadings, and for a certain duration. For periods of running out, prestressing and stringing, the tension of the conductor at the beginning of the event is also known. When the actual data for the line are not measured, the loading history may be assumed. The common practice is to apply the design constraints for the line for certain periods of time, for the longest period to assume that the conductor is at a mean daily temperature, and to eventually assume a small percentage of the exposure time at the maximum conductor temperature. This rarely occurs in practice, and leads to the arbitrary prediction of stresses, strains in the conductor and the sag of the conductor.

The thermal history of the conductor has to be known for the calculation of the losses of tensile strength of the nonferrous wires due to annealing. Until now, the loss of strength was computed separately by arbitrarily estimating the wire temperatures.

The Unified Model may utilize a probabilistic method for the evaluation of the

conductor loading and thermal history. Combining all four models in the Unified Model enables the application of a realistic statistical approach for the first time. The Unified Model enables selection of the tensions, temperatures, and duration of running out, prestressing, and stringing periods. The prestressing and tension at the beginning of stringing period are optional. The periods with additional loads such as wind and ice and very low temperatures are optional too. For most of its life the conductor is at a temperature which depend on the current, ambient temperature, and atmospheric parameters, such as wind speed, direction, and solar radiation. The Unified Model calculates the statistical distribution of the actual temperatures of the conductor over that part of the exposure period based on the statistical variation of these parameters. The current, ambient temperature, wind speed and direction, and solar radiation vary simultaneously.

The system current varies with the actual load demands. For continuous loads, the statistical distribution of typical loads with large systems is shown in Fig. 5 [19].

The normal distribution of the probability density function of the ambient temperature is assumed. The probability density function after Morgan [16] is asymmetrical due to the differing distributions for night and day, Fig. 6. If normal distribution is assumed, the standard deviation for day and night is 5 °C for the mean value of approximately 18 °C. The value for standard deviation varies up to 6.3 °C [21].

The statistical distribution of the temperature rise of the surface of the conductor accounts for the statistical distribution of the wind speed, direction, and the solar radiation. The bimodal distribution for night and day is shown on Fig. 7 [22]. This

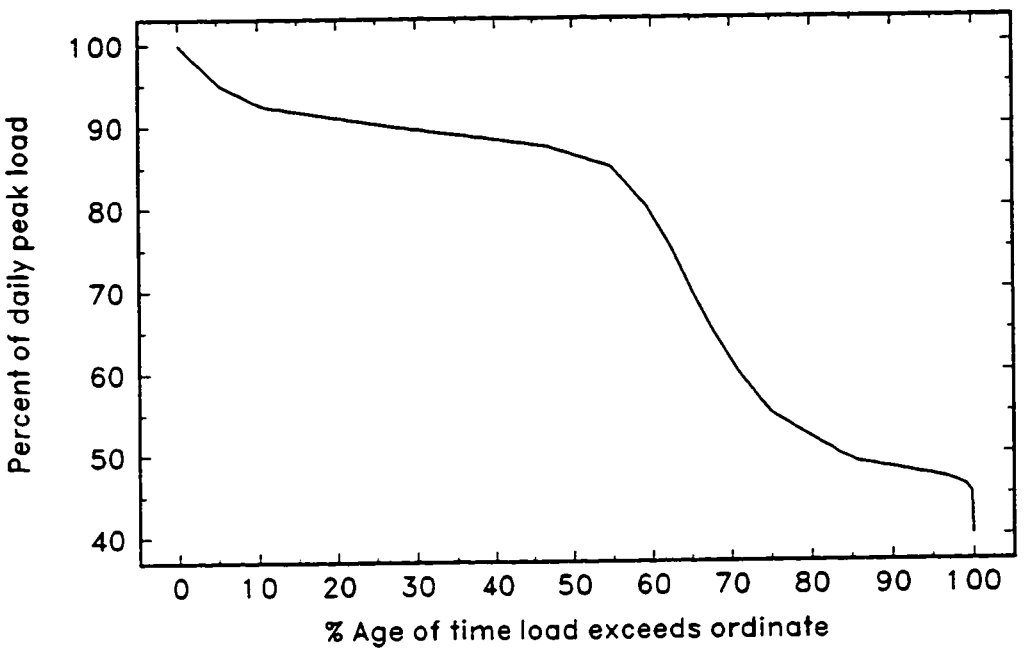

Figure 5 Typical system loads with large systems

probability density function of the temperature rise of the surface of a conductor is used in the Unified Model.

It is assumed that the probability density functions of the temperatures of the layers are similar to that of the surface conductor temperature.

The period of time which the conductor spends at different high temperatures depending on the load current, ambient temperatures, wind speed and direction, and solar radiation is divided into intervals, here called smaller intervals, which correspond to every combination of the probabilities of the peak current, ambient temperature, and maximum temperature rise of the temperature of the conductor. To insure that each interval is long enough to have the steady temperature of the surface of the conductor and

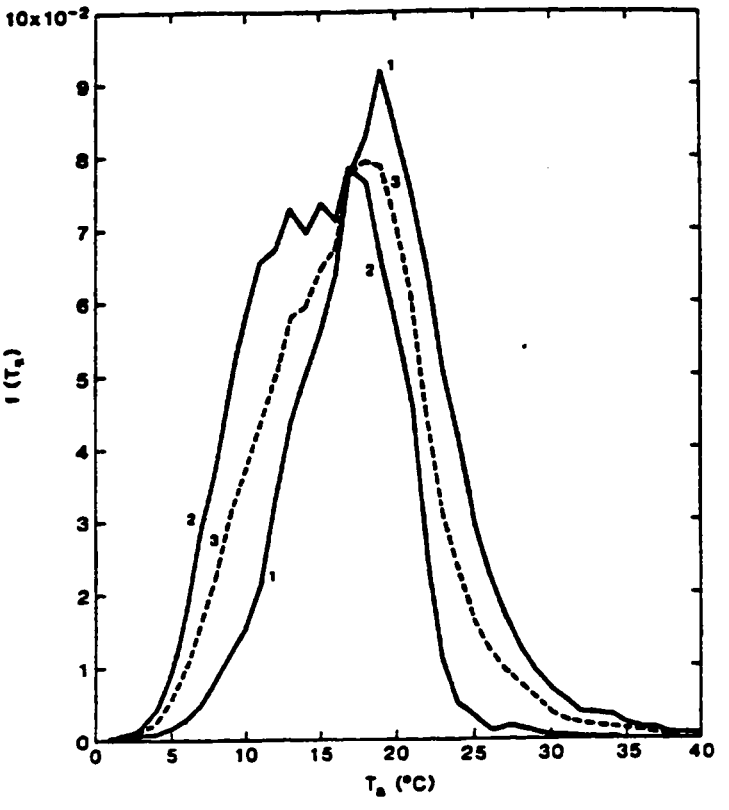

Figure 6 Probability density function of the air temperature for day and night (after Morgan). 10 minute sampling rate.
1. day; 2. night; 3. day and night.

steady temperatures within the conductor, the percentage of the peak load is taken in steps of 10%, the ambient temperature is taken in steps of 5 °C in the range -15 °C to +15°C from the mean value of ambient temperature, and the percentage of maximum temperature rise is taken in steps of 10%.

The Mechanical Model itself can not take account of the realistic loading and thermal history of the conductor. However, the Unified Model enables a realistic probability based evaluation of the conductor history as it combines all four models. For each interval, found from the probabilities of the ambient temperature and current, the Model balances all the common variables, giving the maximum temperature rise for that

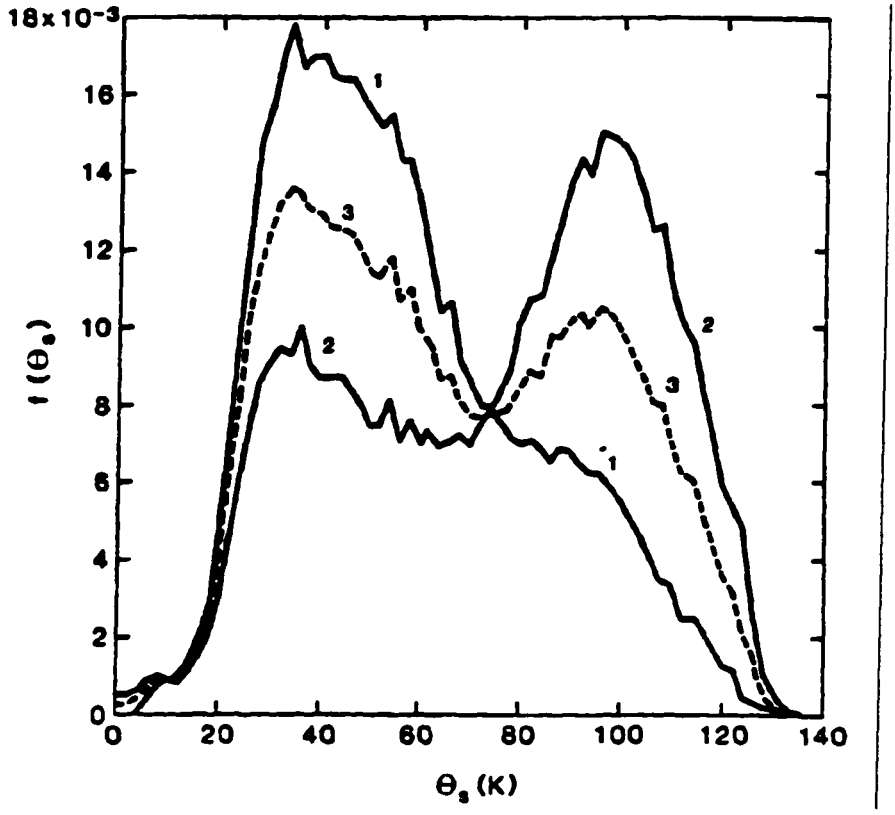

Figure 7 Probability density function of the temperature rise of the conductor (after Morgan). 10 minute sampling rate; 54/7/3.5 mm ACSR (Olive) conductor at 10 m height; I = 1500 A.
1. day; 2. night; 3. day and night.

interval. The statistical variation of the maximum temperature rise may then be considered in smaller intervals.

3.5 THE UNIFIED MODEL

The Unified Model can be used either when the loading and thermal conductor history is evaluated on a probabilistic basis, or when the conductor history is known or conservatively assumed and given as an input. In both cases, the tensions, ambient temperature, and duration for running out and prestressing periods have to be given as

inputs. The prestressing period is optional. If the conductor is clamped without any adjustment in tension and sag and the stringing tension is not fixed, the ambient temperature during stringing and its duration are the inputs. When the stringing tension is fixed, it is given as an input too. Additional loads, i.e. ice and wind, and any other special loads, such as extremely low temperatures, are given as inputs together with the temperature and time of duration. These loading cases usually cover a small percentage of the lifetime of the conductor. In the Unified Model these loading cases are considered prior to other periods. The flow chart of the Unified Model is given in Fig. 8.

When the probabilistic approach is used, the conductor is depicted over its life at various temperatures which depend on the mean ambient temperature and its standard deviation, the maximum (peak) current and its statistical distribution, and the maximum temperature rise of the conductor and its statistical variation. The probability density function is calculated from the given mean ambient temperature and its standard deviation. The probability evaluated period of the lifetime is then divided into the intervals of time corresponding to the ambient temperatures from 15 °C less than the mean ambient temperature to 15 °C larger than the mean ambient temperature in steps of 5 °C. Each interval is further divided into smaller intervals which correspond to the currents from 50% of the maximum current for the whole period to 100% of the maximum current in steps of 10% of the maximum current. Both the currents and the ambient temperatures are taken in an ascending manner.

Starting from the lowest ambient temperature, and the smallest current, the coupling variables in each of these small intervals are equilibrated. The Mechanical Model includes all the cases preceding the probability based period for the first interval.

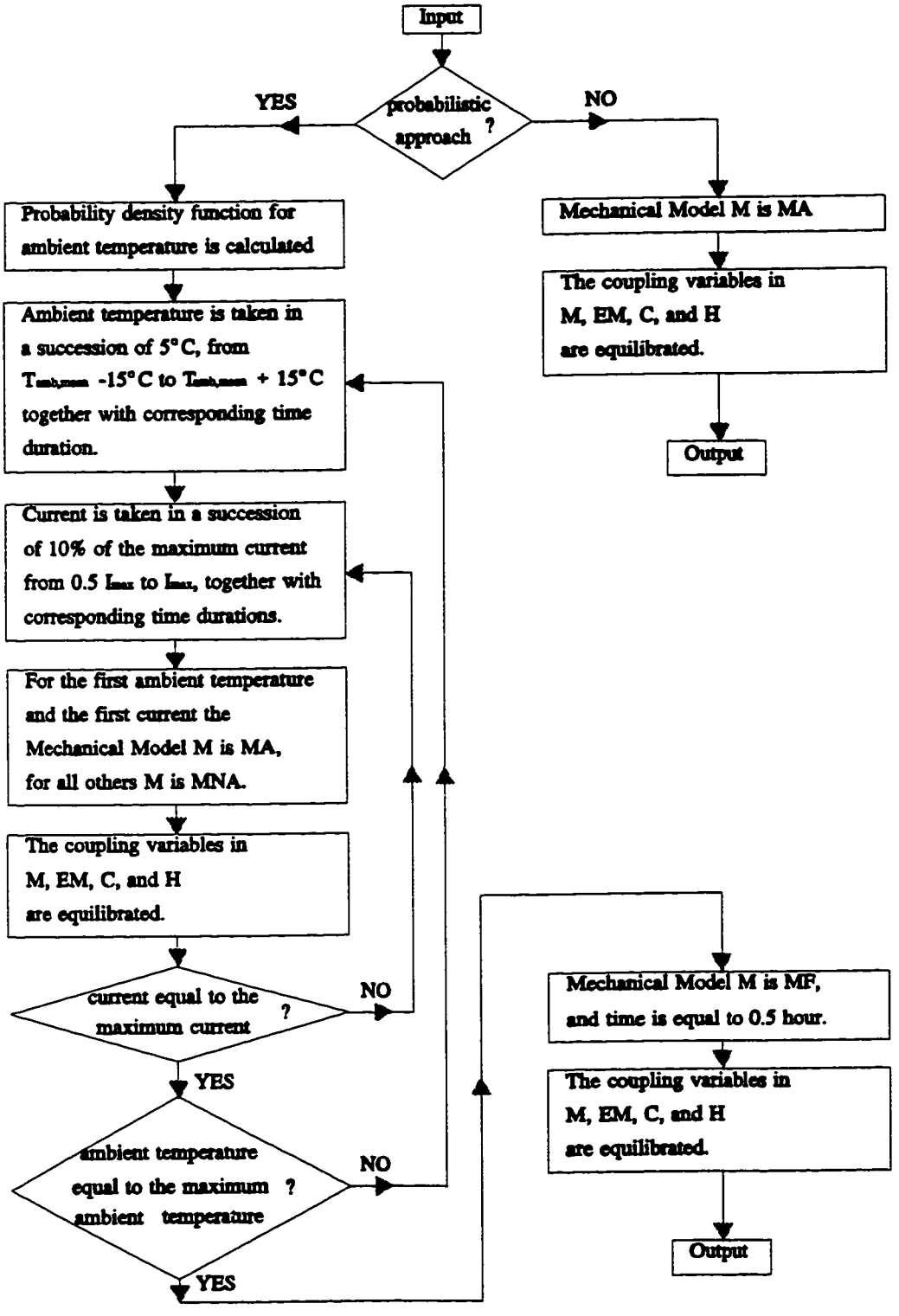

Figure 8 Flow chart of the Unified Model

To avoid unnecessary repetition of these loading cases, they are excluded in succeeding intervals. For each interval, the maximum temperature rise of the conductor is found. To obtain the maximum temperature rise, it is taken in the Steady-State Heat Transfer Model that the number of the day in year $N_d = 182$ for the northern hemisphere, the solar hour of the sun $\omega_S = 0$, and the mean angle of wind attack $\Psi_{mean} = 0°$.

The interval is further divided into the subintervals which correspond to the conductor temperature rises from 10% of the maximum rise to 100% of the maximum rise in steps of 10%. The temperature rise sequence is ascendent too. The loading and thermal history is evaluated when the coupling variables for all intervals in the entire probability based period are balanced, and the cumulative calculation of the creep and settling strains of the aluminum and steel part of the conductor and the annealing of the aluminum layers is done.

The actual electrical, mechanical, and thermal characteristics of the conductor are calculated in a period of half an hour exceeding the probability based period. The equilibration of the coupling variables in the Mechanical, Electromagnetic, Radial Conduction, and Steady-State Heat Transfer Model is done for the input variables corresponding to the actual state. The actual parameters, such as the actual wind speed and direction, current, number of the day in year, and clearness ratio are implemented.

When the probabilistic approach is not employed and the loading and thermal history is assumed, the case with the high temperature is taken as the last one. The coupling variables are balanced for that last period taking into account all the preceding history.

The subroutine for the equilibration of the coupling variables is shown on Fig. 9.

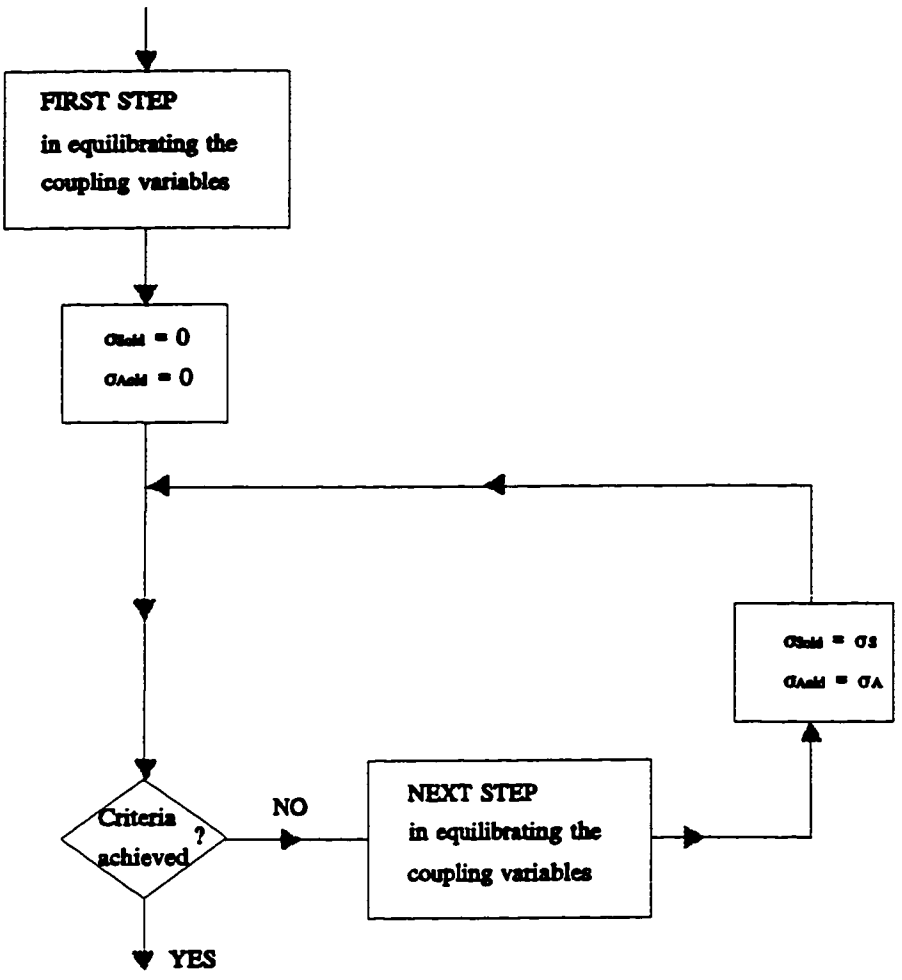

Figure 9 Subroutine for the equilibration of the coupling variables

$$\Delta = \begin{bmatrix} \Delta I_S \\ \Delta I_I \\ \dots \\ \Delta I_N \\ \Delta \nabla \end{bmatrix} = \begin{bmatrix} I_{Sold} \\ I_{Iold} \\ \dots \\ I_{Nold} \\ \nabla_{old} \end{bmatrix} - \begin{bmatrix} I_S \\ I_I \\ \dots \\ I_N \\ \nabla \end{bmatrix} < 10^{-5} \times \begin{bmatrix} 1 + j1 \\ 1 + j1 \\ \dots \\ 1 + j1 \\ 1 + j1 \end{bmatrix}$$

$$| \sigma_{Sold} - \sigma_S | < 10^{-2} \quad MPa$$

$$| \sigma_{Aold} - \sigma_A | < 10^{-2} \quad MPa$$

Figure 10 Criteria for the convergence

The surface temperature of the conductor and the temperature differences between layers are balanced during processing within the First and Next Step. The aluminum and steel stresses σ_A and σ_S and the complex values of the steel current and the currents in the aluminum layers and complex voltage are balanced after every step until the exit criteria are reached. The criteria for balancing are given in Fig. 10. The values of stresses from the previous step are compared with the values from the last step, and their absolute differences have to be less than 10^{-2} MPa. The complex values of the currents and the voltage obtained as the outputs from the two previous iterations of the Electromagnetic Model are compared to achieve a tolerance Δ of less than 10^{-5} times the unit complex vector. When the criterion is achieved, all the coupling variables used either as an input or obtained as an output from any of the four models are equilibrated for that interval. To avoid endless iteration which may occur occasionally, the number of loops is restricted to four.

The First Step in the equilibrating of the coupling variables is shown in Fig. 11. The Steady-State Heat Transfer Model (H) is always linked together with the Electromagnetic Model (EM) in the block HE, where the iterative procedure is engaged to obtain the surface temperature of the conductor. For the block HEF, the first iteration between the Steady-State Heat Transfer Model and the Electromagnetic Model in the interval, and for the Mechanical Model used in the first step, it is assumed that the layer temperatures T_0, $T_1,\ldots,T_{N-1}$, and the steel and aluminum temperatures T_S and T_A are equal to the surface temperature $T_{sur} = T_N$. For all other iterations between the Steady-State Heat Transfer Model and the Electromagnetic Model HES, the temperatures of the layers up to the outer layer N-1, T_0, $T_1,\ldots,T_{N-1}$, which are used as inputs, are calculated

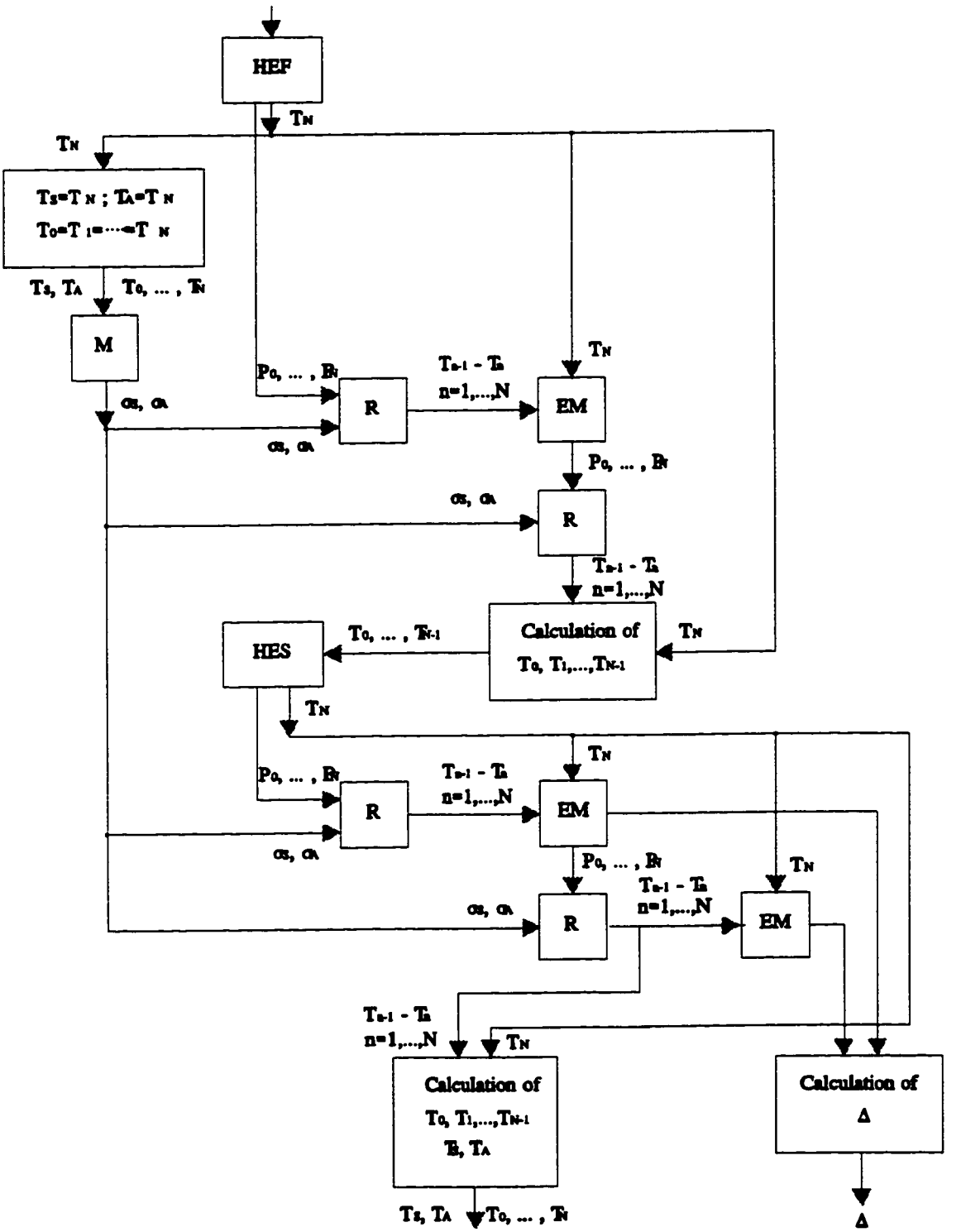

Figure 11 First step in equilibrating the coupling variables

from the last values of the temperature differences between the layers T_{n-1}-T_n, n=1,...,N and the last surface temperature T_N.

The block HEF outputs the surface temperature rise, complex currents and voltage, i.e. power losses in each layer. The Mechanical Model M outputs the stresses in steel and aluminum of the conductor. The Radial Conduction Model R then calculates the temperature rise of each layer, and loops back to the Electromagnetic Model EM to obtain more accurate complex layer currents and voltage, i.e. layer power losses. They are used again by the Radial Conduction Model to calculate more accurate values of layer temperature differences which then, together with the surface temperature result in the more accurate values of the layer temperatures.

Using these temperatures, the next combination of the Steady-State Heat Transfer Model and the Electromagnetic Model HES outputs more precise values of the surface temperature and power losses in each layer. More accurate temperatures of the layers, and consequently more accurate steel and aluminum temperatures are obtained and looped back to the block HES and the Mechanical Model, respectively, in the Next Step in the equilibrating of the coupling variables. The Electromagnetic Model added at the end of the sequence R -EM - R - EM outputs the values of the complex layer currents and the complex voltage for the calculation of the difference Δ which is used as one of the criteria.

The Next Step is presented at Fig. 12. It keeps the same procedure as in the First step with several exceptions. The Next Step uses only the block HES. Temperatures of the layers and the steel and aluminum temperature used as the inputs for the first iteration HES and for the Mechanical Model M are obtained from the preceding step.

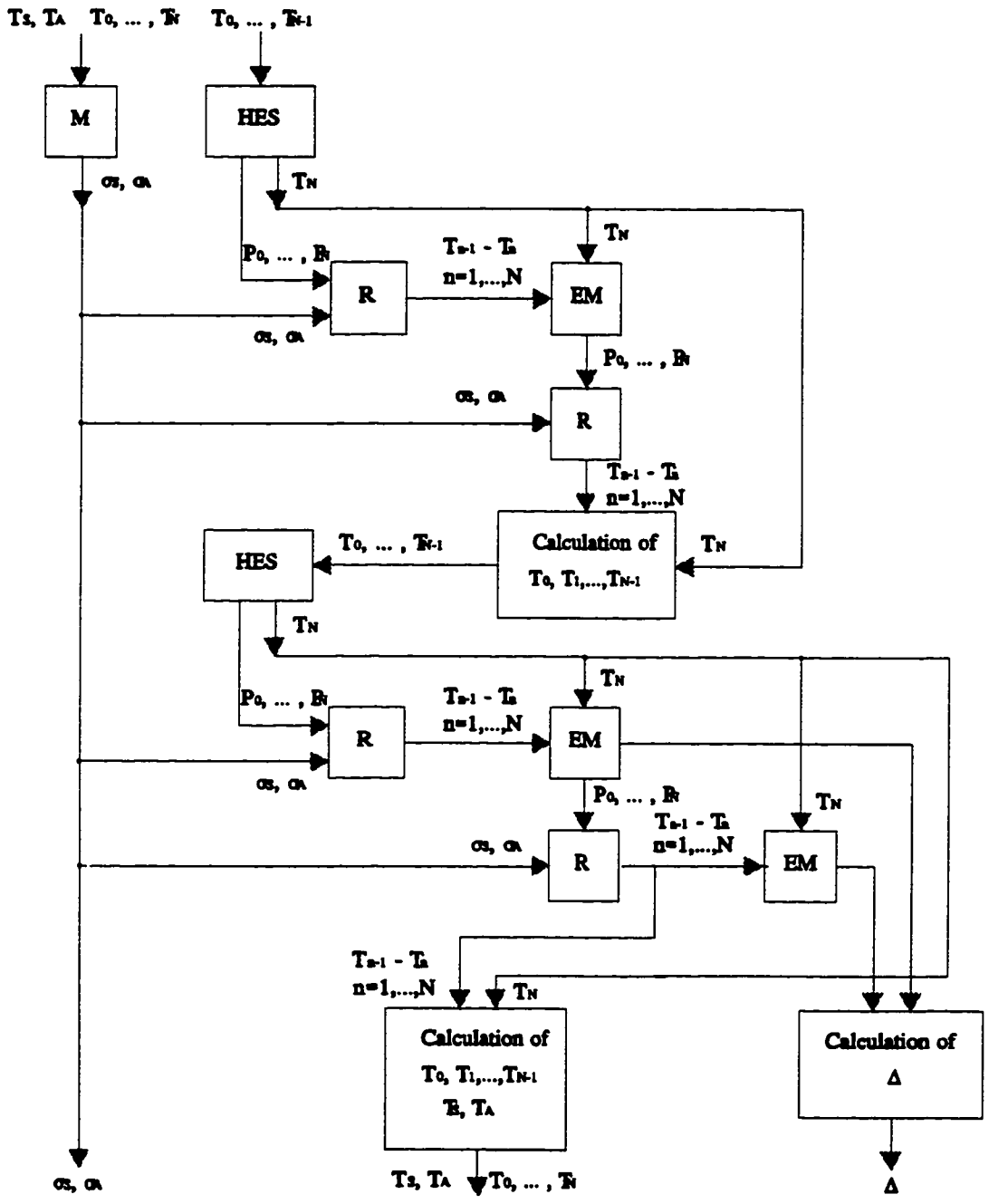

Figure 12 Next step in equilibrating the coupling variables

The stresses σ_S and σ_A of the Mechanical Model are used in the next step for obtaining the other criteria for convergence.

The Mechanical Model, in fact, outputs the stresses in each step based on the outputs of the previous step. For that reason severe criteria for the convergence are imposed.

The structure of the block HEF is shown on Fig. 13. Temperatures of all layers are taken to be equal to the surface conductor temperature. To ensure that the Joule heating P_{JH} obtained from the Steady-State Heat Transfer Model and the power losses P_{EM} obtained from the Electromagnetic Model are equal, the iterative procedure on the surface temperature of the conductor $T_{sur} = T_N$ is employed. The limits of the interval of the iteration are the minimum possible conductor surface temperature for the given conditions and the maximum expected temperature, say 170 °C. The minimum possible surface temperature is obtained by iteration from the Steady-State Heat Transfer Model, so that it corresponds to the Joule heating $P_{JH} = 0$. For the iterations in HEF, and for all other iterations in the Unified Model, the adjusted regula-falsi algorithm is used [36].

The structure of the block HES is shown on Fig. 14. The temperatures of all layers except the outer layer are taken from the previous calculation. The interval of the iteration is decreased, and the limits are closer to the previous temperature of the conductor surface $T_{Nprevious}$. The surface conductor temperature is obtained again by the iteration.

The structure of the Electromagnetic Model E is shown on Fig. 15. To obtain the complex values of the layer currents and the voltage, the complex value of the relative magnetic permeability that matches the modulus of the magnetic field strength

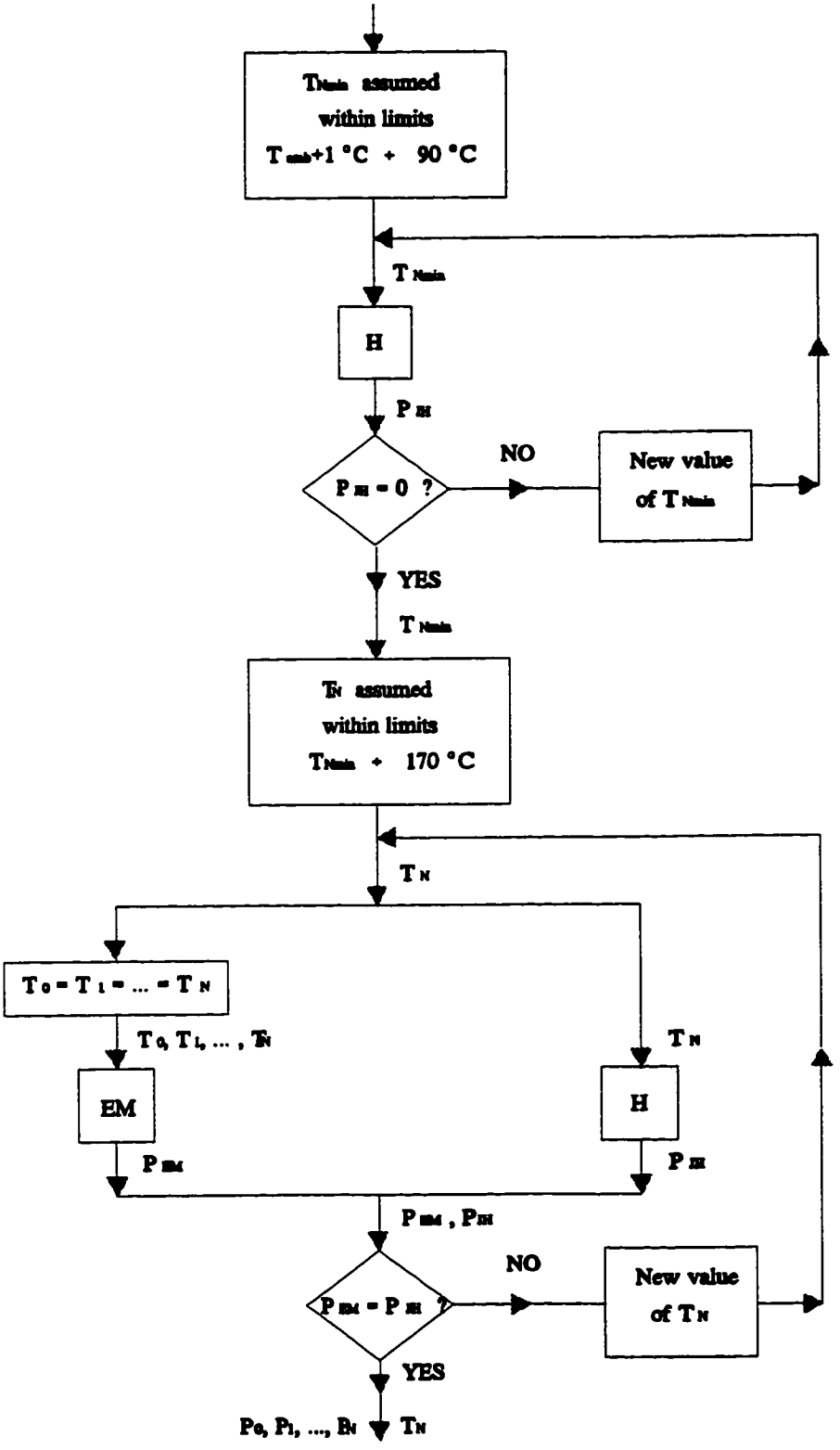

Figure 13 Structure of the block HEF

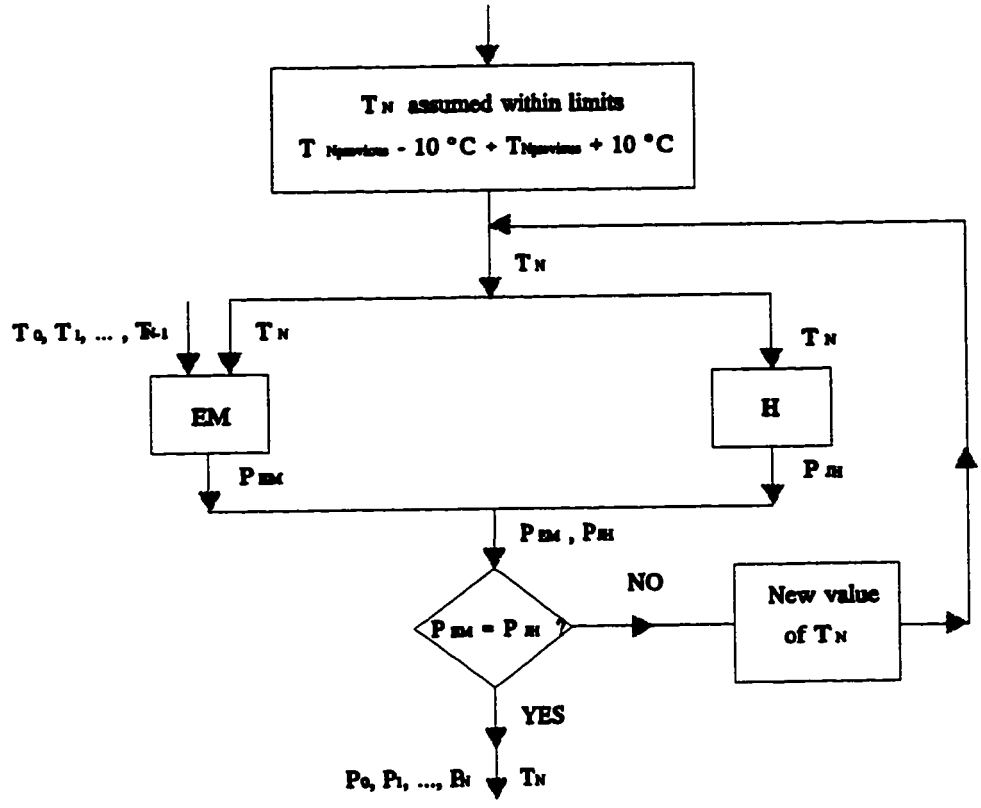

Figure 14 Structure of the block HES

is found by iteration.

The Mechanical Model M is used in the Unified Model in three forms in order to avoid the unnecessary repetition of the whole loading and thermal history of the conductor. The form MA, shown on Fig. 16, includes all loading cases before the period for which the probability based approach is employed and one interval of the probability based period or the loading case which represents the maximum conductor temperature applied without the probability based approach. The alternative which does not include the probability based approach enables the use of the Unified Model for the short periods of exposure, for instance half an hour after the stringing.

The time interval of the probability based period which corresponds to the

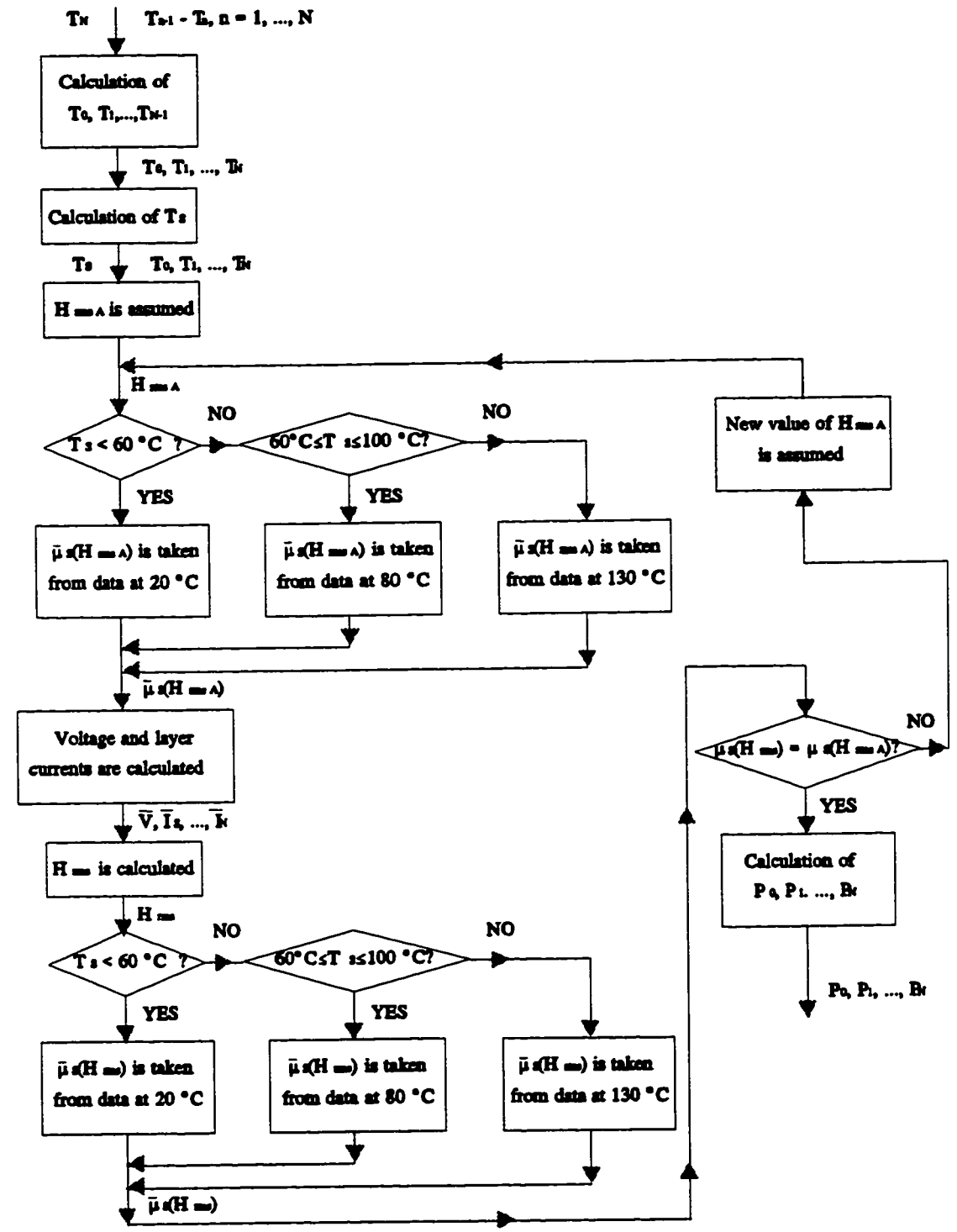

Figure 15 Electromagnetic Model EM.

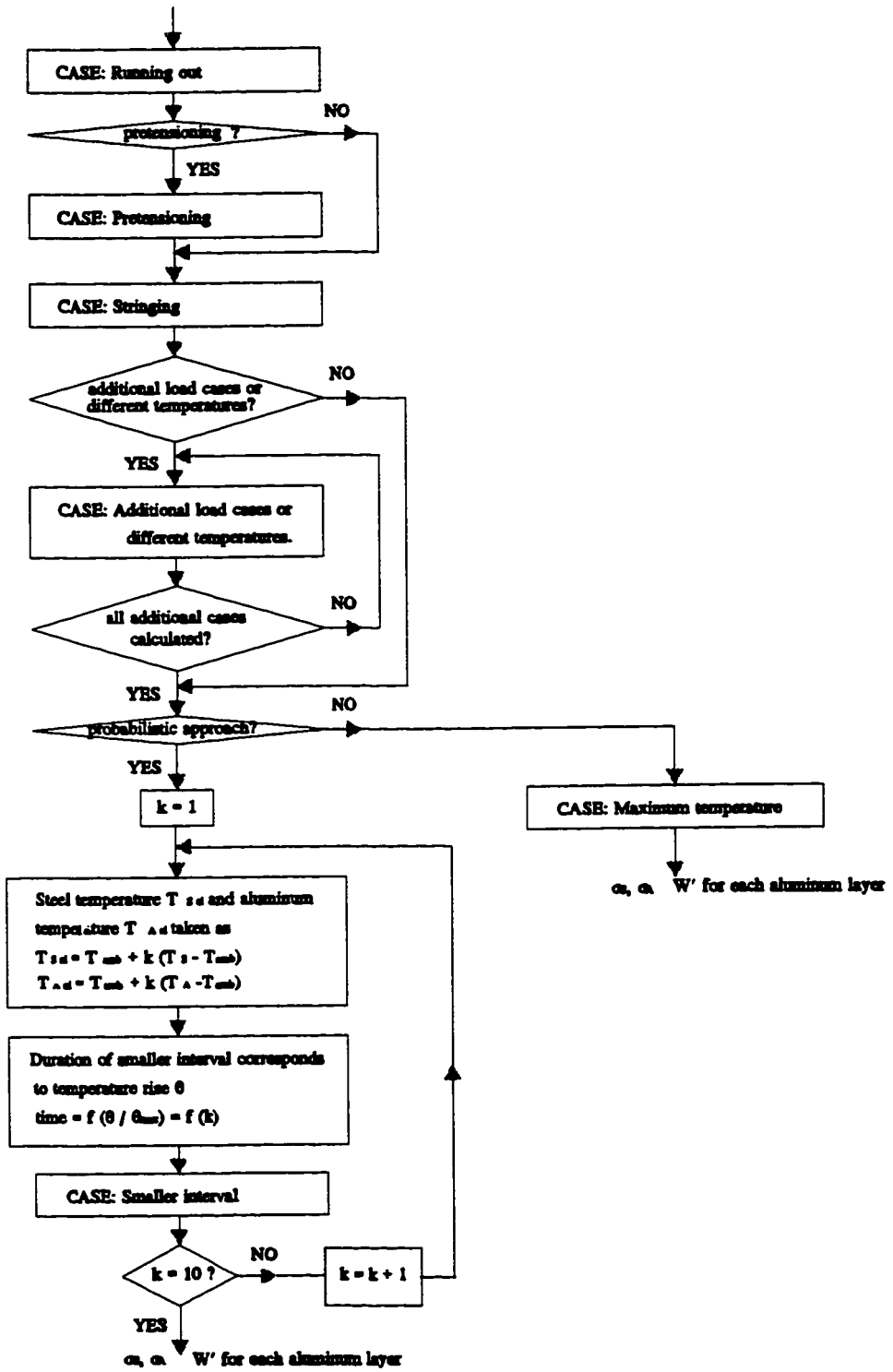

Figure 16 Mechanical Model MA

selected ambient temperature T_{amb} and the selected current is divided further into smaller intervals according to the statistical variation of the temperature rise of the surface of the conductor θ. It is assumed that the layer temperatures T_0, T_1,...,T_N, and consequently the steel and aluminum temperatures $T_{S\,si}$ and $T_{A\,si}$ in a smaller interval follow the same statistical distribution as the temperature rise of the surface of the conductor. The smaller intervals correspond to the temperature rise from 10% to 100% of the maximum temperature rise θ_{max}, in steps of 10%. To avoid introduction of extra variables, the temperature rise is applied in an ascending manner so that the last smaller interval corresponds to the maximum temperature rise. Outputs of the Mechanical Model σ_S and σ_A are the steel and aluminum stresses corresponding to the maximum temperature rise of the conductor for the given ambient temperature and current. These stresses are equilibrated on the larger interval corresponding to the particular ambient temperature and the current, as shown in Fig. 9. At the same time they are used as the coupling variables for obtaining values of the maximum surface temperature and temperature differences, Fig. 11 and 12. If the smaller interval which corresponds to the maximum temperature rise is not the last one, σ_S and σ_A should be memorized and these values used as outputs of the Mechanical Model.

The form of the Mechanical Model MNA, which performs the calculation for only one interval of the probability based period is given on Fig. 17. In a smaller interval the steel temperature $T_{S\,si}$, aluminum $T_{A\,si}$, and the temperatures of the aluminum layers which correspond to the temperature rise of the conductor θ are taken. The form MF used for the final calculation is shown on Fig. 18. Duration of the smaller interval is half an hour and the steel and aluminum temperatures are T_S and T_A.

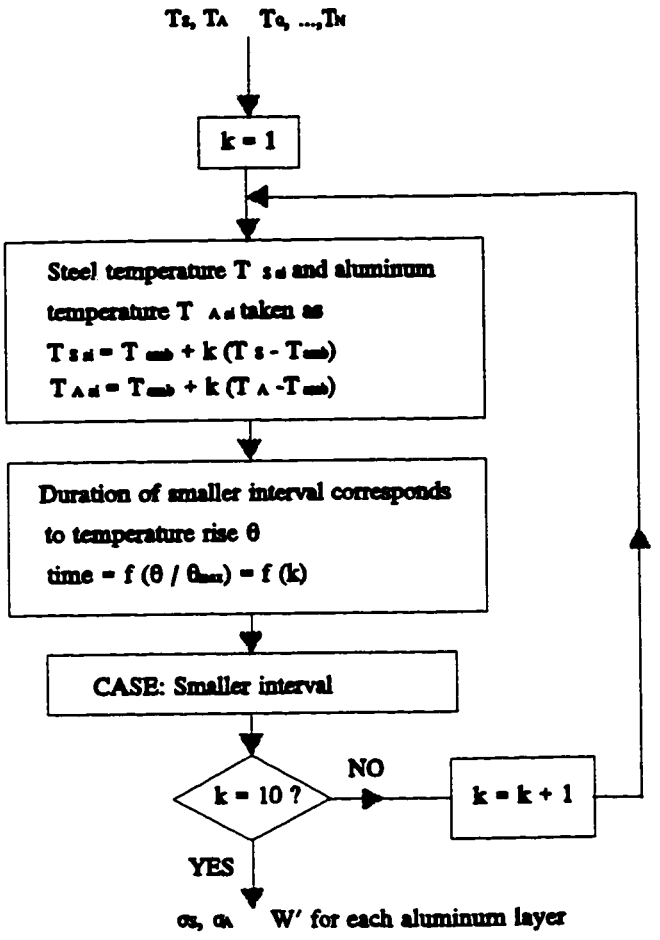

Figure 17 Mechanical Model MNA

The calculation of the loss of tensile strength of the aluminum layers due to annealing is included in the Mechanical Model. For that reason the temperatures of the aluminum layers are necessary. The total period of exposure of the conductor is divided into periods which correspond to the different loading cases. The probability based period is divided into intervals corresponding to each combination of the ambient temperatures and currents. Each of these intervals are divided again into smaller

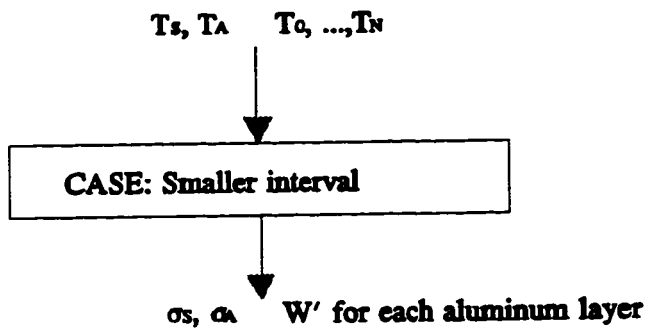

Figure 18 Mechanical Model MF

intervals according to the statistical variation of the maximum temperature rise. Even these small intervals can be divided into subintervals if the duration of the interval is larger than a half year. The cumulative calculation of the loss of tensile strength of the aluminum layers is performed for each of these interludes in parallel with the cumulative calculation of creep and settling strains of the steel and aluminum portions of the conductor. In this way the thermal history of the conductor is found on a probabilistic basis, and the losses of tensile strength of the aluminum layers are predicted in a realistic way for the first time by the Unified Model. For the prediction of the loss of tensile strength of the wires in the aluminum layers, it is assumed that the percentage loss of strength in the fully-annealed state W_a = 56%, and the coefficients are $A'=8.62$, $B'=110$, $C'=-5000$, and $D'=7.5$ [21], page 52.

If the duration of the loading cases is longer than half a year, it is divided into subintervals not exceeding half a year. The flow chart for the Case in the Mechanical Model is given in Fig. 19. The steel strain X_S for each subinterval is found by an

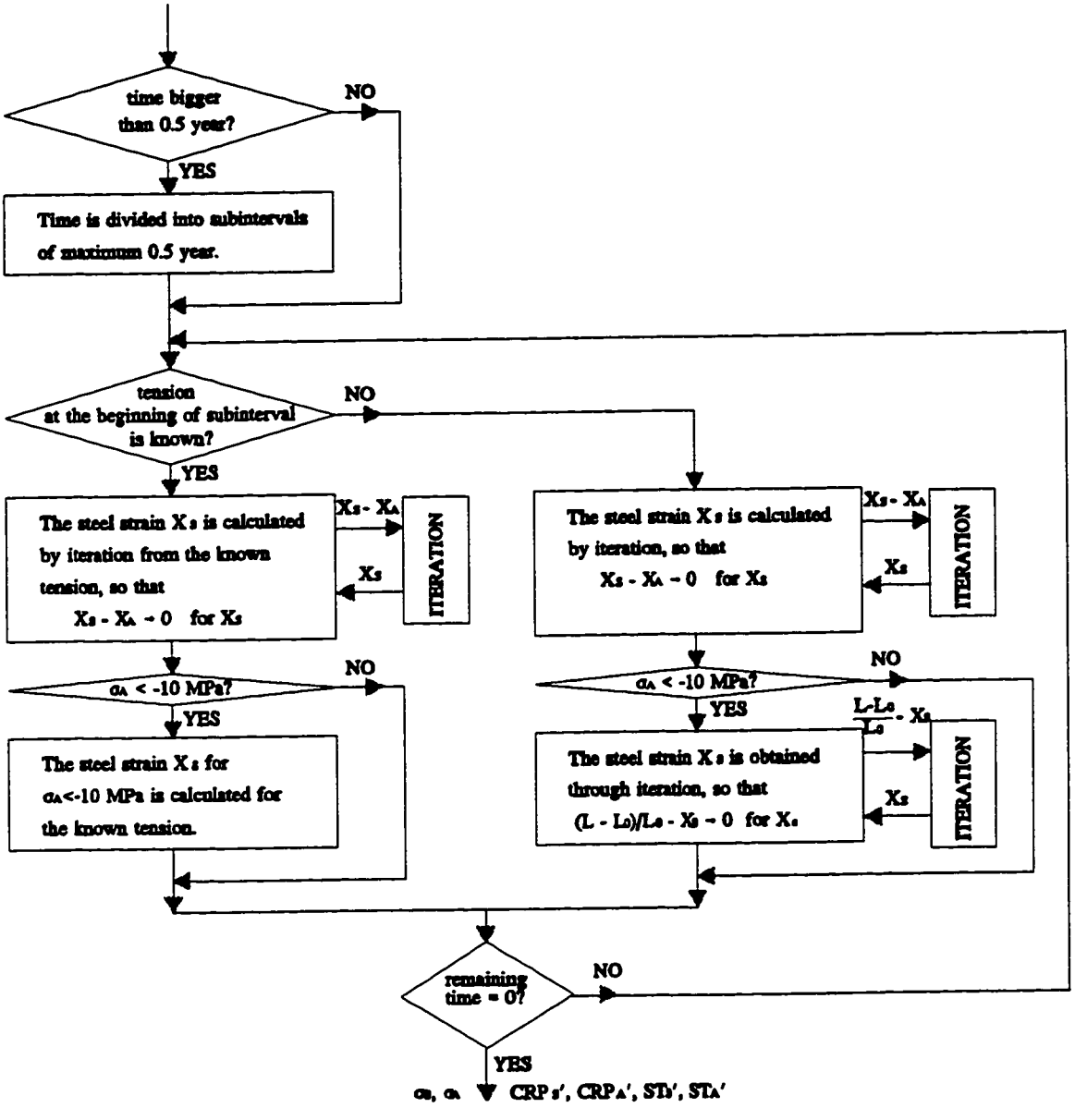

Figure 19 Structure of the CASE in the Mechanical Model

iterative procedure so that at the end of the subinterval the total steel strain is equal to the total aluminum strain $X_S = X_A = X$. The result of birdcaging is predicted even though not used in the Unified Model, otherwise the conductor strain, sag, and steel stress are calculated. At the end of each case, the stresses, cumulative creep and settling

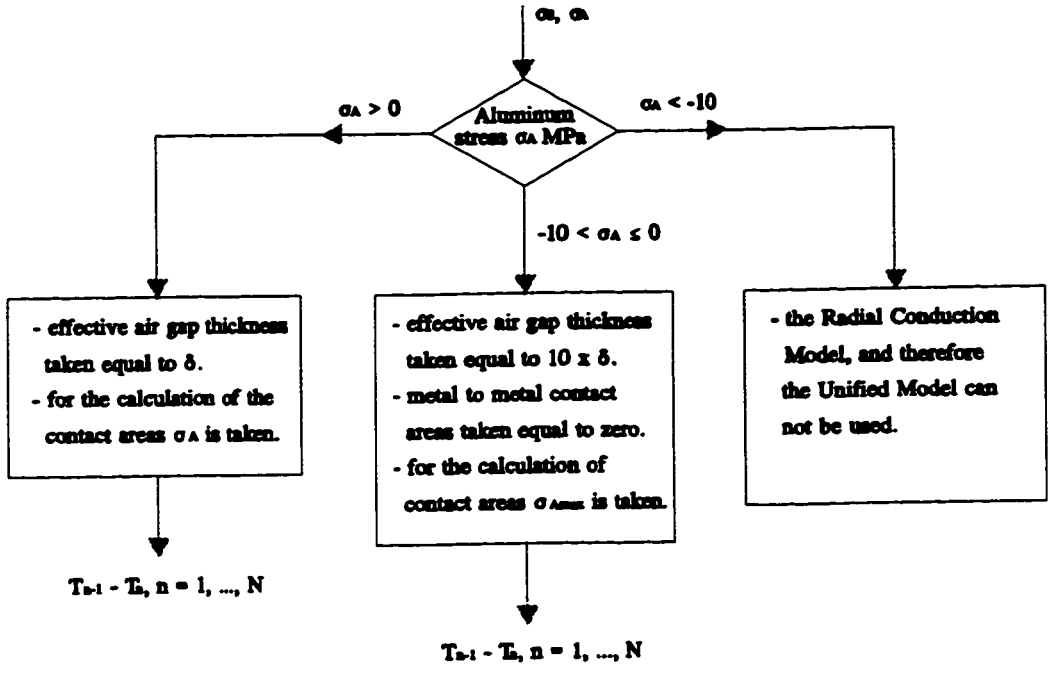

Figure 20 Radial Conduction Model

strains in aluminum and steel, and all other outputs of the Mechanical Model, such as sag, are obtained.

A flow chart for the Radial Conduction Model is shown in Fig. 20. When aluminum is under compression, without birdcaging, i.e. -10 MPa $< \sigma_S \leq$ 0 MPa, the contact areas are calculated using the maximum stress in aluminum σ_{Amax}. Although the stress in aluminum is bigger at the beginning of the interval, for this purpose the stress from the end of the period or interval in which the maximum stress occurs is taken.

3.6 APPLICATION OF THE UNIFIED MODEL

The Unified Model has been implemented for 54/19 Grackle ACSR conductor. Values for the input variables used in the Model are shown in Table 7. Construction of

the conductor and the characteristics of materials used in the Model are shown in Table 8. Unless otherwise stated, these input variables apply to all the results.

The loading history of the conductor is taken in a sequence: running out period, stringing period, one period with the additional load - ice with wind, and the probability based period. As the duration of the running out and stringing periods is two hours, the total exposure time is in fact the duration of the additional load case period and the probability based period. Pretensioning is not considered. The actual period is taken after the probability based period.

When the tension is given at the beginning of the period, it is assumed to be the horizontal component. Only the horizontal dead-end span is considered. It is assumed that the actual current and the maximum current for the probability based period are the same, although this as well as all other input variables can easily be changed.

The permeability curve shown on Fig. 3 is implemented for 20 °C [2]. For the temperatures 80 °C and 130 °C the permeability curves are obtained from the data for the modulus of the relative permeability of a 2.76 mm galvanized steel wire at 50 Hz and 0 MPa, after Morgan [16]. These curves are the only published data for 2.76 mm wire at high temperatures and are used at 60 Hz, although there is some difference between 50 Hz and 60 Hz. Moduli of magnetic permeability are split into the real and imaginary components using the data for the magnetic loss tangents at 80 °C and 130 °C for the galvanized steel wire with the diameter of 3.19 mm and stress 0 MPa [1]. The real and imaginary components of the relative permeability are then multiplied by the shielding factors at 80 °C and 130 °C for the galvanized steel wire with the diameter of 3.19 mm and the stress 0 MPa [1]. The data for the magnetic loss tangent and shielding factor

Table 7 Standard input variables used in the Unified Model

Variable	
Actual solar hour	0°
Actual clearness ratio	1
Actual number of day in year	182
Actual current	A
Actual ambient temperature	20 °C
Actual wind speed	0.6 m/s
Actual wind angle to axis	0°
Air pressure	101.3 kPa
Air gap at contacts	1 μm
Albedo	0.26
Altitude	Sea level
Azimuth	0°
Clearness ratio for the probability based period	1
Frequency	60 Hz
Ice thickness	6.35 mm
Latitude	44° 00'N
Maximum current for a probability based period	A
Mean ambient temperature for the region	20 °C
Running out tension (20 % of RTS)	37288 N
Span length	400 m
Standard deviation of mean ambient temperature	6.3 °C
Standard deviation of wind angle	15 m/s
Stringing tension (20 % of RTS)	37288 N
Stringing temperature	20 °C
Temperature at running out	20 °C
Temperature for addit. load case (ice and wind)	0 °C
Time duration of actual period	0.5 hour
Time duration of probability based case	99% of 10 years
Time duration of additional load case	1% of 10 years
Time duration of running out	1 hour
Time duration of stringing	1 hour
Total exposure time	10 years
Wind pressure for additional load case	385 Pa
Wind angle to axis for a probability based period	0°
Wind speed for a probability based period	0.6 m/s

Table 8 Construction of the conductor and characteristics of materials used in the Unified Model

Variable	
Absorptivity	0.9
Bare weight of conductor	22.38 N/m
Coeff. of linear expansion of aluminum	22.8×10^{-6} 1/°C
steel	11.3×10^{-6} 1/°C
Conductor diameter	33.9 mm
Crossectional area, conductor	680.84 mm^2
aluminum	604.26 mm^2
steel	76.58 mm^2
Dc resistances at 20°C, aluminum	0.02818 $\Omega mm^2/m$
steel	0.1775 $\Omega mm^2/m$
Diameter of steel wire	2.27 mm
Diameter of aluminum wire	3.77 mm
Elasticity modulus, aluminum	55 GPa
steel	190 GPa
Emissivity	0.95
Lay lengths, steel	0.150, 0.1874 m
aluminum	0.2916, 0.365, 0.4 m
Number of wires in layers	1, 6, 12, 12, 18, 24
Number of layers, steel	1 + 2
aluminum	3
Temperature coefficient of resistance, aluminum	0.00404 $°C^{-1}$
steel	0.0032 $°C^{-1}$
Yield stress, aluminum	140 MPa
steel	530 MPa

for wire 3.19 mm are used because there are no published data for the wire 2.76 mm for temperatures 80 °C and 130 °C. The variations of the real and imaginary parts of the relative permeability at the temperatures 80 °C and 130 °C with magnetic field strength which are acquired as described and used in the Unified Model are given in Table 9.

Table 9 Variation of the real and imaginary parts of the permeability at the temperatures 80 °C and 130 °C with magnetic field strength

H_{rms}	80 °C		130 °C	
	Re (μ_s)	Im (μ_s)	Re (μ_s)	Im (μ_s)
0.0	70	0	80	0
71	75	4	90	5
141	90	9	104	12
212	108	19	124	31
283	123	30	131	47
354	136	45	158	81
424	156	59	188	136
495	181	64	379	481
565	245	247	521	657
636	398	481	590	696
707	438	525	646	743
848	548	565		

CHAPTER 4

RESULTS

The Unified Model produces information related to all aspects of the behaviour of the conductor. The sensitivity of such parameters as the heat gains and losses, temperatures of the layers, currents and stresses, ac resistance and power losses, sag and the rate of loss of tensile strength due to annealing for any of the input variables can be readily determined. The influence of the mean ambient temperature, exposure time, ice thickness and the duration of the additional load case, air gap thickness, and the span on the electrical, thermal, and mechanical characteristics of the conductor are examined.

The results are given for the range of currents from 200 A to 1400 A. For currents larger than 1400 A the calculation can not be done, as birdcaging occurs in some of the intervals of the probability based period, which correspond to the higher ambient temperatures. The temperature of the aluminum part of the conductor is approximately 135 °C when birdcaging occurs at the aluminum stress -10 MPa under standard conditions.

Fig. 21 shows the variation of the temperature rise of the king wire and aluminum layers of the conductor above ambient temperature with current. The temperature difference between the king wire and the surface is 14.9 °C for 1400 A, which is 15.9 % of the temperature rise of the conductor surface. The biggest temperature difference

occurs between the third (outer) and second (middle) aluminum layer. For 1400 A the temperature difference between third and second aluminum layer is 10.7 °C , between second and first aluminum layer 3.6 °C, between first aluminum layer and third steel layer 0.5 °C, and between third steel layer and the king wire 0.1 °C. The temperature difference increases with the increasing current.

The variation of the magnitude of currents in steel core and aluminum layers with total current is presented on Fig. 22. The curves are not smooth because of the use of only three sets of the permeability data for a wide range of steel temperatures. However, the trend suggests that the increase of the layer currents with total current may be linear.

Fig. 23 shows the variation of the current density of the steel core and aluminum layers with current. The current density in the second aluminum layer is the same as in the outer aluminum layer and 3 % higher than in the inner aluminum layer for 200 A. The current density in the second layer is 34 % higher than in the outer layer and 44 % higher than in the inner layer for 1000 A. Again the curves are not smooth, showing clearly that the temperature of the steel core is less than 60 °C for the currents 200 and 400 A, between 60 °C and 100 °C for the currents 600, 800, and 1000 A, and more than 100 °C for 1200 and 1400 A (Fig. 31). The importance of accurate data for the relative magnetic permeability for the corresponding steel temperature for the prediction of the current redistribution within the layers is obvious.

Fig. 24 presents the variation of the loss of tensile strength of aluminum layers with current. The loss of tensile strength of the inner aluminum layer is 4.6 % bigger than the loss of tensile strength of the outer aluminum layer for the current 1400 A. The difference increases with increasing current as the temperature difference between layers

increases.

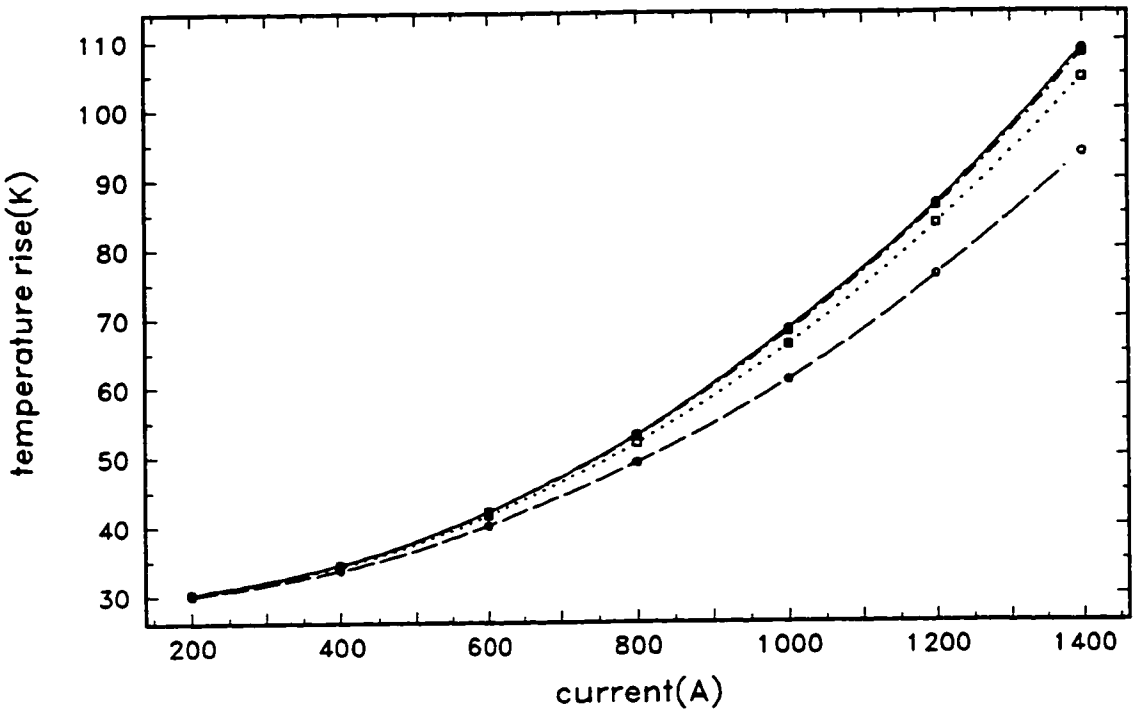

Figure 21 Variation of the temperature rise of the conductor with the current.
_____ king wire _ _ _ _ 3rd aluminum layer
..... 2nd aluminum layer ._._._. 1st aluminum layer

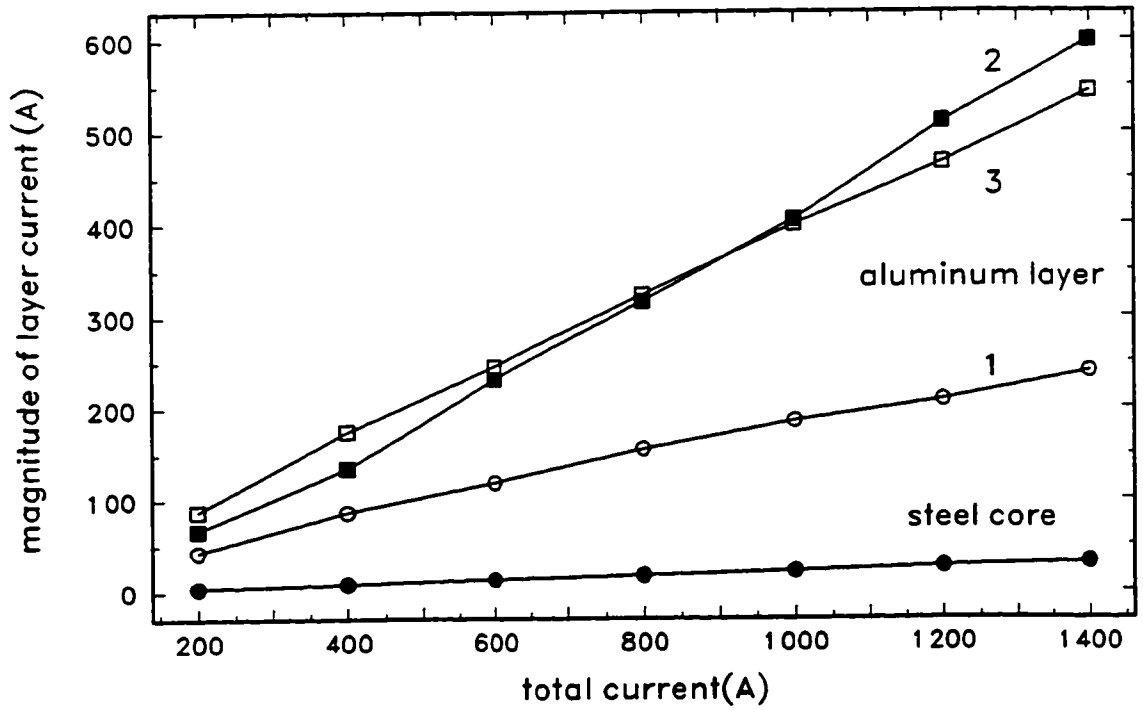

Figure 22 Variation of the magnitude of layer currents with total current.

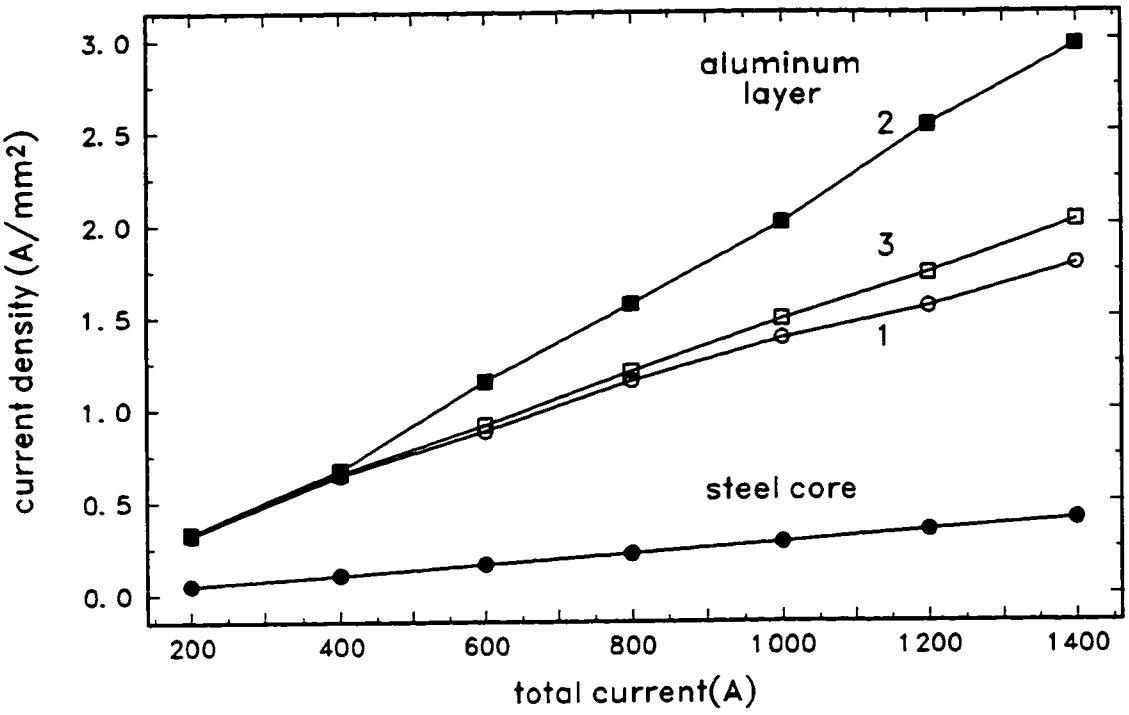

Figure 23 Variation of the current density in layers with current.

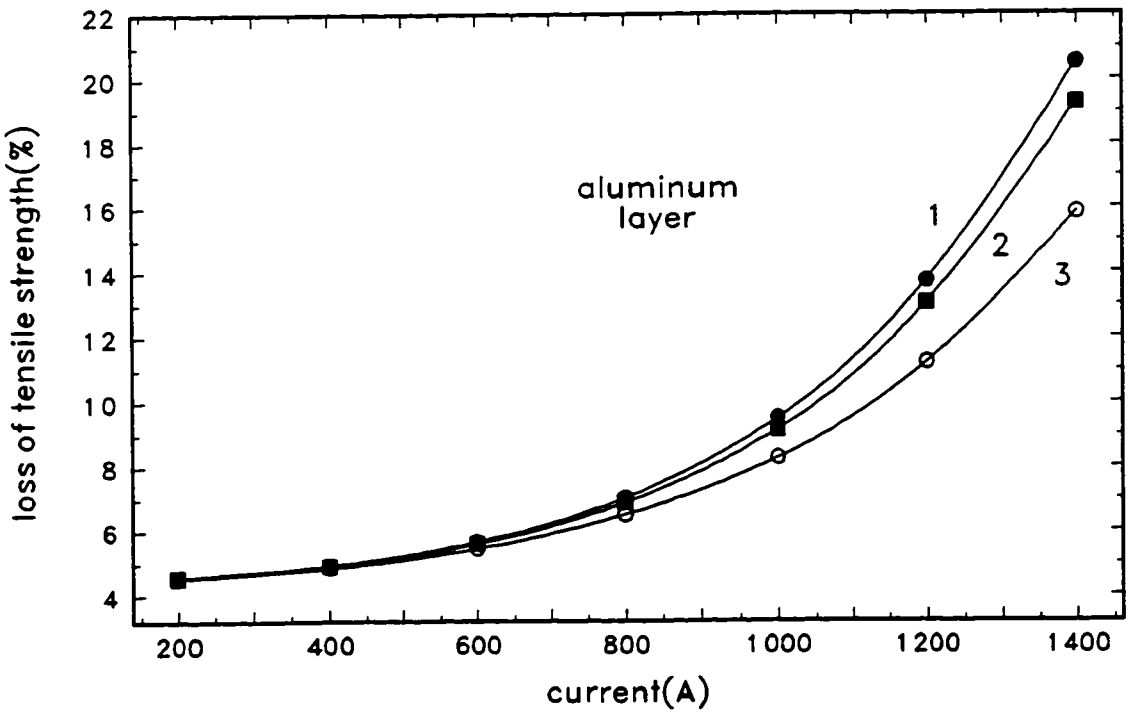

Figure 24 Variation of the loss of tensile strength of aluminum with current.

4.1 AMBIENT TEMPERATURE

To investigate the influence of the ambient temperature on the conductor parameters, the mean ambient temperature is taken for three conditions: 0 °C, 10 °C, and 20 °C.

Various losses are plotted against current for these three cases in Fig. 25. It is seen that the heat losses and gains change with current and ambient temperature. The convective P_{con} and radiative heat losses P_R and heat gain due to Joule losses P_J increase with increasing current. The convective cooling decreases with an increase of ambient temperature, as the temperature rise of the surface of the conductor decreases with the increase of the ambient temperature for the same current. Both the radiative cooling and Joule heating increase with an increase of the ambient temperature. Joule losses increase with increasing current at the higher rate than exponential, because the ac resistance of the conductor increases with increasing current too. The Joule losses for 1400 A increase by 3.2 W/m when the ambient temperature increase from 0 °C to 10 °C and from 10 °C to 20 °C, which is 2.3 % of the Joule losses at 20 °C.

The variation of the Joule losses with the surface temperature rise and ambient temperature is presented in Fig. 26. The Joule losses increase with an increase of ambient temperature for the same temperature rise of the surface of the conductor. The increase is bigger for higher ambient temperatures.

Fig. 27 shows the variation of the difference of the temperatures between the king wire and surface with current. Up to 1000 A the temperature difference between the king wire and the surface increases almost exponentially with current, being larger for larger ambient temperatures. The curve for ambient temperature 20 °C changes the

slope at current 1200 A, and the curves for 10 °C and 0 °C at current 1400 A. The reason for that is shown in Fig. 28. The aluminum stress at these points is less than 0 MPa and it is assumed in the Radial Conduction Model that the air gap thickness for the aluminum layers under compression is 10 times bigger than the air gap for aluminum with tension. It would be logical that the temperature difference between the king wire and surface increases at a higher rate when aluminum compression occurs, than it is when the aluminum is under tension. Either the air gap thickness for the layers under compression is bigger than 10 δ or the area of metal to metal contacts calculated from the maximum aluminum stress is too big. These assumptions obviously underestimate the temperature difference between the king wire and surface when aluminum compression occurs.

The variation of current density for the steel core and aluminum layers with the corresponding core and layer temperature rises is shown in Fig. 29. The current density in each layer shows the same trend of change with the temperature rise of that particular layer for all ambient temperatures.

From Fig. 30 it can be seen how the ac resistance changes with current and ambient temperature. The curves are not smooth because the permeability curves for three temperatures are available only, so that each curve is used for a large range of temperatures. Fig. 31 shows the variation of the steel temperature with the current. The permeability data taken for the calculation of the ac resistance of the conductor corresponds to the steel temperature for the given current. The tendency of the curves in Fig. 30 shows an increase in R_{ac}. Taking into account the steel temperatures from Fig. 31, it appears that the ac resistance increases exponentially with increasing current

for a fixed ambient temperature. The resistance increases almost linearly at 0.16×10^{-5} Ω/m with a rise of ambient temperature of 10 °C for the fixed current.

Fig. 32 presents the variation of the steel and aluminum stresses with the current and ambient temperature. The aluminum stress decreases and the steel stress increases with current, as the aluminum transfers the load to the steel due to increasing temperatures. The steel stresses increase, and aluminum stresses decrease with the increase of the ambient temperature for the fixed current.

It is seen from Fig. 33 that the horizontal tension of the conductor decreases almost exponentially after 500 A with an increase of current. The horizontal tension decreases by 1 kN at 200 A and 0.8 kN at 1400 A, which is approximately 3 % when the ambient temperature increases from 0 °C to 10 °C. It decreases by 0.9 kN and 0.7 kN, or approximately 3 % when the ambient temperature increases from 10 °C to 20 °C, for the currents 200 A and 1400 A, respectively.

The variation of the horizontal tension of the conductor with temperature rise of the core is given in Fig. 34. The horizontal tension decreases with the increase of the temperature rise of the core. It decreases with the increase of the ambient temperature, and the decrease is bigger for the smaller temperature rise of the core.

The variation of the total sag with current and ambient temperature is presented in Fig. 35. It will be noted that the sag increases linearly with increasing air temperature, but increases exponentially with increasing current.

It is seen from Fig. 36 that the sag increases almost linearly with increasing temperature rise of the steel core above 40 K for a fixed ambient temperature, and with increasing ambient temperature for the fixed value of the temperature rise of the steel

core. For example, the sag at the ambient temperature 0 °C for 110 K temperature rise of the core is only 8 cm larger than it would be with the linear change.

The loss of tensile strength of the inner aluminum layer due to annealing with current and ambient temperature can be seen in Fig. 37. The cumulative loss of tensile strength increases linearly with increasing ambient temperature for a fixed current. The loss of tensile strength increases approximately exponentially with increasing current.

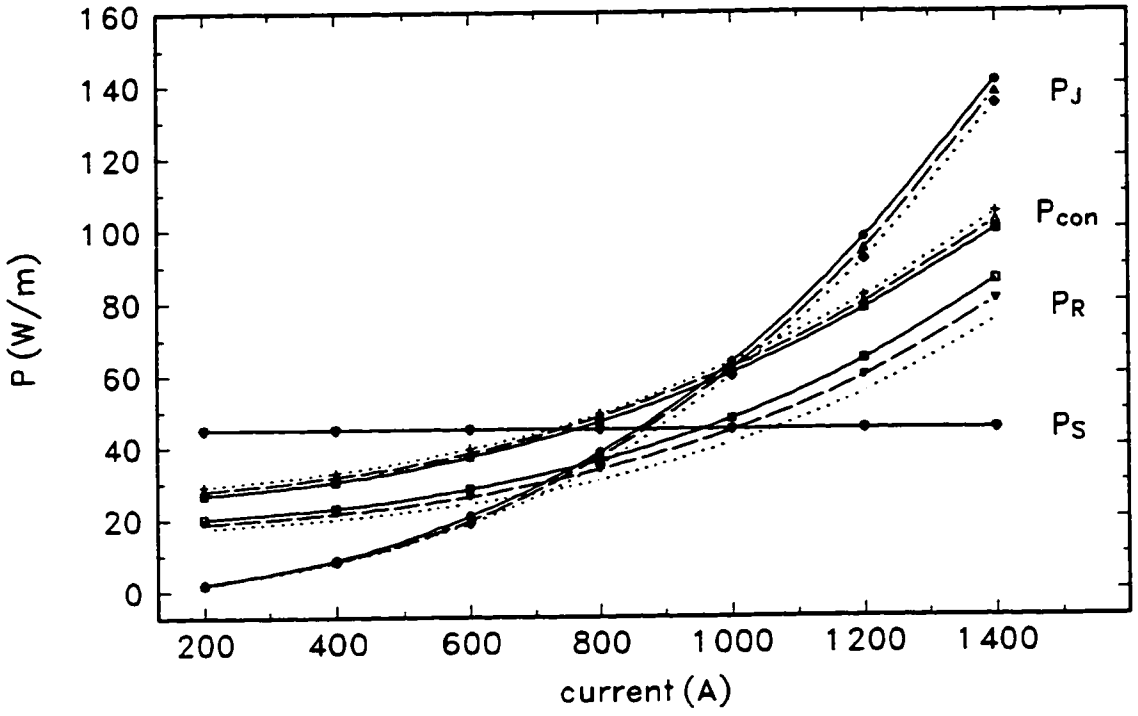

Figure 25 Variation of the heat gains and losses with current and ambient temperature at

_____ 20 °C _ _ _ 10 °C ..... 0 °C.

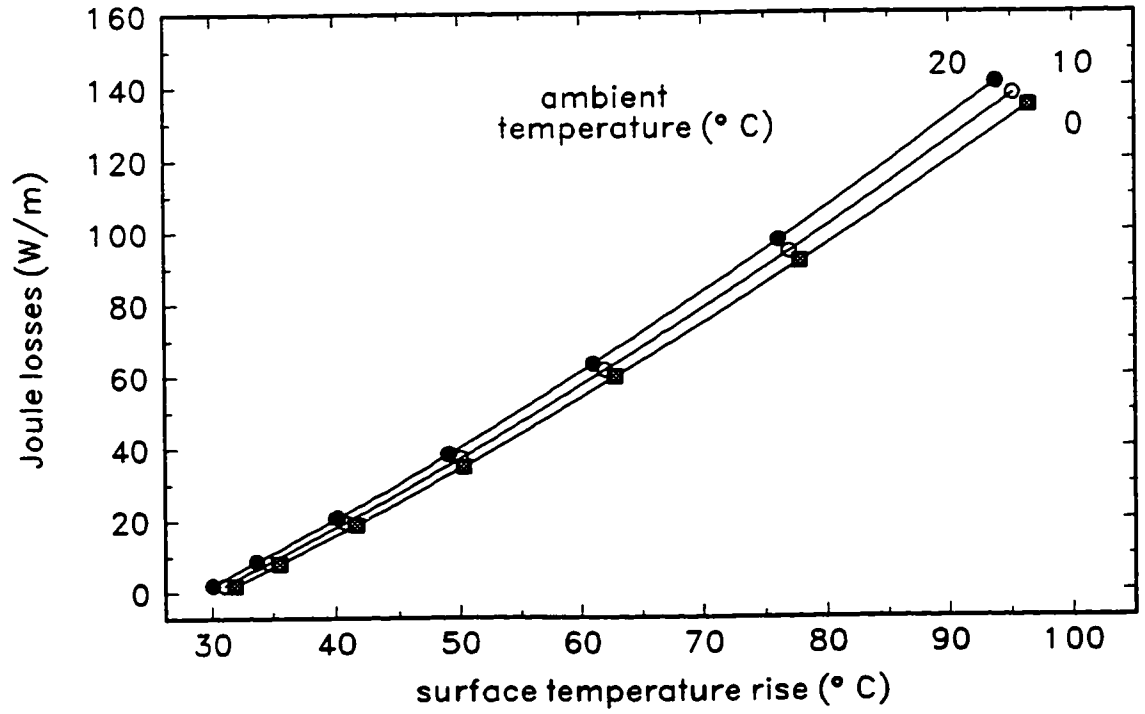

Figure 26 Variation of the Joule losses with the temperature rise of the surface of the conductor and ambient temperature.

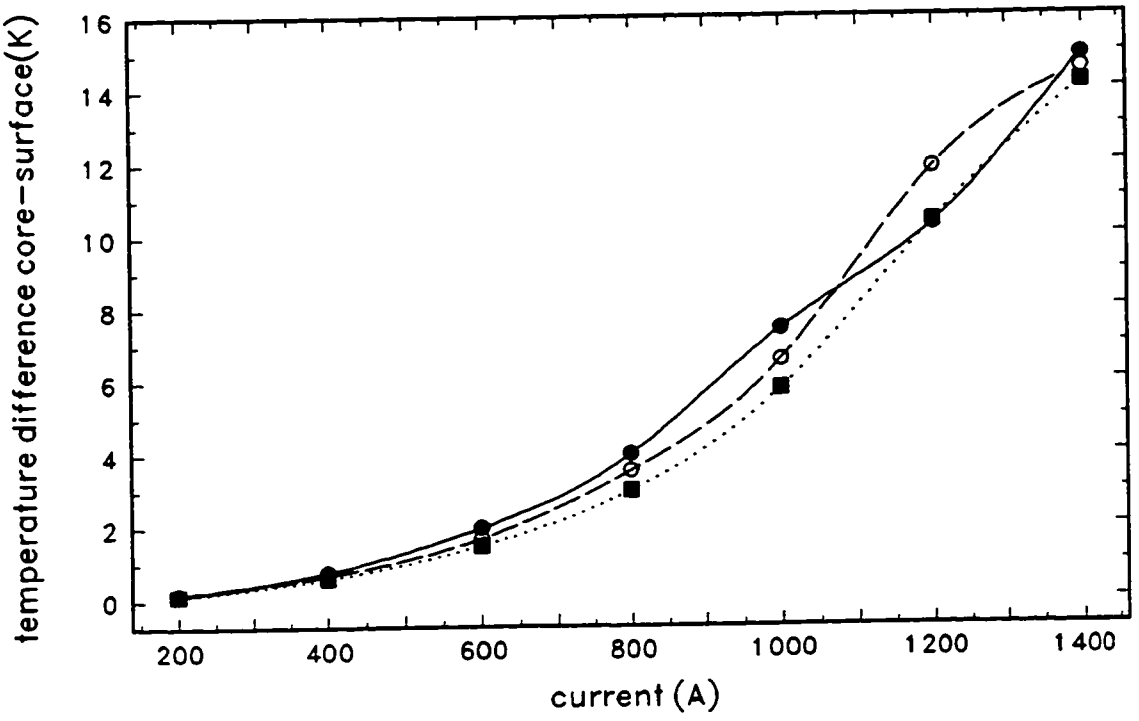

Figure 27 Variation of the difference of the temperatures between the king wire and surface with current and ambient temperature
_____ 20 °C _ _ _ 10 °C ..... 0 °C.

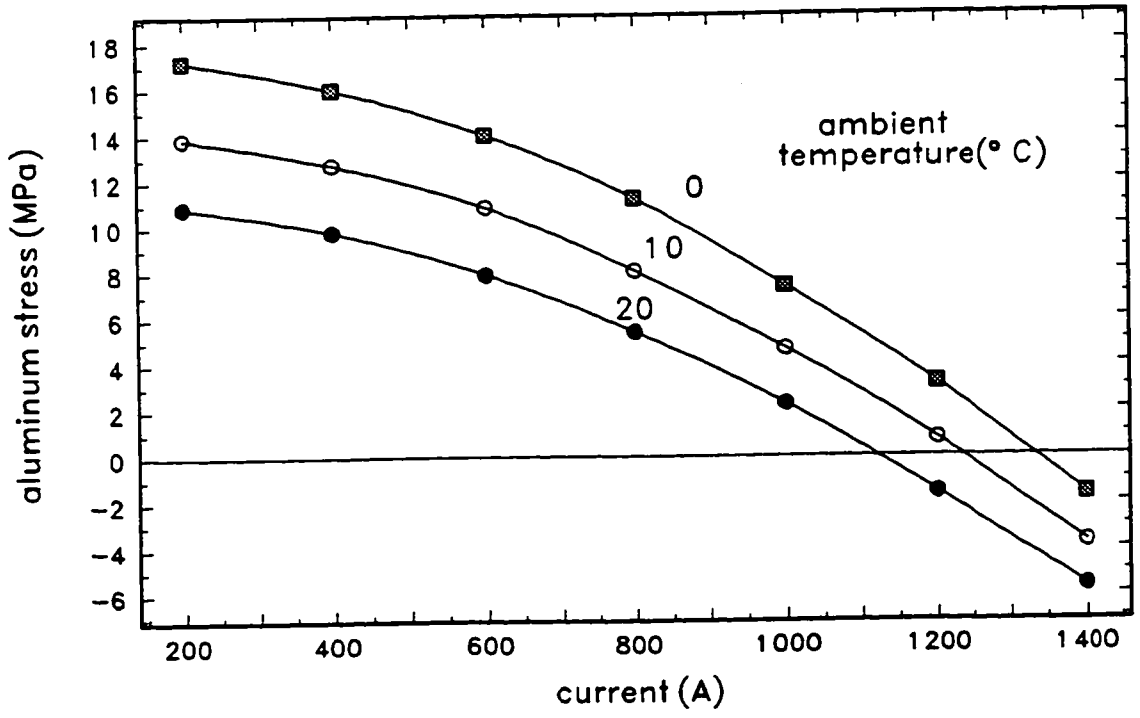

Figure 28 Variation of the aluminum stress with current and ambient temperature.

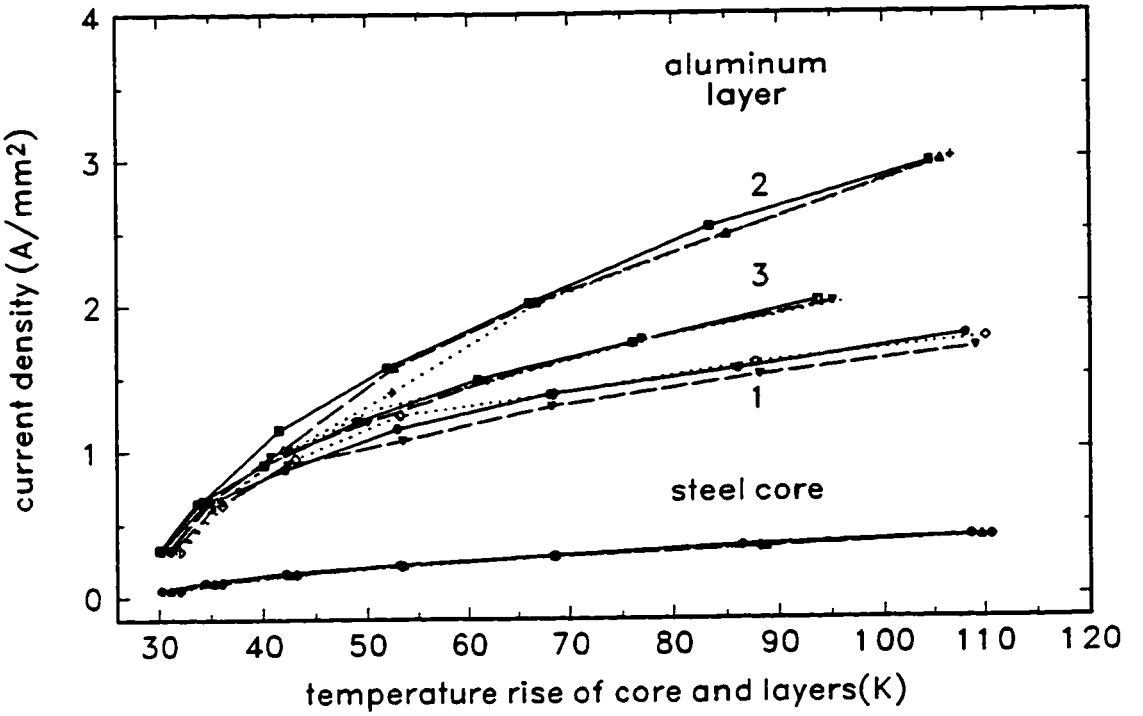

Figure 29 Variation of the current density in steel core and aluminum layers with temperature rise of the core and aluminum layers and ambient temperature
_____ 20 °C _ _ _ 10 °C ..... 0 °C.

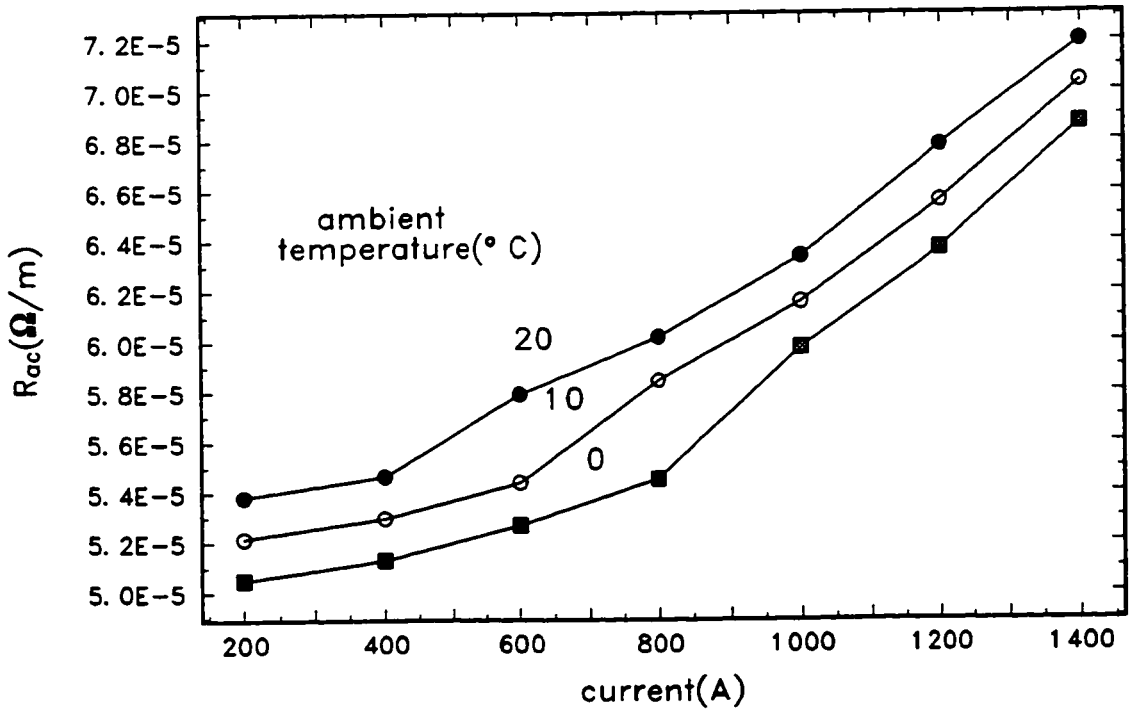

Figure 30 Variation of the ac resistance of the conductor with current and ambient temperature.

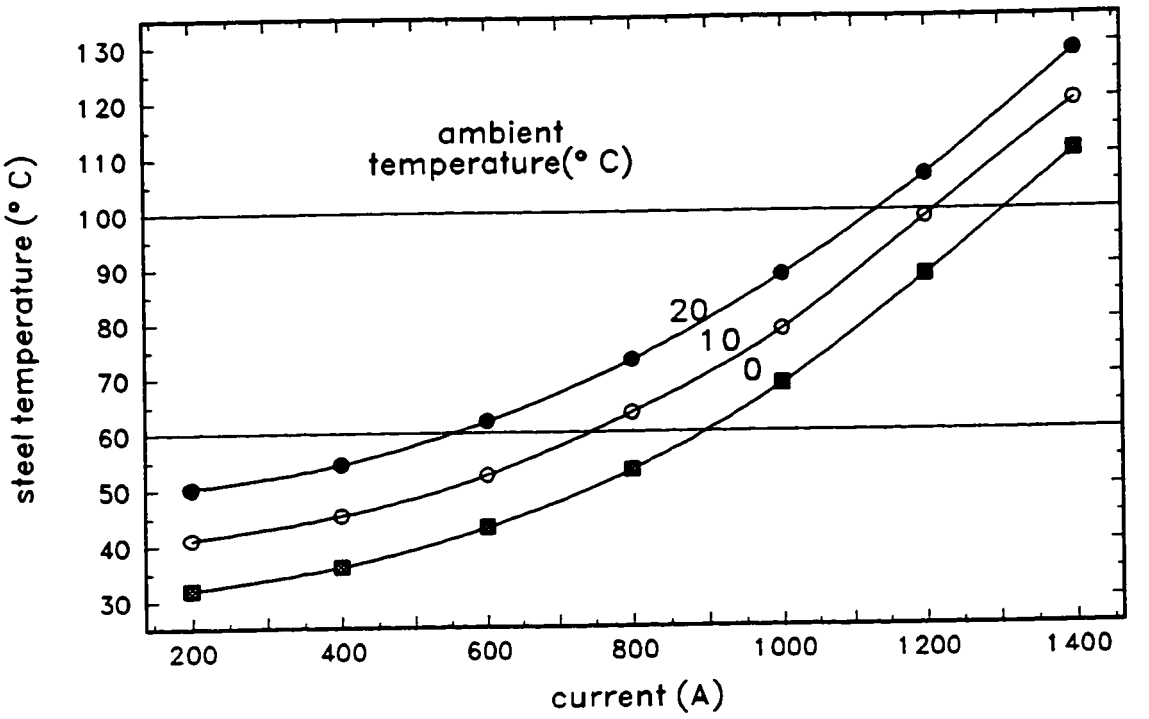

Figure 31 Variation of the steel temperature with current and ambient temperature.

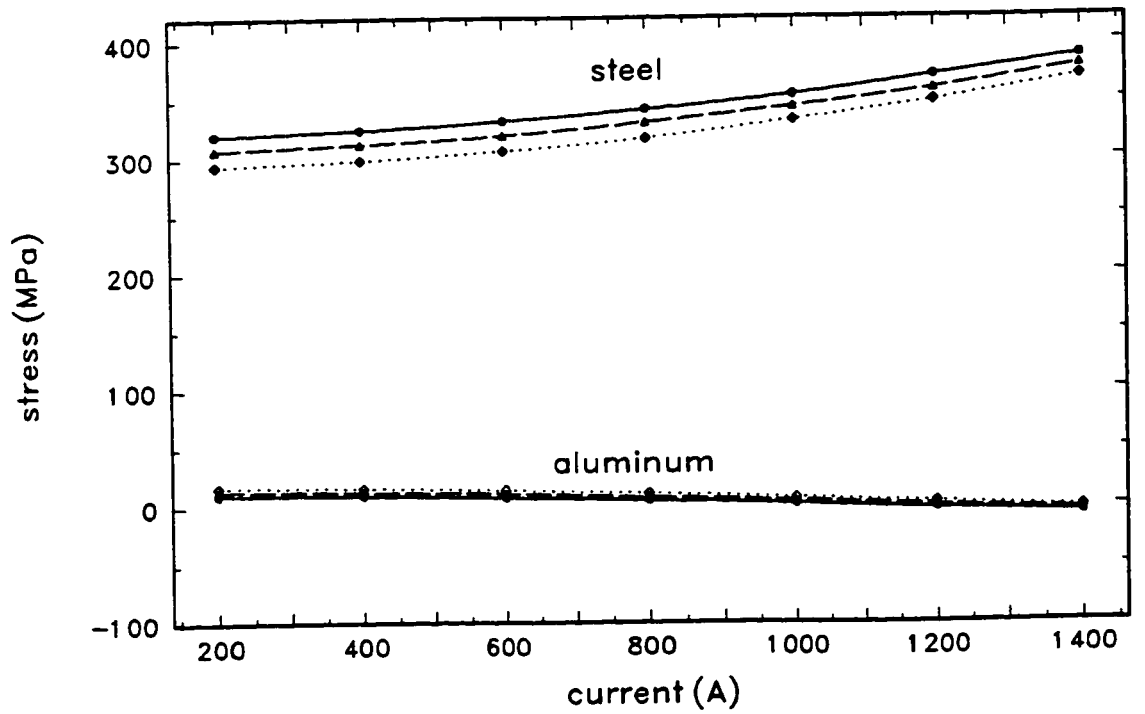

Figure 32 Variation of the steel and aluminum stress with the current. Ambient temperature

_____ 20 °C _ _ _ 10 °C ..... 0 °C.

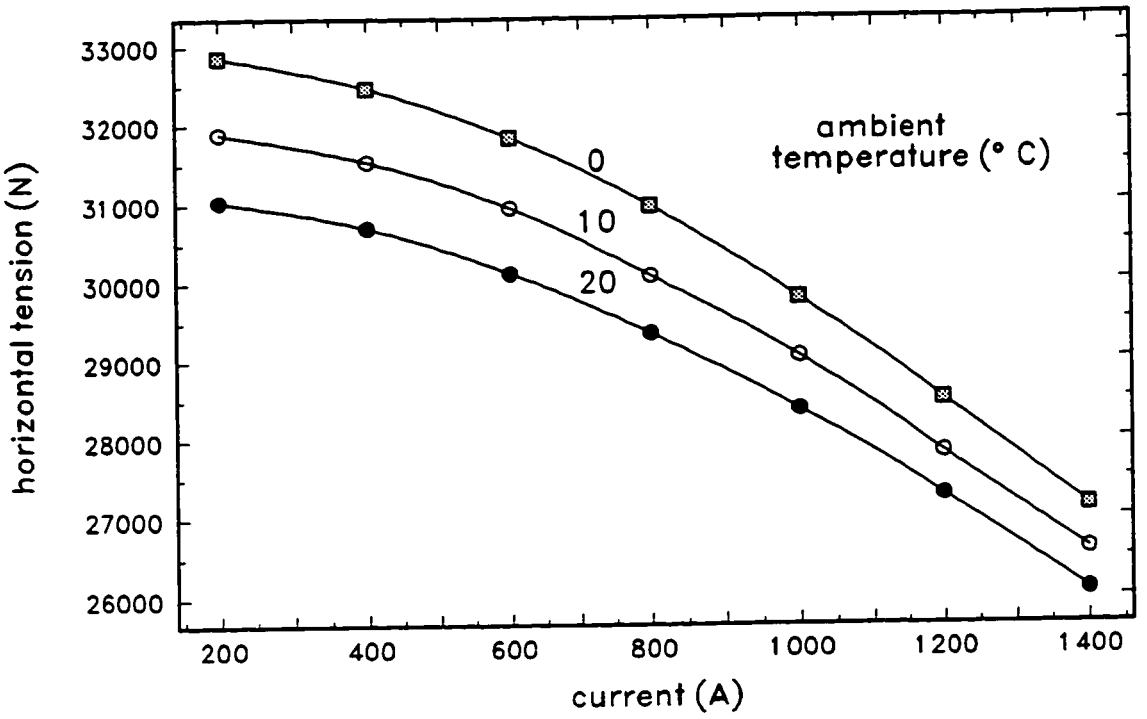

Figure 33 Variation of the horizontal tension of the conductor with the current and ambient temperature.

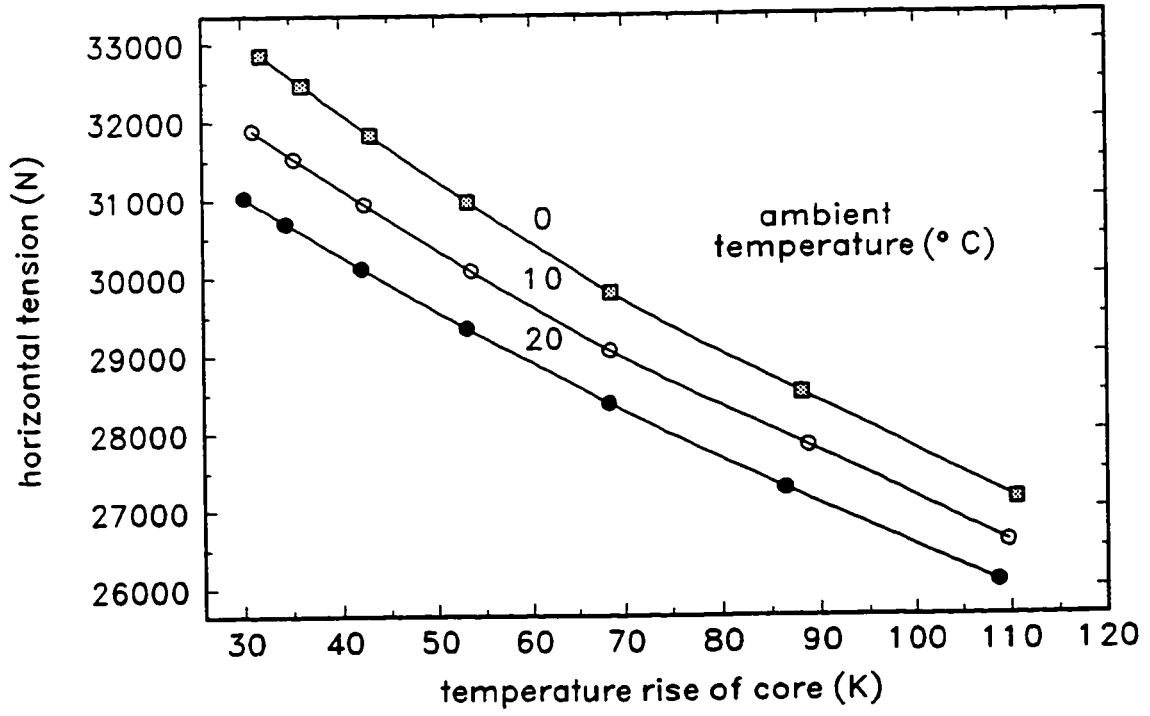

Figure 34 Variation of the horizontal tension of the conductor with the temperature rise of the core and ambient temperature.

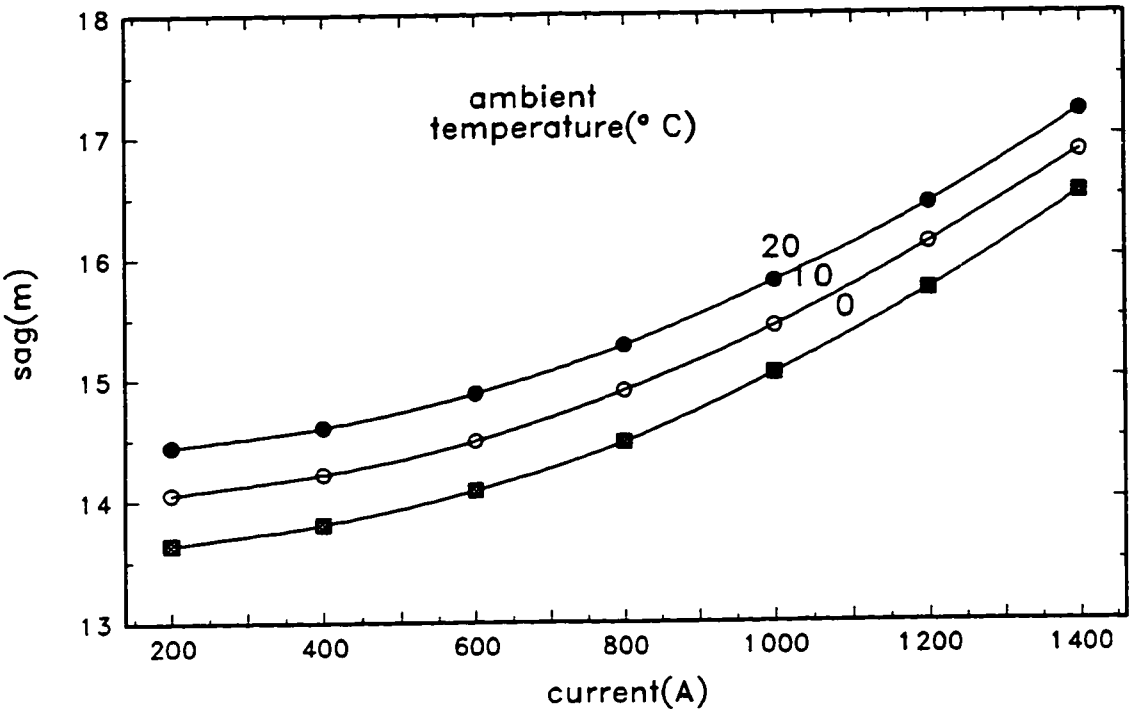

Figure 35 Variation of the sag of the conductor with current and ambient temperature.

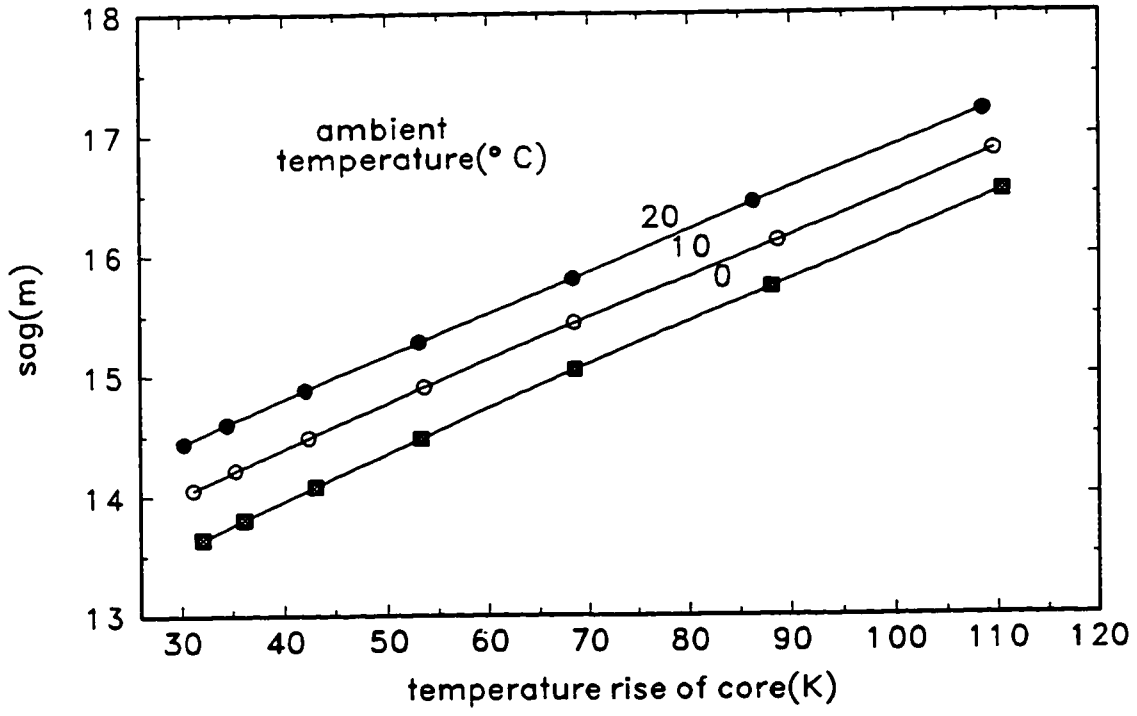

Figure 36 Variation of the sag of the conductor with the temperature rise of the core and ambient temperature.

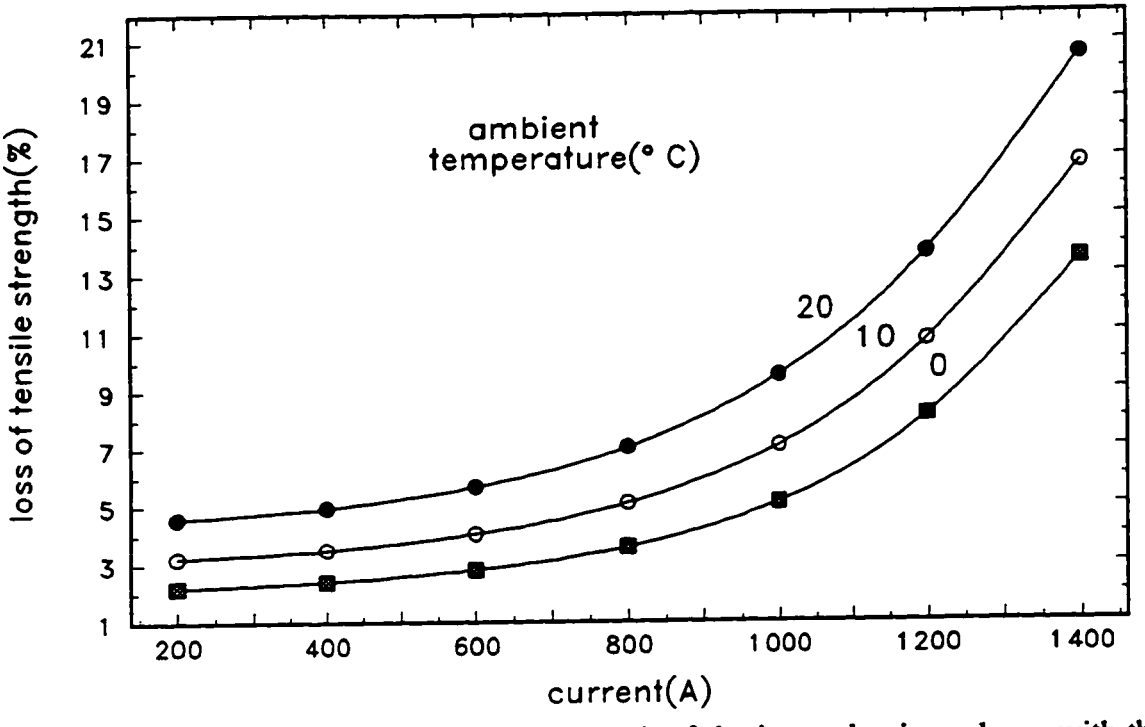

Figure 37 Variation of the loss of tensile strength of the inner aluminum layer with the current and ambient temperature.

4.2 TIME OF EXPOSURE

We use a probabilistic model to explore the effect of exposure time of the conductor at an ambient temperature of 20 °C. The total exposure time is taken at 0.1, 1, 3, 10, and 30 years. The total exposure time consists of the period with additional load case, which lasts 1 % of the total exposure time, and the probability based case which lasts 99 % of the total exposure time. For the times of exposure less than 6.3 years, during a few subintervals in the probability based period, temperature differences occur over periods of shorter than 0.5 hour. But this is tolerated without introduction of the Unsteady-State Thermal Model. Those subintervals could be combined with the next larger subinterval if necessary, but the difference in the final results is negligible.

When the exposure time is taken as 0.5 hour, the probability approach is not employed, and the additional load case is not included. The period is too short and those assumptions would be unrealistic. The exposure time of half an hour consists of the case with constant maximum current. It is applied immediately after the running out and stringing period.

Fig. 38 shows that the Joule losses remain almost constant for all the exposure times. The same holds for the ac resistance of the conductor and the magnitude of the layer currents. The variation of the current density in the steel core and aluminum layers with exposure time for a total current of 1000 A is shown in Fig. 39. Notice that layer 2 is maintained at substantially larger current density than layer 3, and both are larger than layer 1. The variation of the ac resistance with the time of exposure is presented in Fig. 40.

The variation of the temperature rise of the king wire and aluminum layers with

the exposure time for the current 1000 A is given in Fig. 41. The temperature rise of the rest of the core falls between the king wire and first aluminum layer. However, it is not shown in order to present the results in an understandable way. While the temperature of the third layer or the surface temperature remains almost constant for the whole exposure time, the temperature rise of the king wire is larger than the surface temperature rise. The difference increases from 4.9 °C after half an hour, which is 8.1 % of the temperature rise of the surface of the conductor, to 7.8 °C or 12.8 % of the surface temperature rise after 30 years.

The variation of the temperature difference between the king wire and the surface of the conductor with the exposure time and for various currents is shown in Fig. 42. The temperature difference between the king wire and the surface increases with the exposure time. The reason for the discontinuity in the curve for 1200 A, and the smaller slope of the curve for 1400 A is the negative aluminum stress shown in Fig. 43 that occurs at higher levels. The air gap thickness, assumed as $10x\delta$ for the aluminum layers under compression, is obviously too small. Fig. 43 shows that the aluminum stresses for 3, 10, and 30 years and current 1200 A, and for exposure times except 0.5 hour for the current 1400 A are negative, and that compression occurs at these points, hence the variations shown in Fig. 42.

It is seen from Fig. 44 that the steel and aluminum stresses change linearly with increasing (log) time for the time of exposure above 0.1 year. For the current 200 A the steel stress increases by 67 MPa, or 28.2 % in the first year and by 93 MPa, or 39.3 % in 30 years. The aluminum stress decreases by 11.8 MPa, or 45.9 % in the first year of the conductor exposure and by 16.3 MPa, or 63.3 % in 30 years. For 1400 A the

steel stress increases by 63 MPa, or 20.3 % in the first year and by 82 MPa, or 26.5 % in 30 years. The aluminum stress decreases by 13.1 MPa in 30 years, of which the change is 10.0 MPa in the first year of the conductor exposure.

Fig. 45 shows the variation of the horizontal tension of the conductor with the time of exposure and the current. The horizontal tension for the current 200 A decreases by 2.8 kN in thirty years, which is 8.2 % of the horizontal tension after 30 minutes, of which 2.0 kN, or 6.1 % is in the first year. For the current 1400 A, the horizontal tension decreases for 1.6 kN, which is 6.0 % of the horizontal tension after 30 minutes, of which 1.2 kN or 4.4 % occurs in the first year.

Fig. 46 shows how the sag increases as the exposure time increases from 30 minutes to 30 years with a fixed current. It is seen that after 0.1 year, the sag increases linearly with increasing (log) time. After 30 years at the maximum current of 1000 A, the sag increases by 1.11 m (7.5 %) more than its value after 30 minutes exposure. The biggest portion of the sag increase, or 0.8 m occurs in the first year of the conductor exposure.

The variation of the loss of tensile strength of the inner aluminum layer due to annealing with the current and time of exposure is shown in Fig. 47. As the annealing is cumulative, the loss of tensile strength of the aluminum increases with increasing time of exposure and current. For 1000 A the total loss of tensile strength of the inner layer is 9.5 % after 10 years, and 13 % after thirty years.

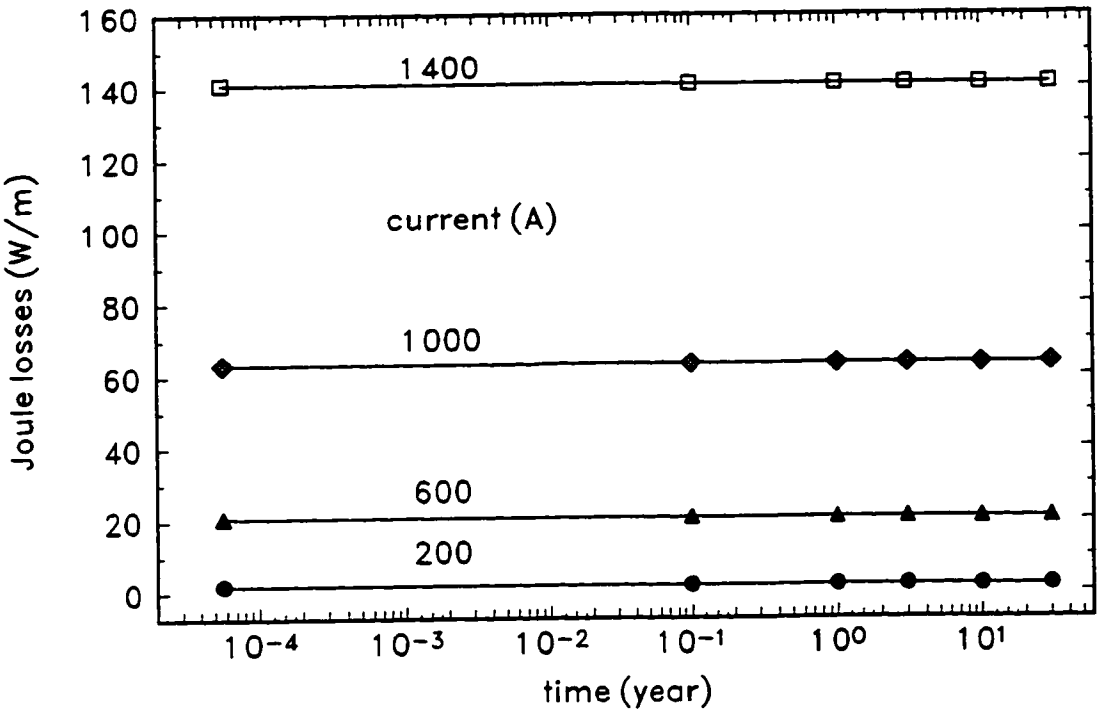

Figure 38 Variation of the Joule losses with the time of exposure and current.

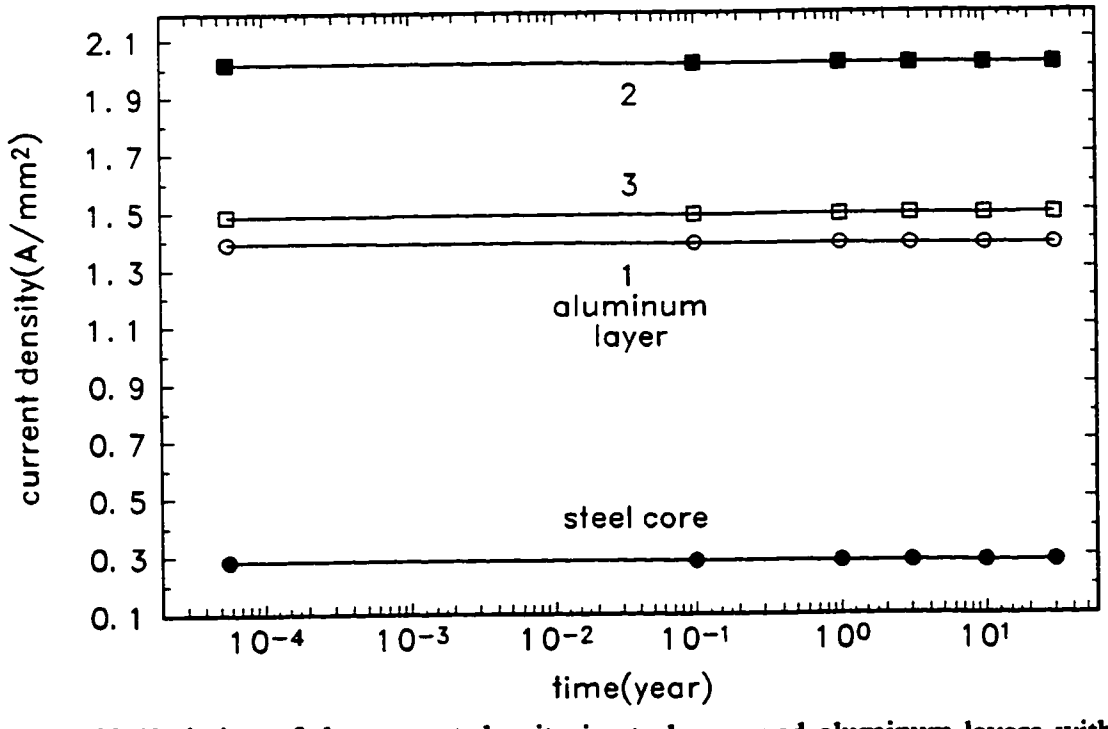

Figure 39 Variation of the current density in steel core and aluminum layers with the time of exposure for 1000 A.

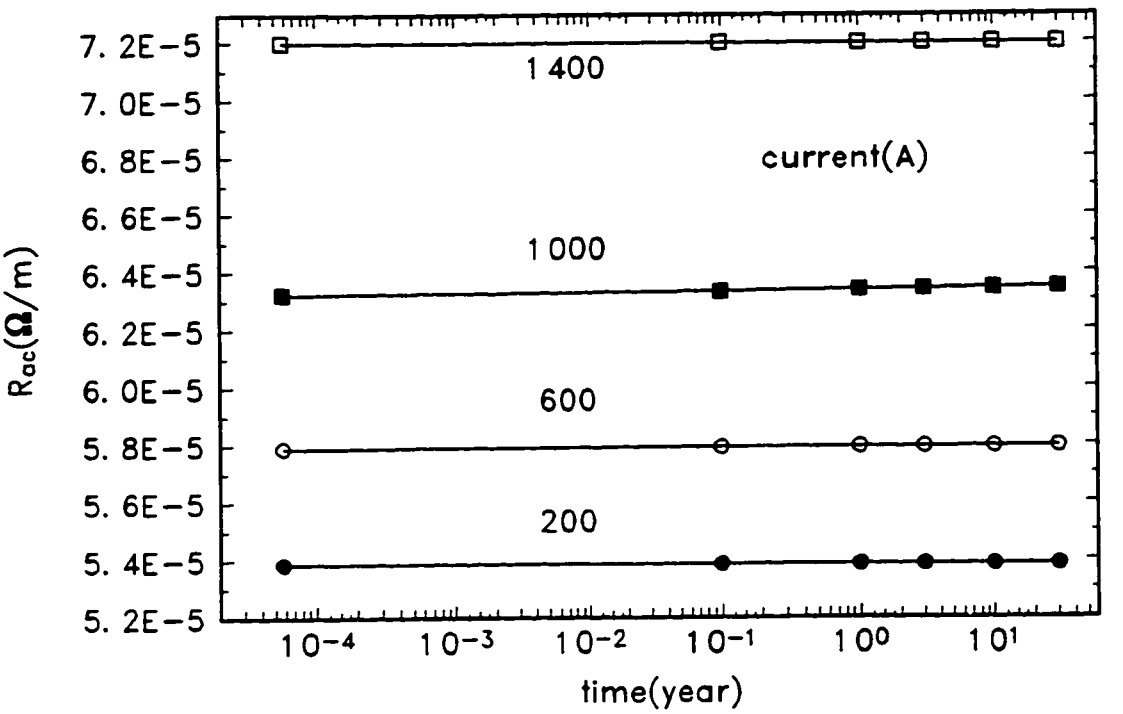

Figure 40 Variation of the ac resistance of the conductor with the time of exposure and the current.

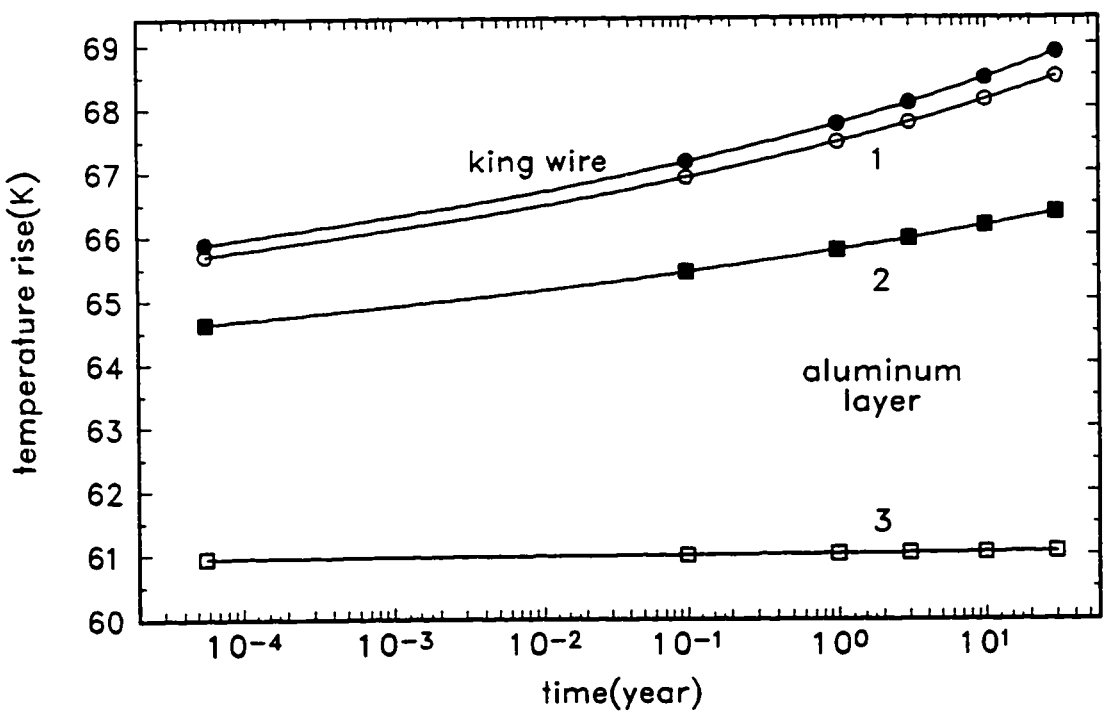

Figure 41 Variation of the temperature rise of the king wire and aluminum layers with the time of exposure for 1000 A.

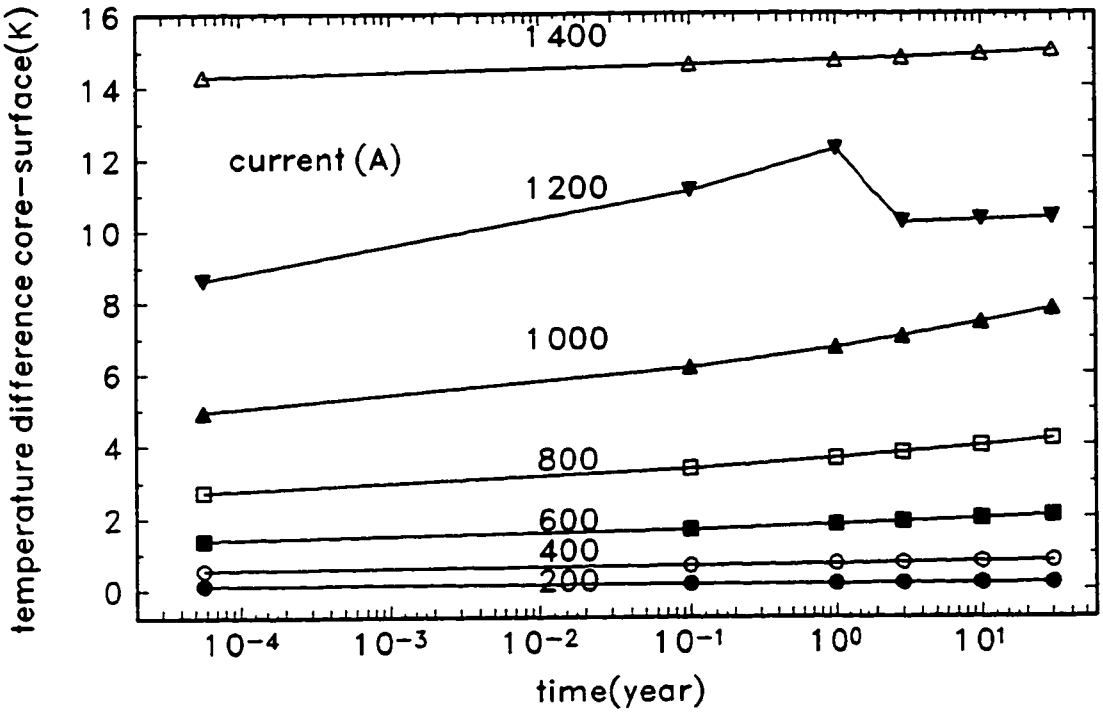

Figure 42 Variation of the difference of the temperature between the king wire and surface with the time of exposure and current.

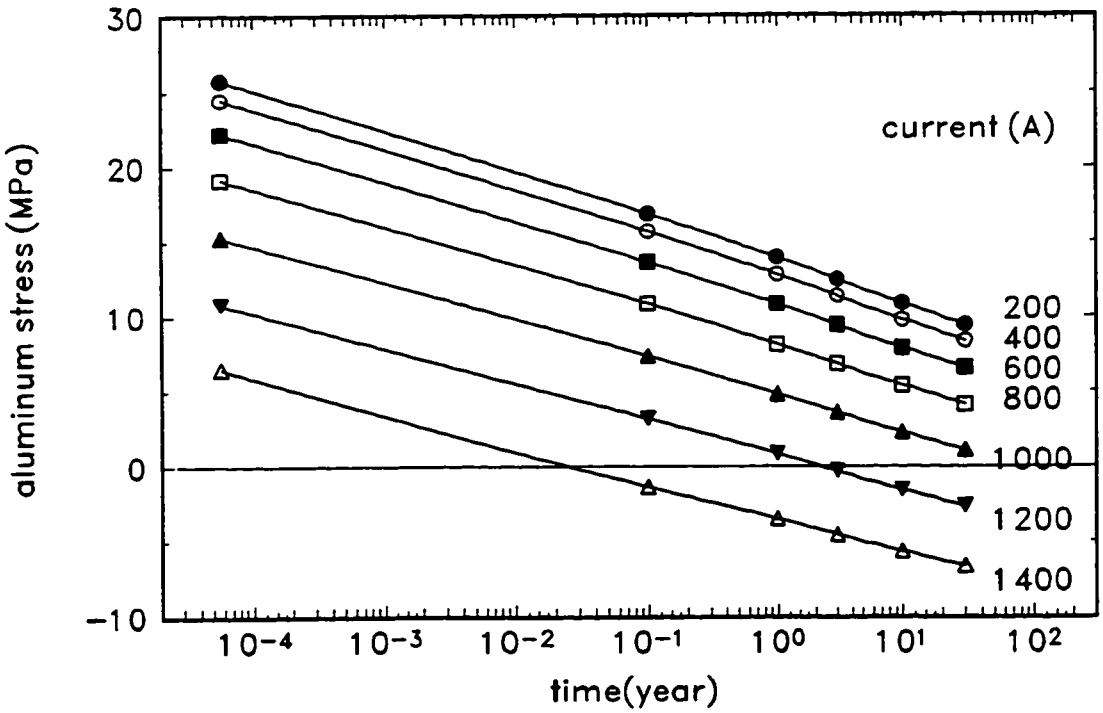

Figure 43 Variation of the aluminum stress with the time of exposure and current.

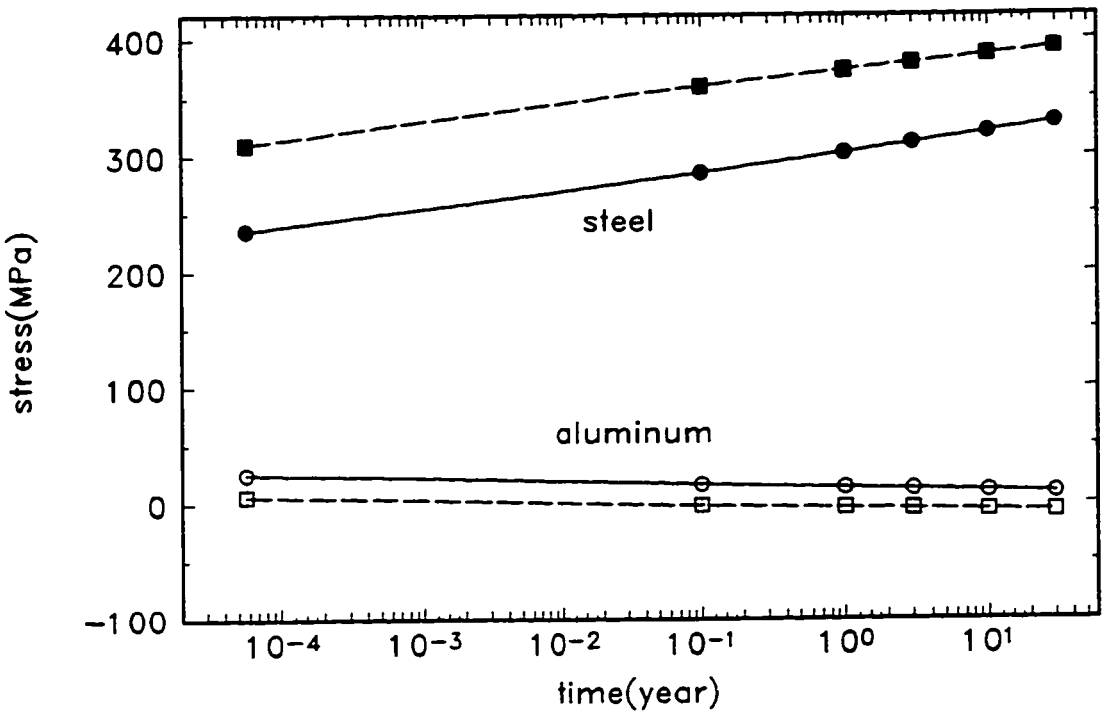

Figure 44 Variation of the steel and aluminum stress with the time of exposure. Current
_____ 200 A _ _ _ 1400 A

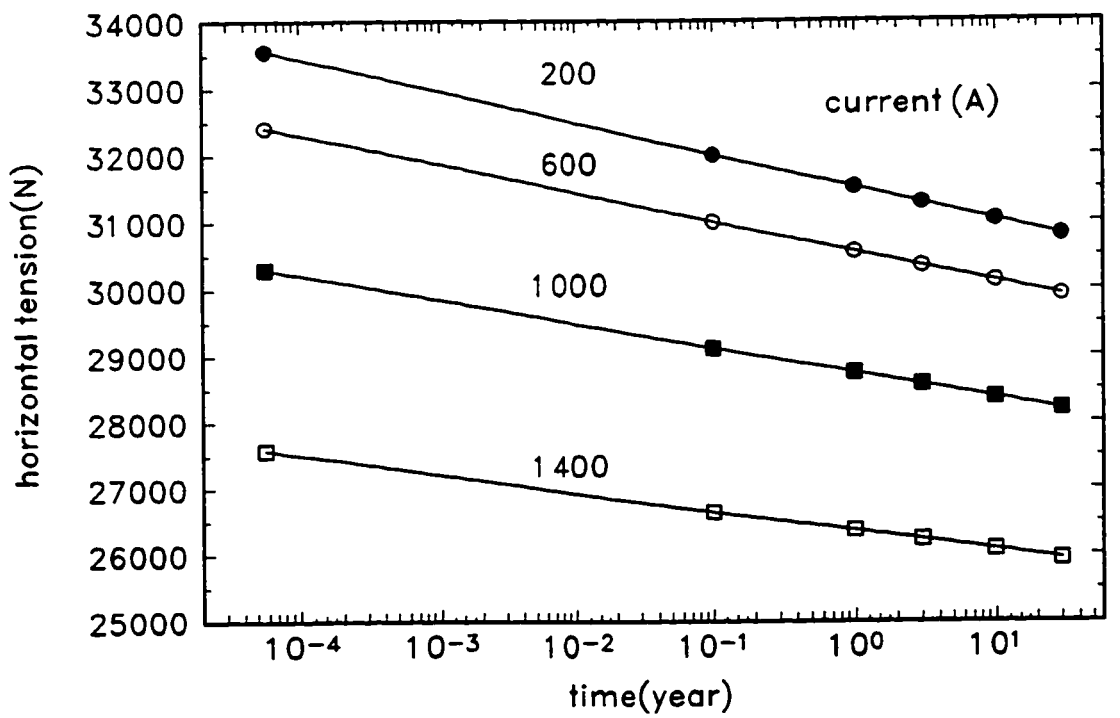

Figure 45 Variation of the horizontal tension of the conductor with the time of exposure and current.

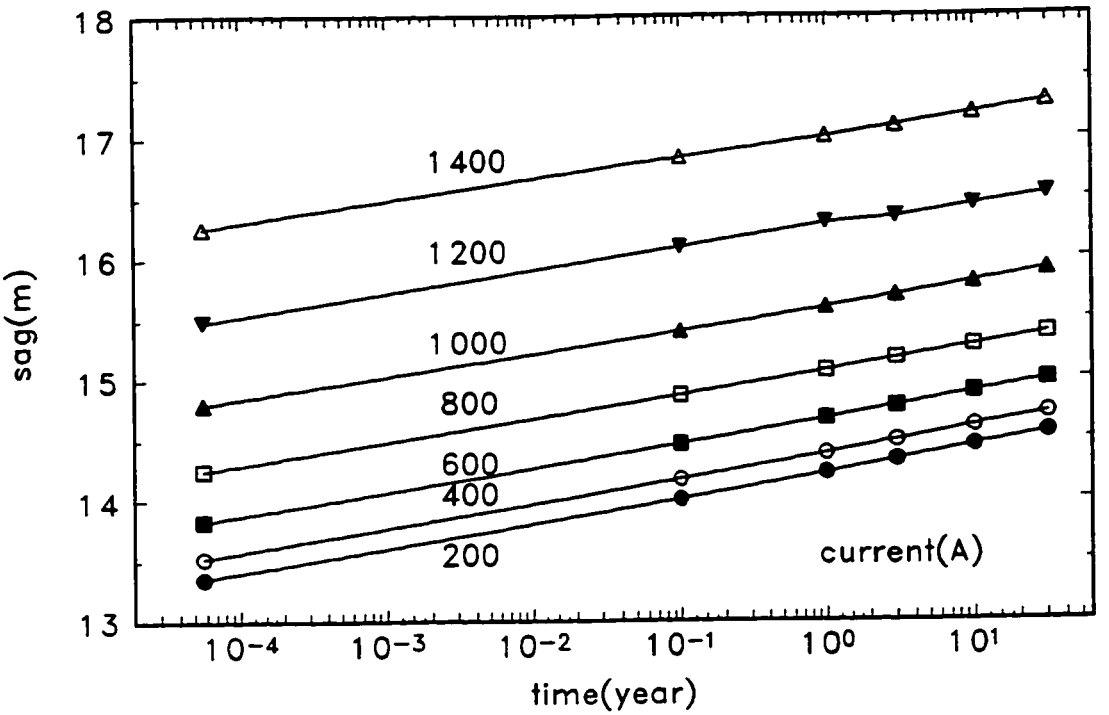

Figure 46 Variation of the sag of the conductor with the time of exposure and the current.

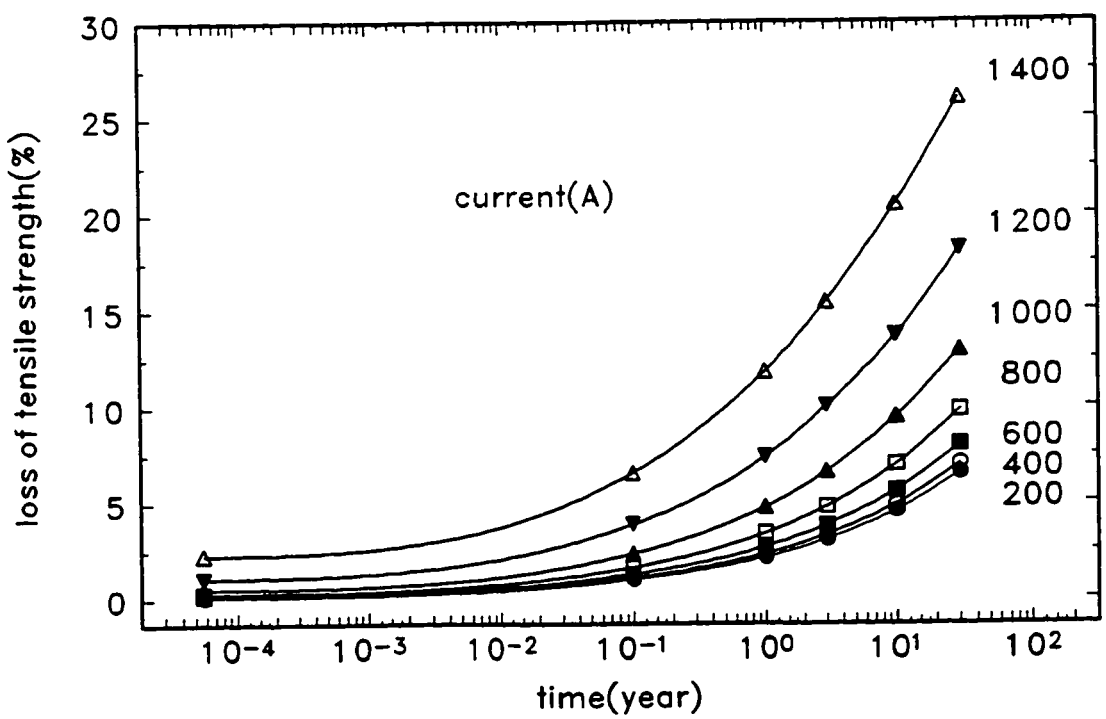

Figure 47 Variation of the loss of tensile strength of the inner aluminum layer with the time of exposure and the current.

4.3 ADDITIONAL LOADS

The effects of the various additional load cases on the characteristics of the conductor are investigated through the variation of the thickness of the ice for the standard time duration of the additional load case and through the change of the time duration of the additional load case for standard ice thickness and wind pressure.

THICKNESS OF THE ICE

Besides the standard ice thickness of 6.35 mm applied as an additional loading, together with the standard value for the wind pressure, the ice thickness is altered from 2 mm to 18 mm, in steps of 2 mm. For an ice thickness of 18 mm and current 1400 A, birdcaging occurs in some of the subintervals of the probability based period and the Unified Model can not be applied.

Fig. 48 shows that the Joule losses remain relatively constant for various ice thicknesses for a fixed current. The ac resistance of the conductor and the magnitude of the layer currents are also constant.

It is seen from Fig. 49 that the surface temperature rise remains constant for all ice thicknesses, while the temperature rise of the king wire and inner aluminum layers increases with an increase of ice thickness, as the aluminum stress decreases. For 1000 A the temperature rise of the king wire is larger than that of the surface from 7.3 °C, or 12.0 % at ice thickness 2 mm, to 8.0 °C or 13.1 % of the surface temperature rise for an ice thickness of 18 mm.

Fig. 50 presents the variation of the temperature difference between the king wire and the surface of the conductor. For currents of 200, 600, and 1000 A, for which the

aluminum stress does not fall bellow zero and the aluminum part of the conductor is not under compression, the temperature difference between the king wire and the surface increases nonlinearly with increasing ice thickness. For a current of 1400 A, where for all ice thicknesses the aluminum is under compression, Fig. 51, the temperature difference between the king wire and surface decreases from 15.2 , or 16.3 % of the temperature rise of the surface for an ice thickness 2 mm, to 14.1 °C, or 15.0 % of the surface temperature rise for 16 mm ice thickness. This is in consequence of the assumption introduced in the Radial Conduction Model, that the metal to metal contact area, when the aluminum layers are under compression, is calculated from the maximum aluminum stress during the conductor lifetime. As the maximum stress increases with ice thickness, the temperature difference between king wire and surface increases.

The change in steel and aluminum stresses with ice thickness for fixed currents is shown in Fig. 52. The aluminum stress, which is also presented in Fig. 51 decreases with increasing ice thickness as the creep and especially settling strains increase with the increasing additional load. Aluminum transfers more stress to the steel portion of the conductor for the bigger ice thickness increasing the steel stress.

The horizontal tension of the conductor decreases with increasing ice thickness, as shown in Fig. 53, as the permanent elongation of the conductor increases with increasing ice thickness.

Fig. 54 shows how the sag of the conductor changes with ice thickness for a fixed current. It is seen that the sag increases by only 0.8 % at 1000 A and by 0.4 % at 1400 A under assumed ice thickness of 16 mm. The sag for the current 1400 A increases at a smaller rate because the temperature difference between the king wire and the surface

decreases with increasing ice thickness, due to the assumption that the metal to metal contacts can be calculated from the maximum stress in the aluminum part of the conductor during the lifetime.

Fig. 55 shows that while the loss of tensile strength of the inner aluminum layer due to annealing remains almost constant for currents 200, 600, and 1000 A for which aluminum is under tension, for 1400 A, when aluminum is under compression, the loss of tensile strength of the inner layer decreases with an increase of the ice thickness.

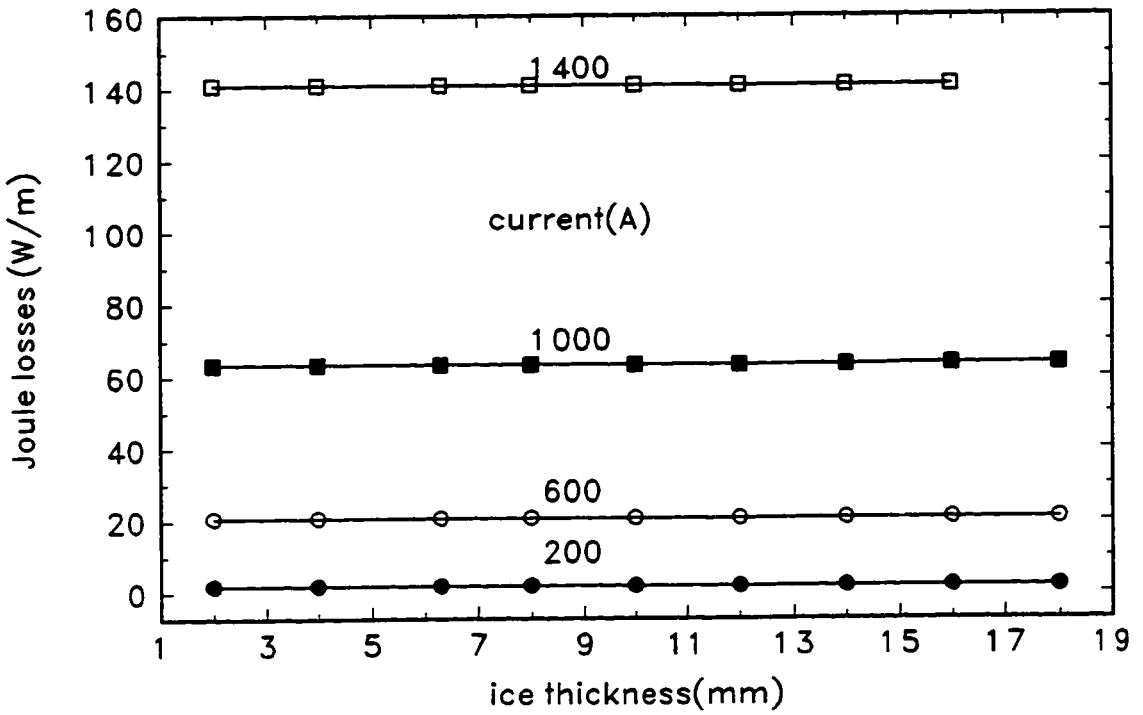

Figure 48 Variation of the Joule losses with the ice thickness and current.

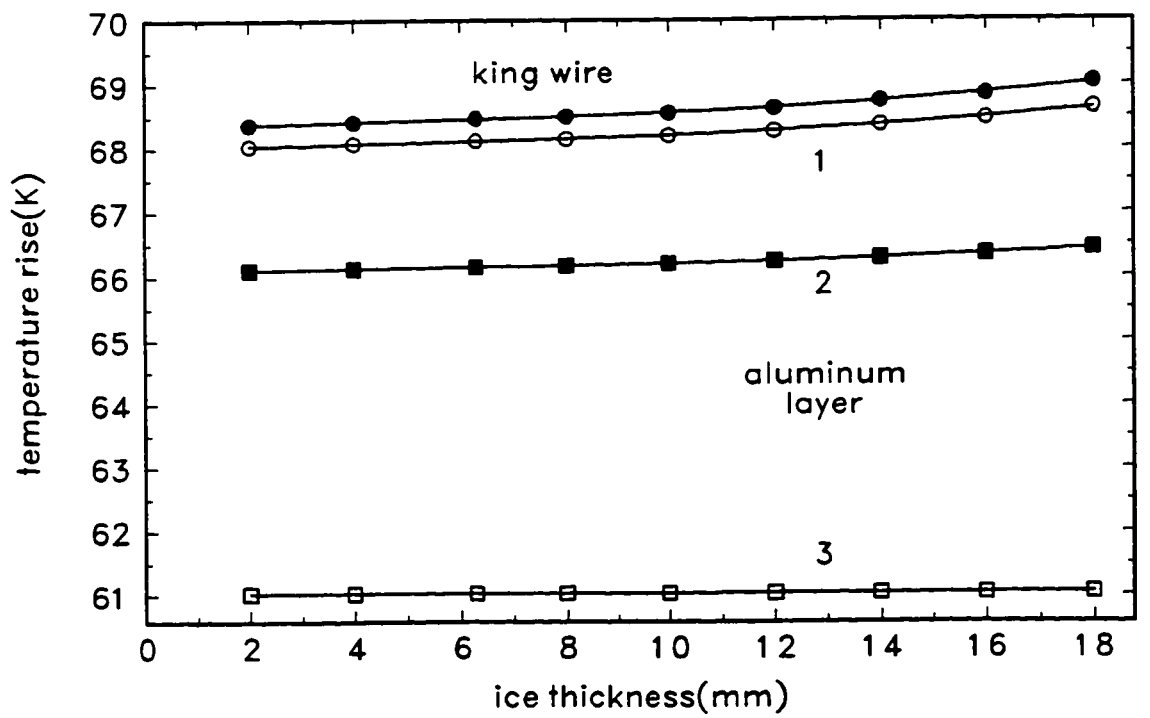

Figure 49 Variation of the temperature rise of the king wire and aluminum layers with the ice thickness for 1000 A.

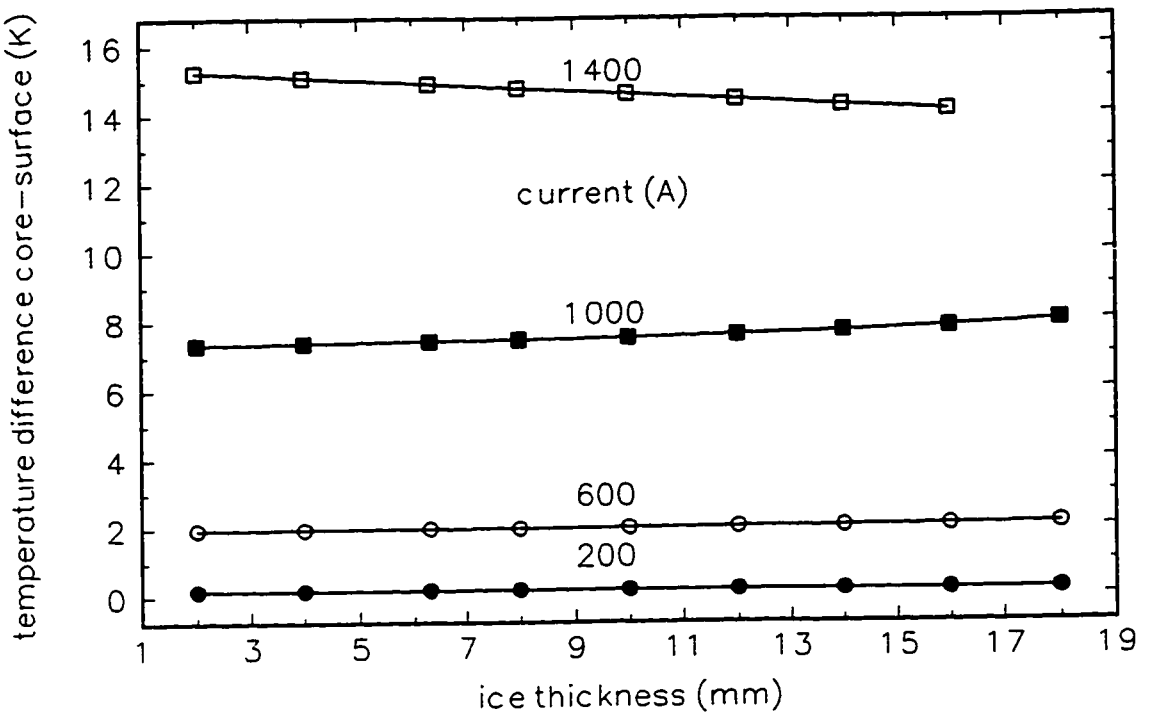

Figure 50 Variation of the temperature difference between king wire and surface with ice thickness and current.

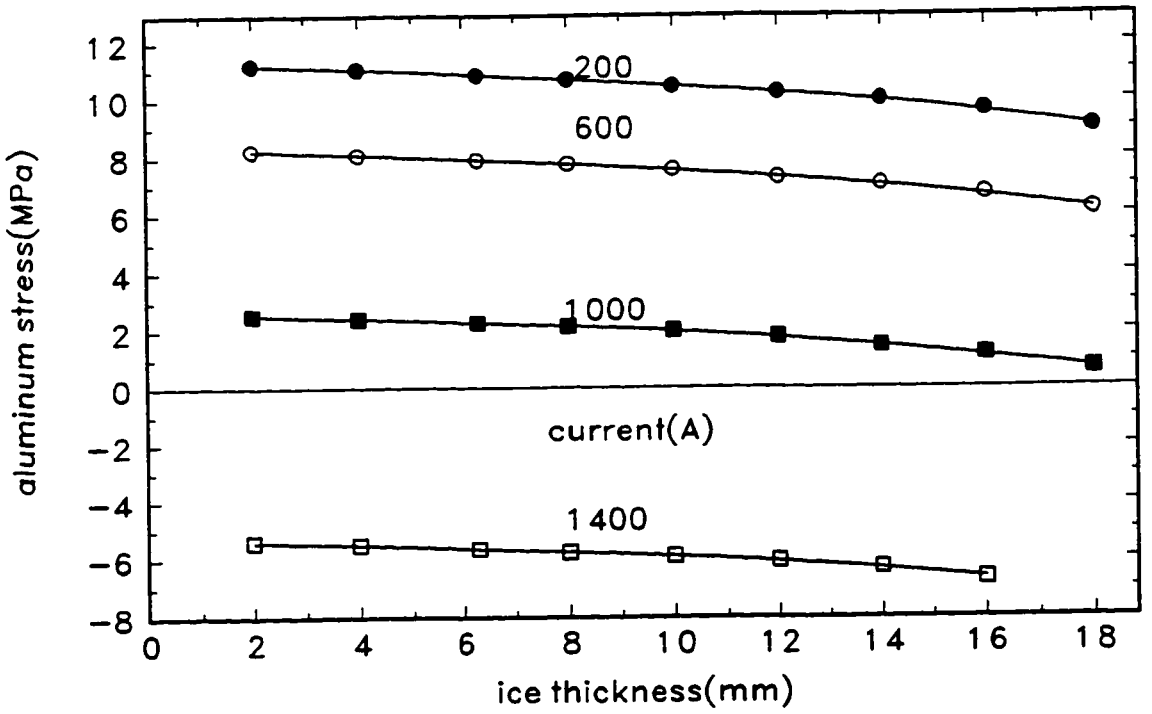

Figure 51 Variation of the aluminum stress with the ice thickness and current.

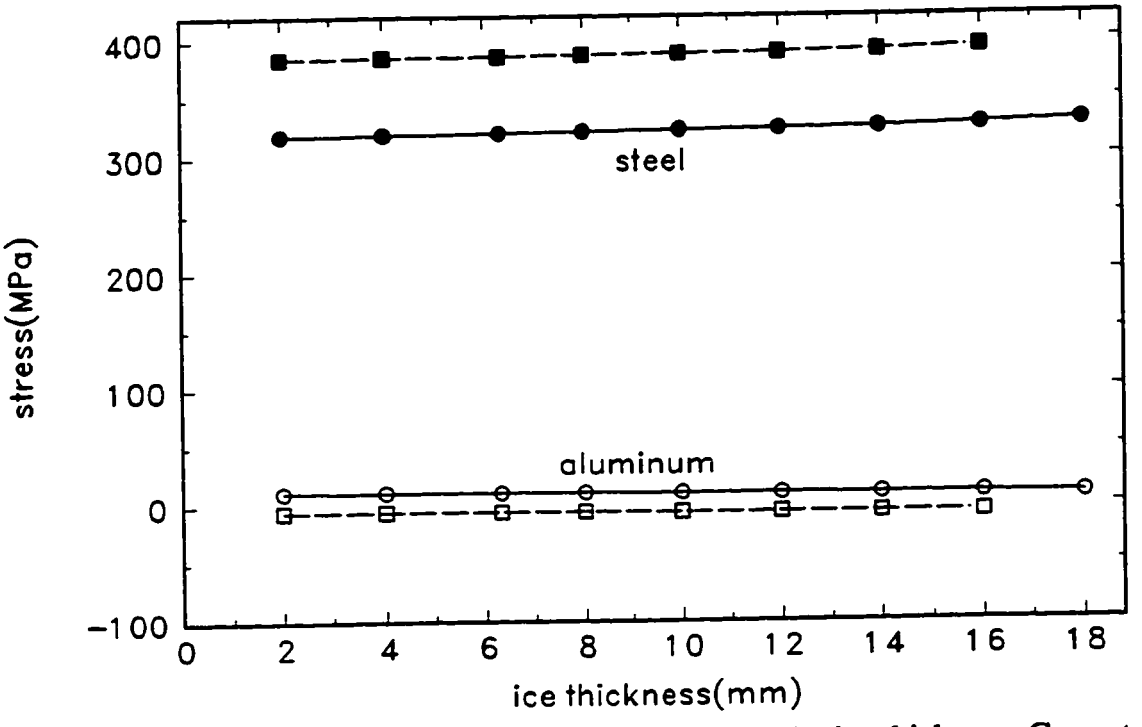

Figure 52 Variation of the steel and aluminum stress with the ice thickness. Current
_____ 200 A _ _ _ 1400 A

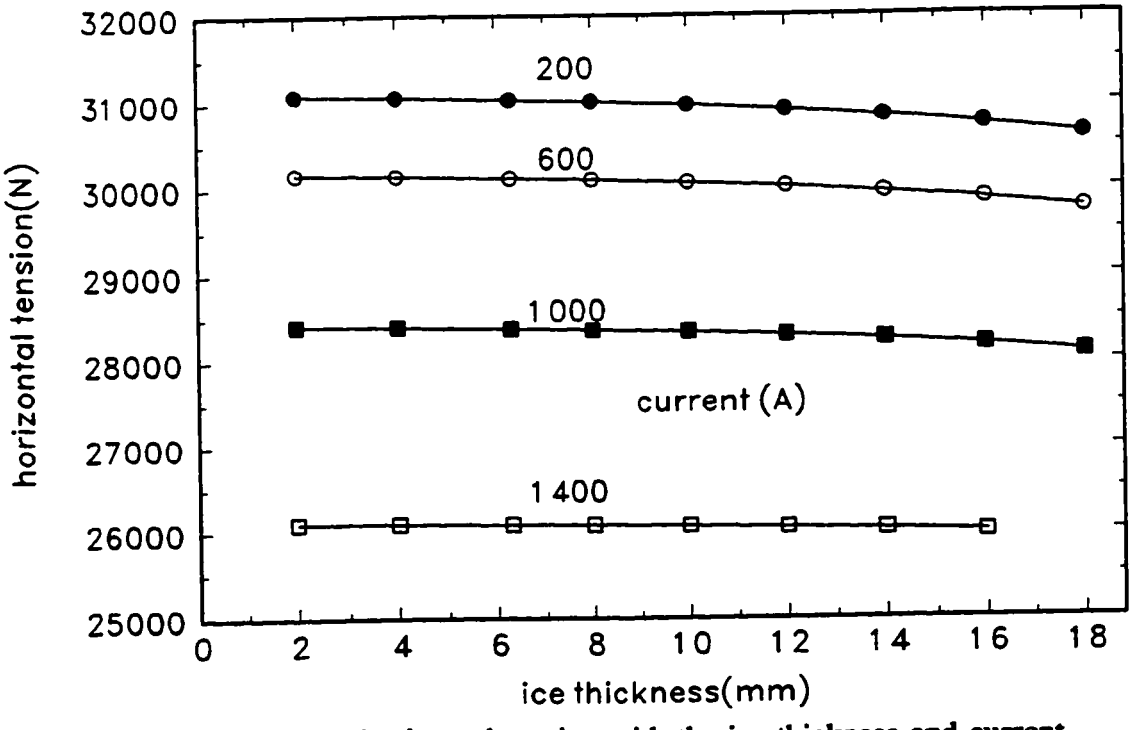

Figure 53 Variation of the horizontal tension with the ice thickness and current.

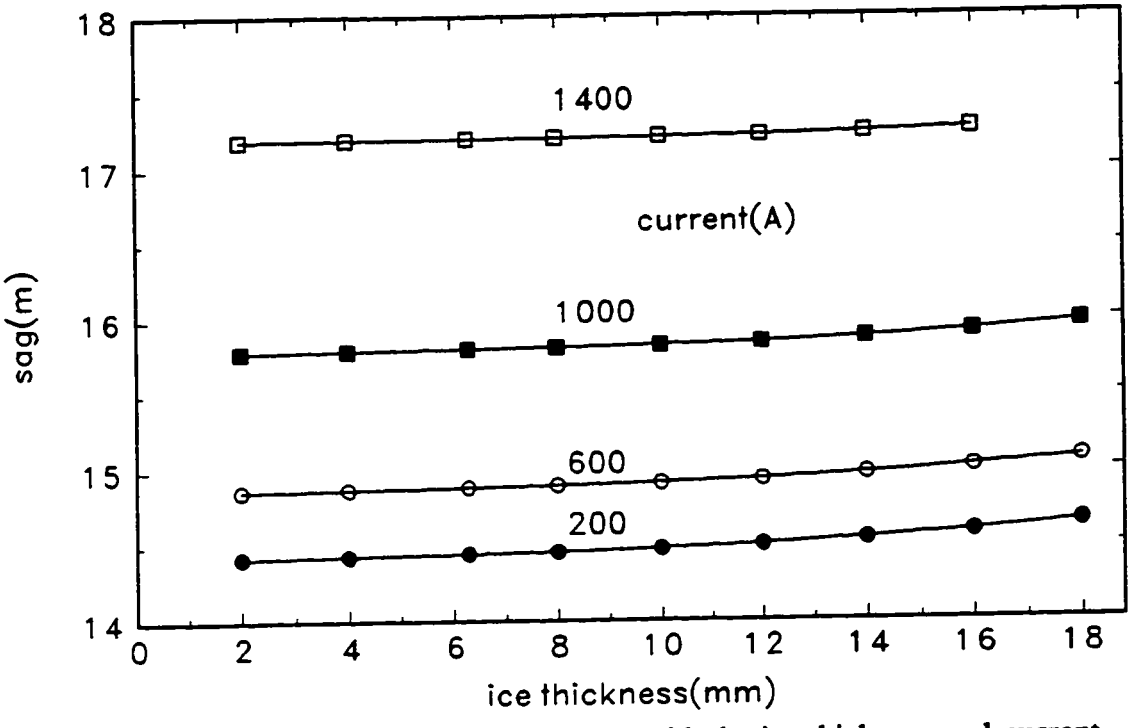

Figure 54 Variation of the sag of the conductor with the ice thickness and current.

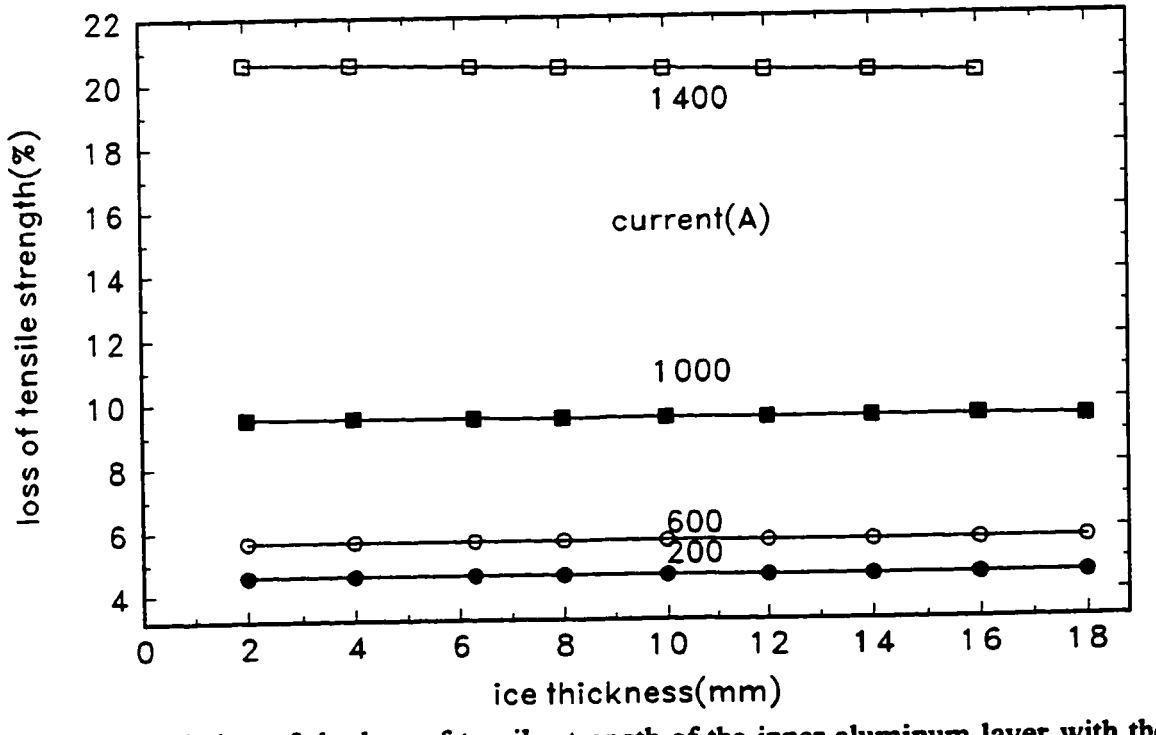

Figure 55 Variation of the loss of tensile strength of the inner aluminum layer with the ice thickness and current.

DURATION OF THE ADDITIONAL LOAD

For this case, the total time of exposure of the conductor is maintained as 10 years, but the proportion of the duration of the additional load case versus the probability based period is varied. The time duration of the additional load case is altered from the standard 1 % to 13 % of the total exposure time.

The Joule losses, ac resistance of the conductor, and magnitude of the layer currents remain constant with the variation of the duration of the additional load case.

Fig. 56 shows that the temperature rise of the king wire and aluminum layers remain almost constant for all durations of the additional load for 1000 A.

Note also that the difference between the king wire temperature and surface temperature changes little with duration of the additional load and the current, for the currents 200, 600, and 1000 A, as seen from Fig. 57. For 1400 A the temperature difference increases with increasing duration of the additional load, but that increase is caused only by the fact that the maximum stress in the aluminum for the calculation of the radial temperature differences is taken at the end of the additional load case period. Had the maximum aluminum stress been taken at the beginning of the additional load period, it would have been the same for all additional load case durations and the temperature rise would have been constant for 1400 A as well.

Fig. 58 shows that the steel and aluminum stresses remain constant for all durations of the additional load case. It can be seen from Fig. 59 that the horizontal tension is almost constant too, and from Fig. 60 that the sag remains the same for all durations of the additional loading period.

The variation of the loss of tensile strength of the inner aluminum layer with the

duration of the additional load case is shown in Fig. 61. As the duration of the probability based period decreases when the duration of the additional load case period increases, the duration of high temperatures, and consequently, the loss of tensile strength decreases. For 1400 A the loss of tensile strength decreases from 20.5 % to 20.0 %, when the duration of the additional load case increases from 1 % to 13 % of the total exposure time.

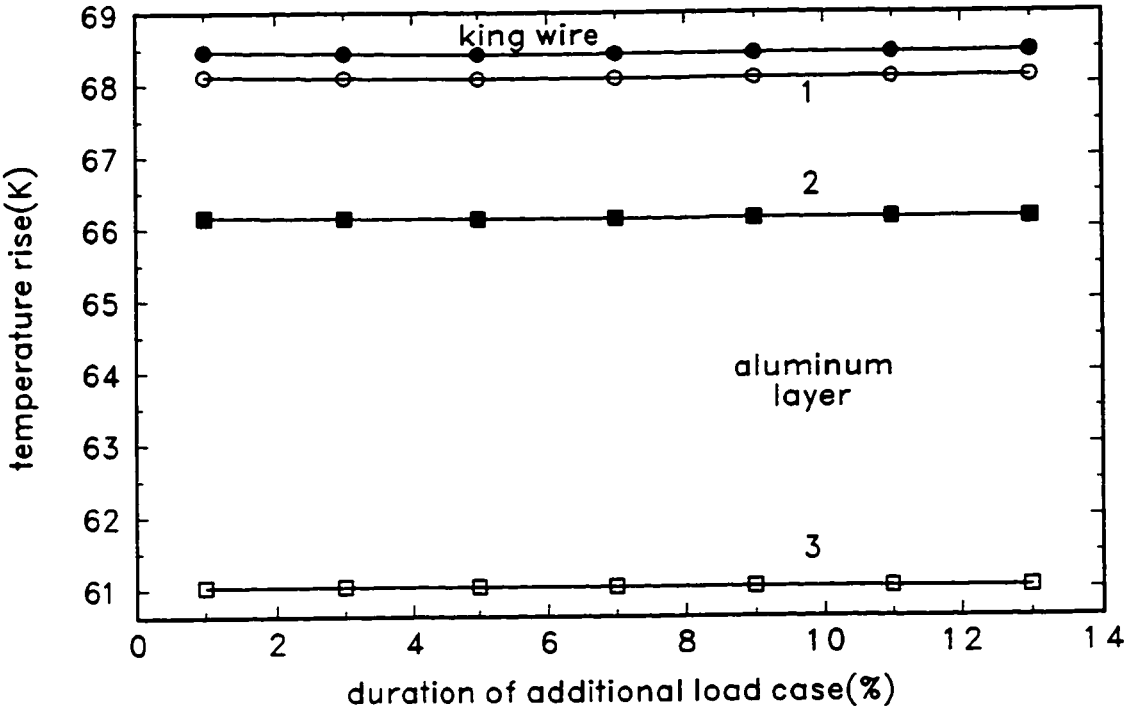

Figure 56 Variation of the temperature rise of the king wire and aluminum layers with the duration of the additional load case period for the current 1000 A.

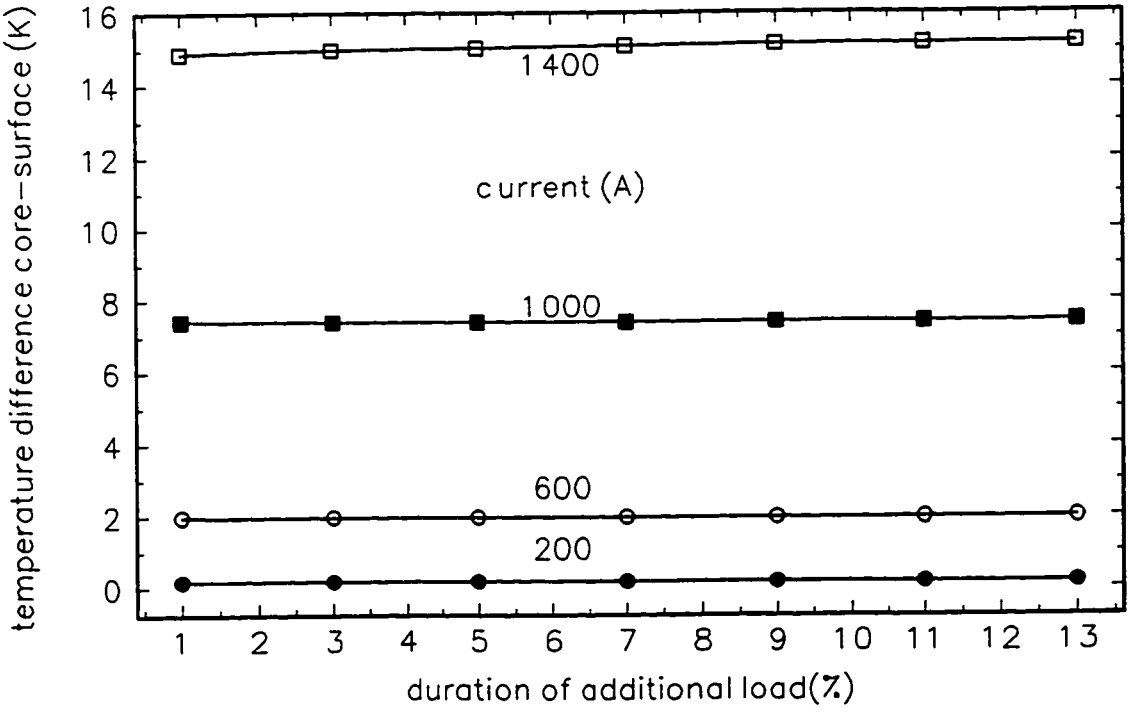

Figure 57 Variation of the temperature difference between the king wire and surface of the conductor with the duration of the additional load case period and current.

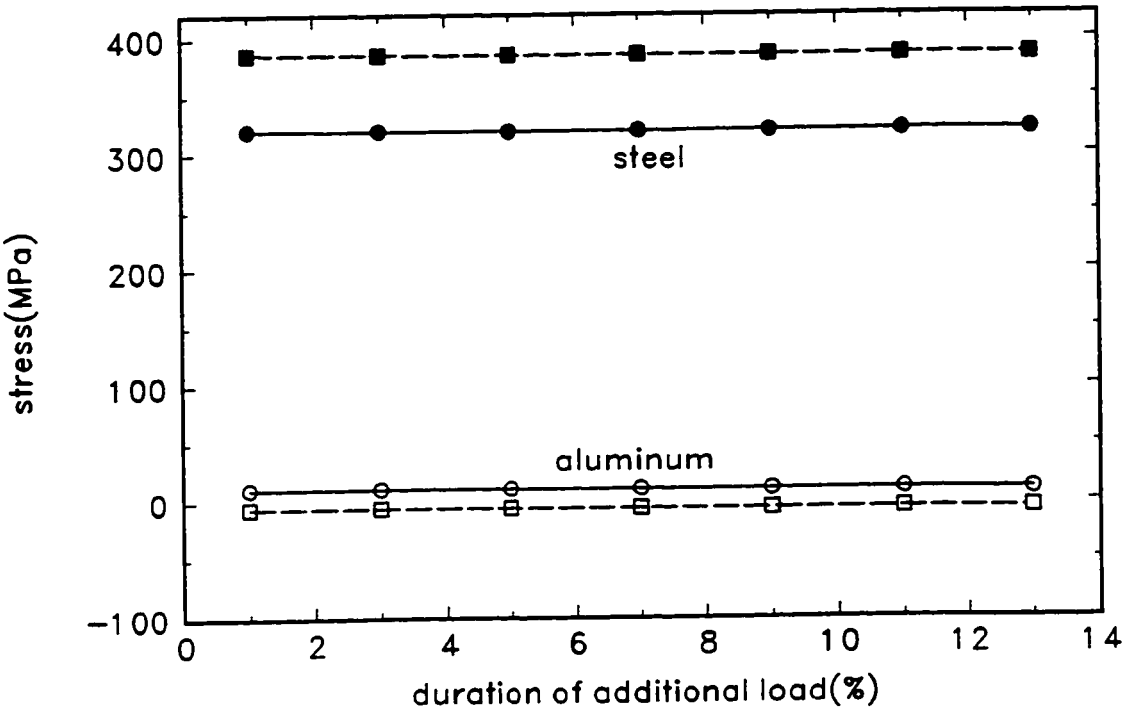

Figure 58 Variation of the steel and aluminum stresses with the duration of the additional load case period. Current
_____ 200 A _ _ _ 1400 A

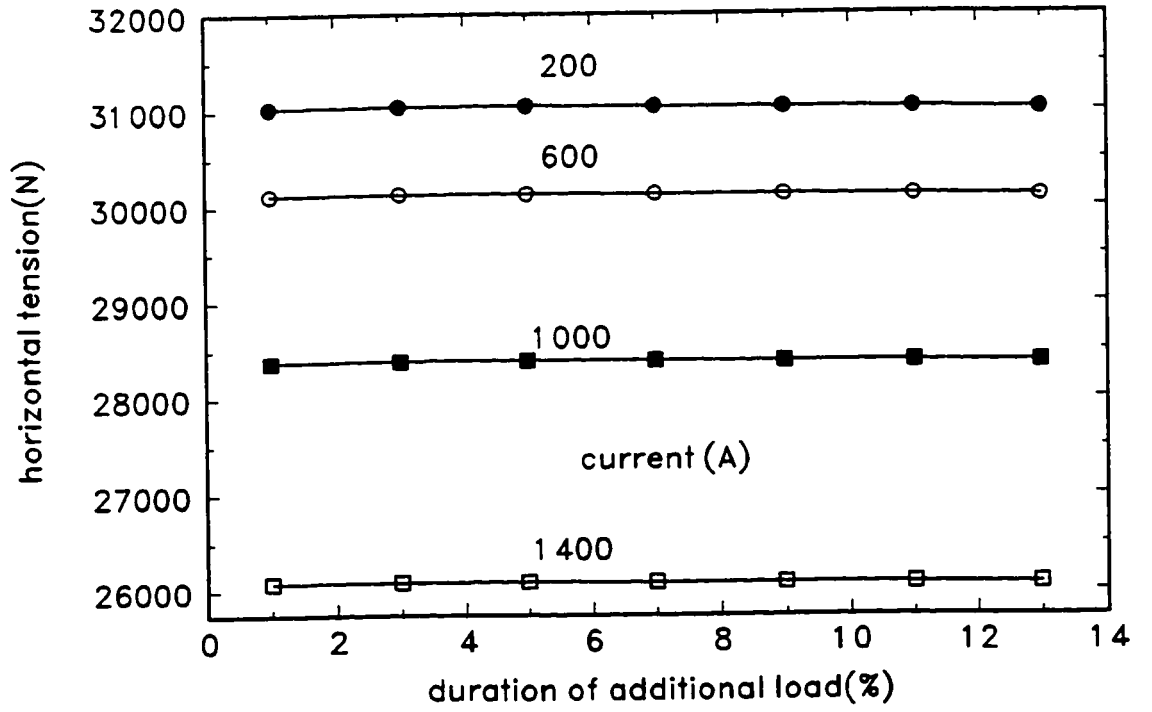

Figure 59 Variation of the horizontal tension of the conductor with the duration of the additional case period and current.

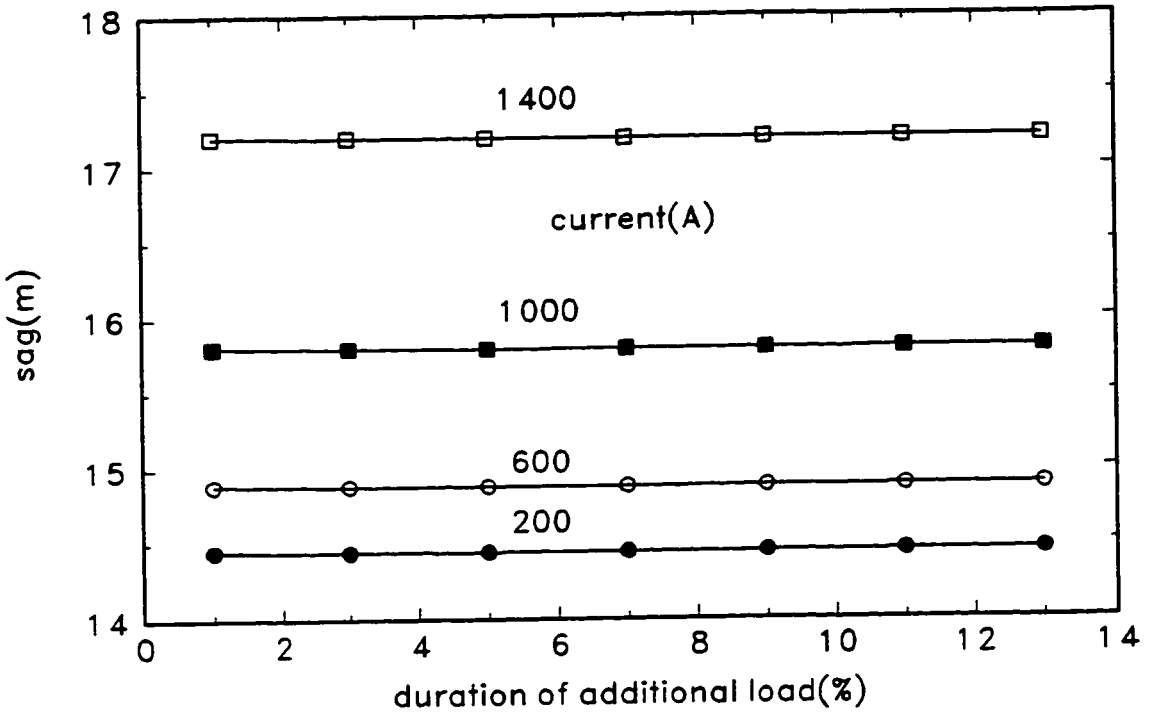

Figure 60 Variation of the sag of the conductor with the duration of the additional load case period and current.

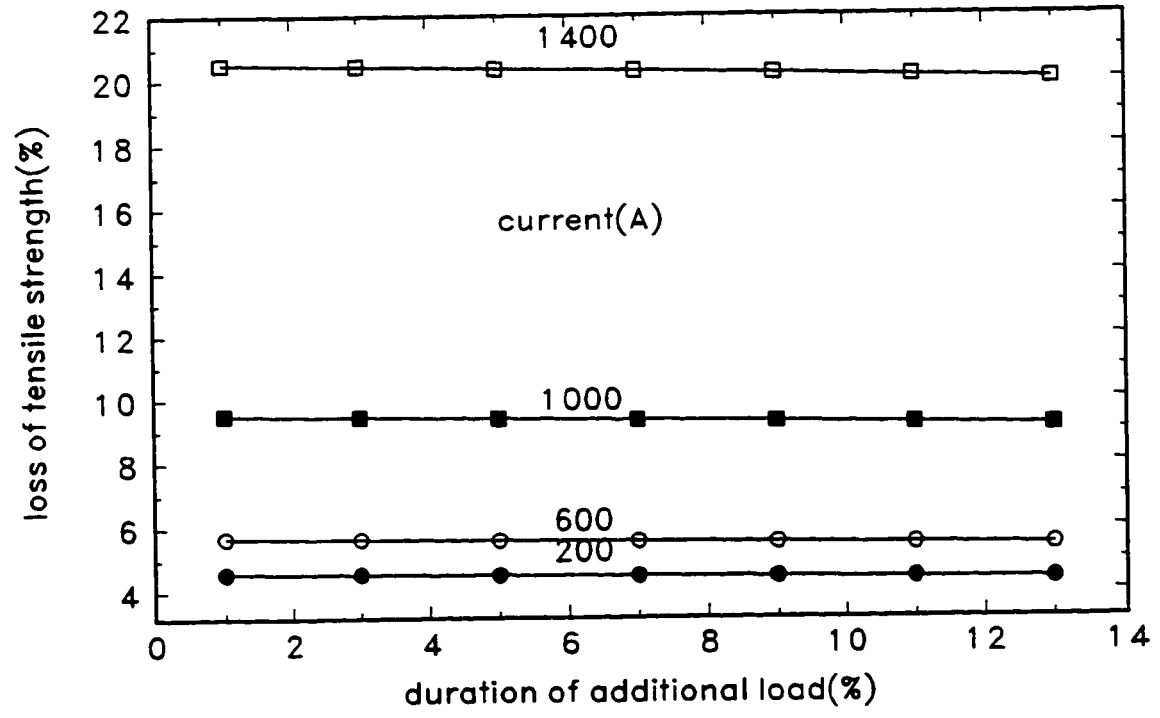

Figure 61 Variation of the loss of tensile strength of the inner aluminum layer with the duration of the additional load case period and current.

4.4 AIR GAP THICKNESS

The thickness of the air gap is changed from 0.2 μm to 1.4 μm in steps of 0.2 μm. When the aluminum is under compression, before birdcaging occurs, it is always assumed that the air gap thickness is ten times that which is taken when the aluminum is under tension and the radial forces on the layers can be obtained.

The electrical characteristics of the conductor remain almost constant with the variation of the air gap thickness for currents of 200 A, 600 A, and 1000 A. The Joule losses and current density in the inner, middle, and outer aluminum layers change by less than 0.3 % at 1000 A. For 1400 A, the Joule losses increase by 0.2 %, when the air gap increases from 0.2 μm to 1.4 μm. The variation of current density in layers with the air gap thickness for the current 1400 A is shown in Fig. 62. The current density in the middle aluminum layer decreases by 2.3 %, and in the outer layer increases by 2.0 % when the air gap increases from 0.2 μm to 1.4 μm. The current redistribution in layers changes for 1400 A because of the bigger temperature differences between the layers.

Fig. 63 shows the variation of the temperature rise of the king wire and aluminum layers with air gap thickness for 1000 A. The temperature rise of the king wire increases from 66.3 °C at 0.2 μm to 68.7 °C at 1.4 μm, which is 3.5 % of the temperature rise at the air gap thickness 0.2 μm.

It can be seen from Fig. 64 how the temperature difference between the king wire and surface of the conductor changes with air gap thickness and current. For 1400 A the temperature difference increases from 8.7 °C to 15.8 °C when the air gap increases from 0.2 μm to 1.4 μm, which is an increase in radial temperature difference of 80.7 %.

Fig. 65 presents the variation of the steel and aluminum stresses with air gap thickness and current. While the aluminum stress is constant for all air gap thicknesses and for all currents, the steel stresses decrease with air gap thickness, the decrease being bigger for the higher current. For 1400 A, the steel stress decreases from 389.6 MPa to 386.3 MPa when the air gap increases from 0.2 μm to 1.4 μm.

The variation of the horizontal tension of the conductor with air gap thickness and current is given in Fig. 66. For 1400 A the horizontal tension decreases from about 26.3 kN to about 26.0 kN, or only 0.8 %.

Fig. 67 shows the variation of the sag of the conductor with the air gap thickness and current. The sag increases by 15 cm for the current 1400 A, and 5 cm for 1000 A when the air gap increases from 0.2 μm to 1.4 μm.

The variation of the loss of tensile strength of the inner aluminum layer with the air gap and current is shown in Fig. 68. While the loss of tensile strength of the outer aluminum layer is almost constant, the loss of tensile strength of the inner aluminum layer increases from 18.5 % for the air gap of 0.2 μm to 20.8 % for the 1.4 μm air gap.

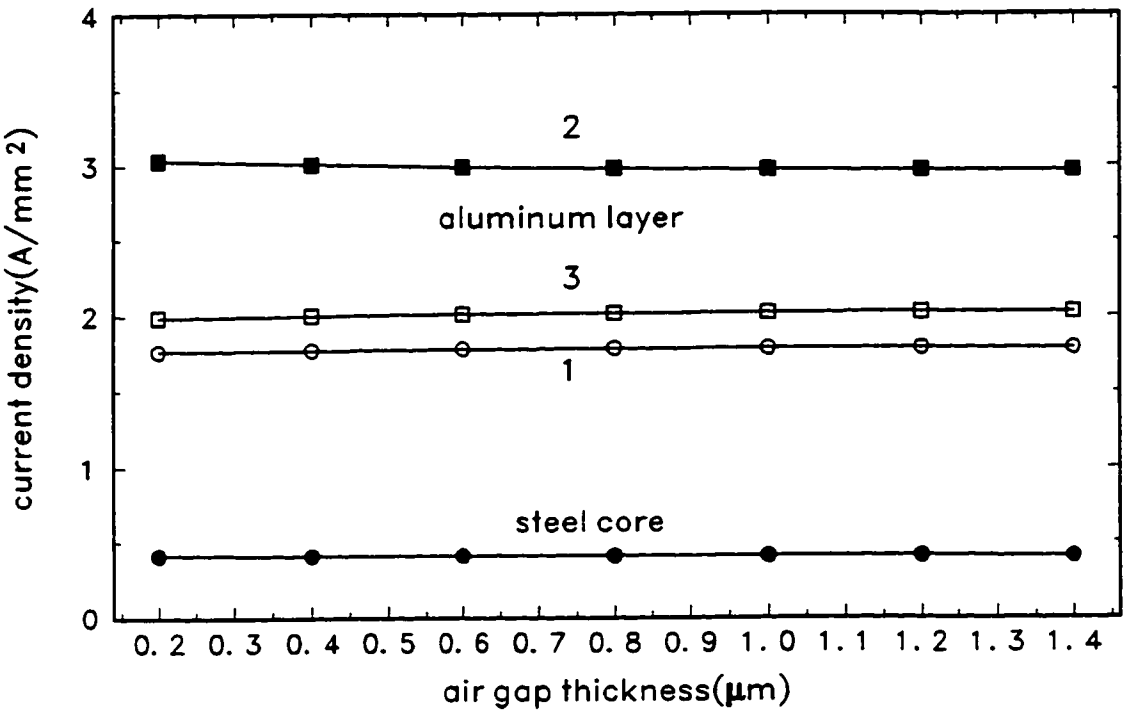

Figure 62 Variation of the current density in steel core and aluminum layers with the air gap thickness for the current 1400 A.

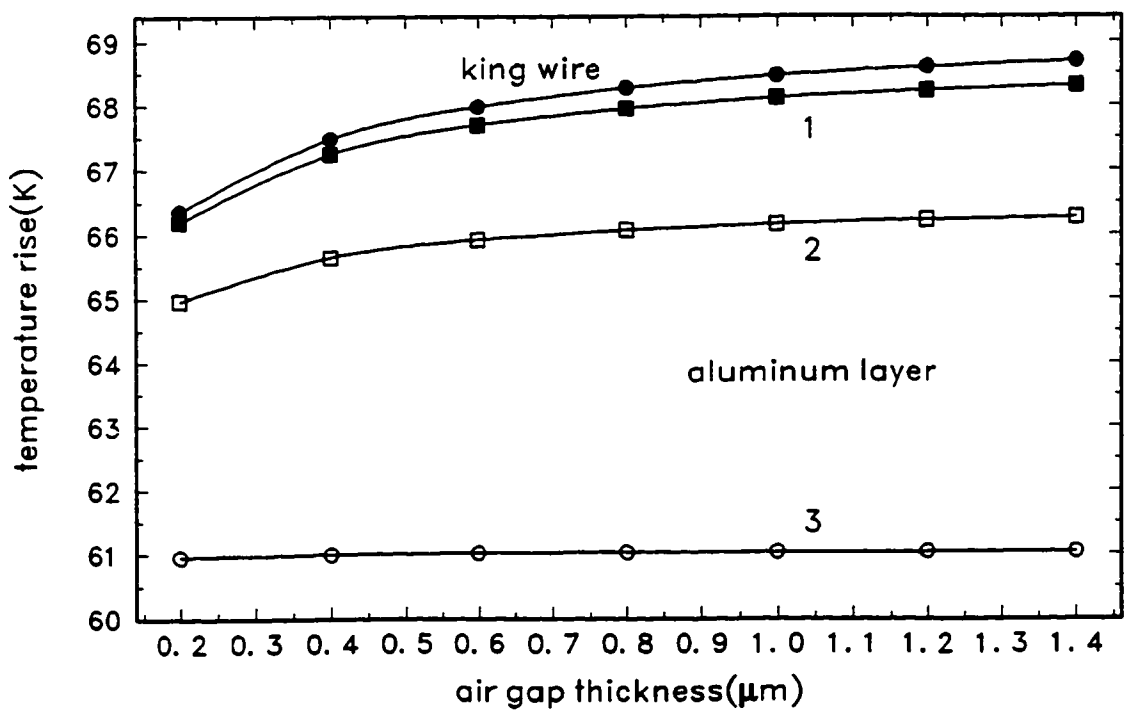

Figure 63 Variation of the temperature rise of the king wire and aluminum layers with the air gap thickness for the current 1000 A.

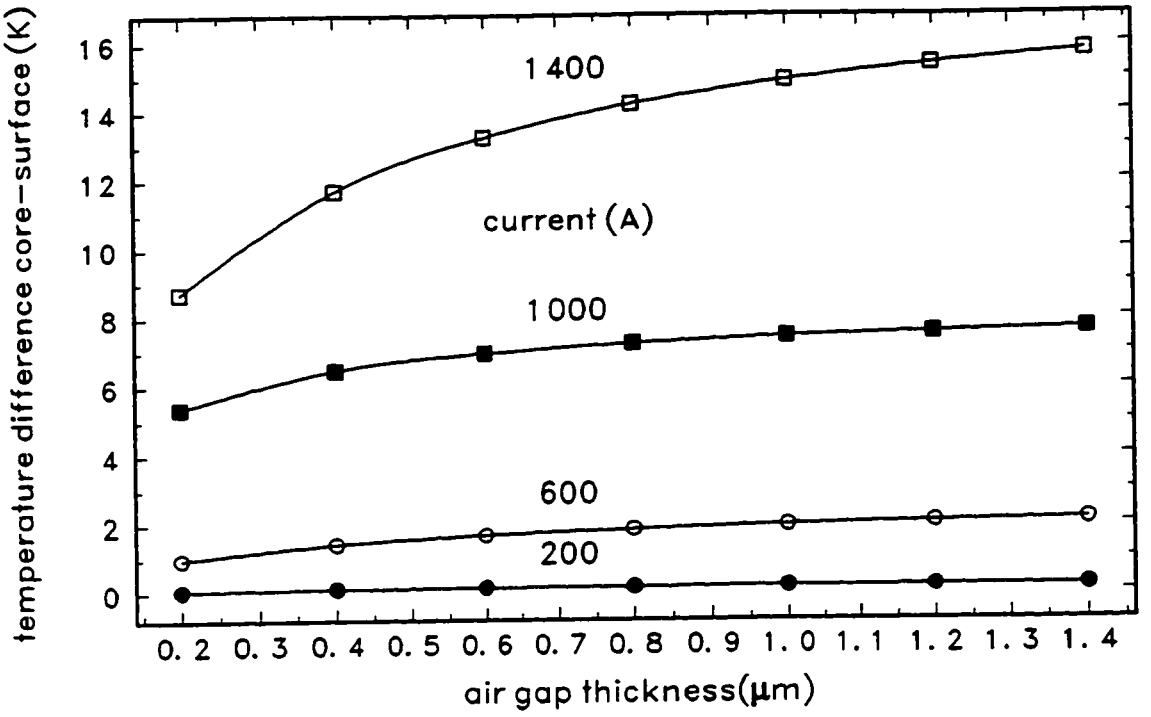

Figure 64 Variation of the temperature difference between the king wire and surface of the conductor with the air gap and current.

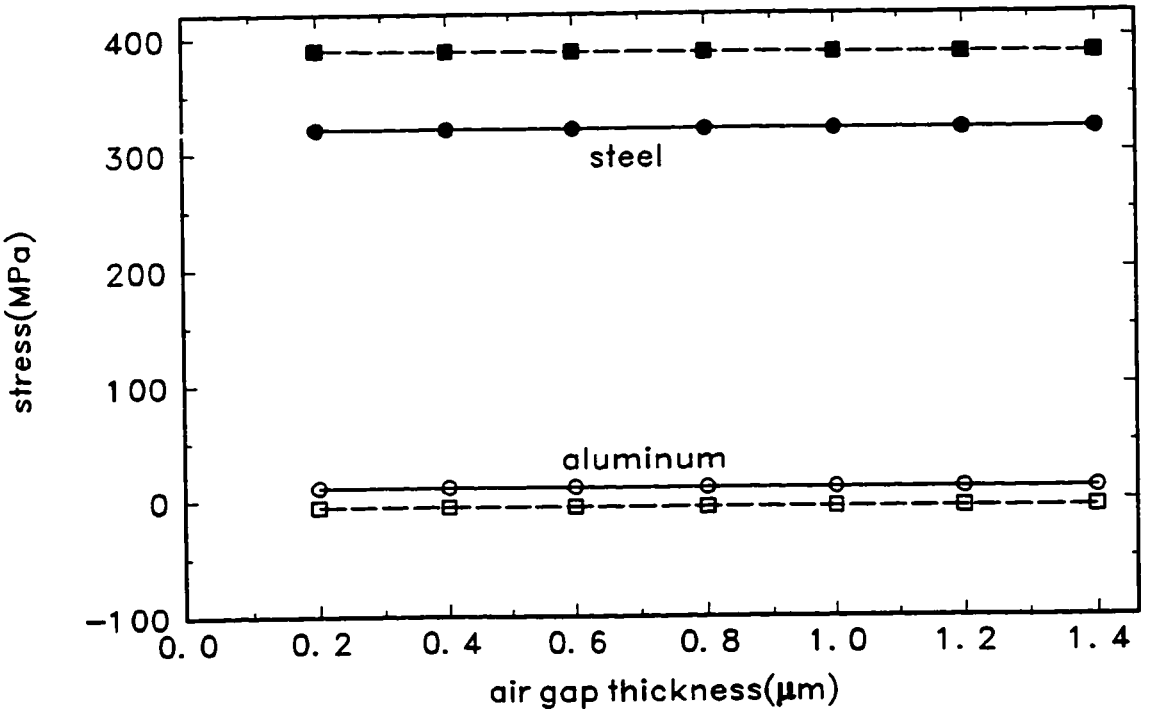

Figure 65 Variation of the steel and aluminum stress with the air gap thickness. Current _____ 200 A _ _ _ 1400 A

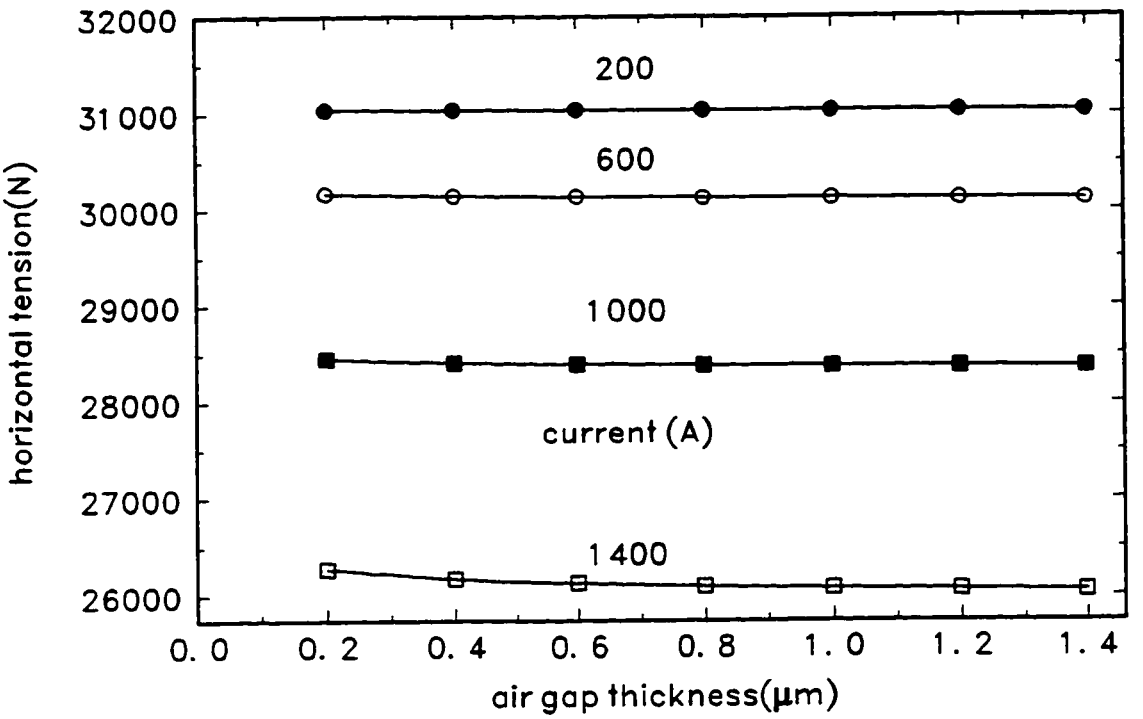

Figure 66 Variation of the horizontal tension of the conductor with the air gap thickness and current.

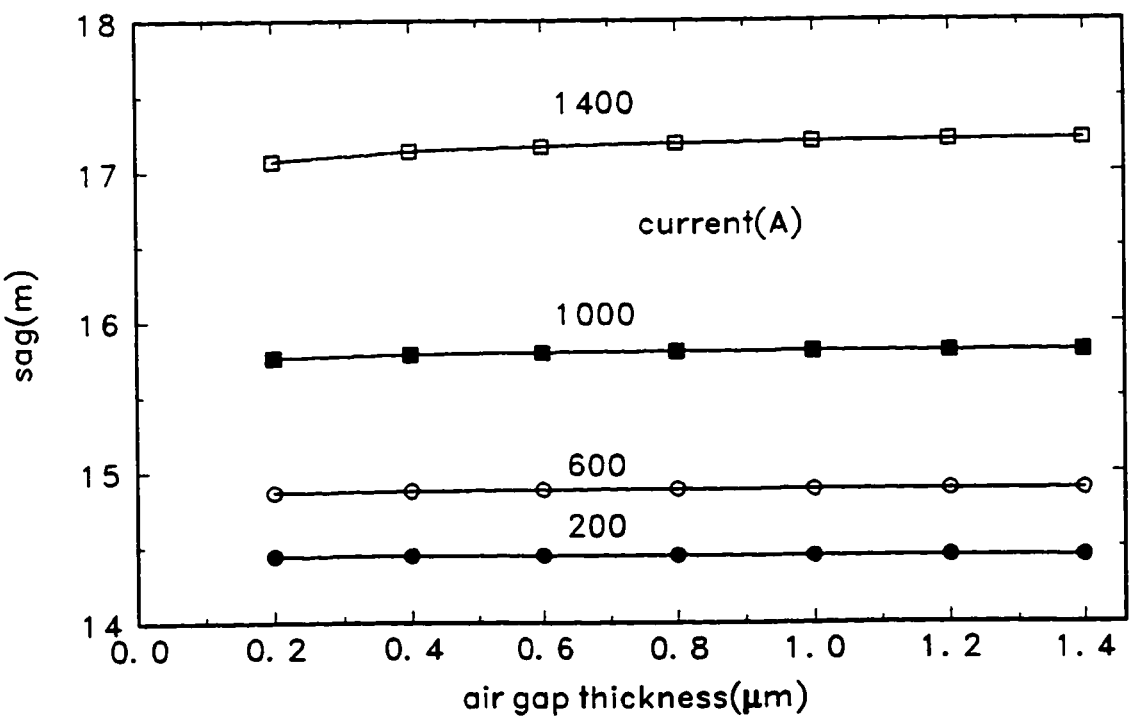

Figure 67 Variation of the sag of the conductor with the air gap thickness and current.

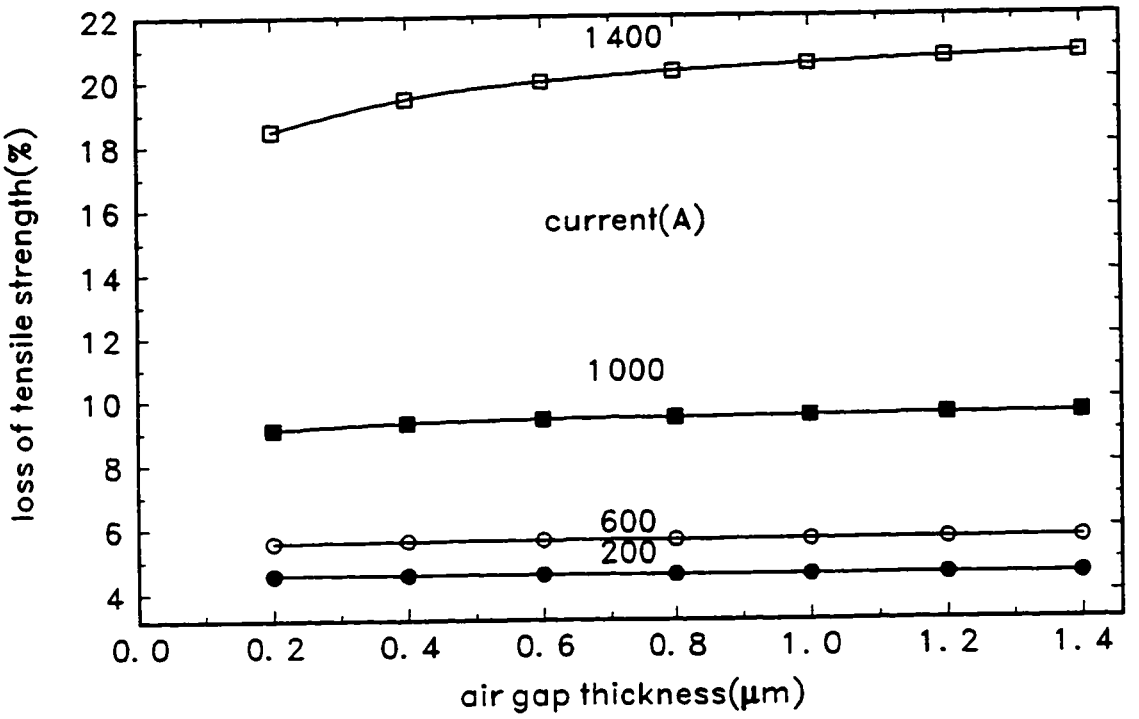

Figure 68 Variation of the loss of tensile strength of the inner aluminum layer with the air gap thickness and current.

4.5 SPAN

The span is changed from 200 m to 600 m in steps of 50 m. It is assumed that the span is the distance between two tension towers. The variations of the span between the suspension towers in a section is not investigated. Birdcaging occurs on some intervals of the probabilistic period, hence in those cases the Unified Model can not be applied for 1400 A for spans less than 400 m.

The electrical characteristics of the conductor are almost unaffected by the variation of the span. The Joule losses and the magnitude of the currents in the layers remain almost constant for all range of the spans. The variation of the ac resistance of the conductor with span and current is shown in Fig. 69. Ac resistance decreases marginally with the span while the aluminum layers are not under compression. For 1000 A the resistance decreases marginally from 6.35×10^{-5} Ω/m to 6.34×10^{-5} Ω/m when the span increases from 350 m to 600 m, as the temperature difference between the layers decreases. Note that the aluminum layers are under compression at 1400 A and at 200 and 250 m for 1000 A. The ac resistance changes slower and at different rates at these points. The variation of the aluminum stress with span and current is seen from Fig. 70.

The variation of the temperature rise of the king wire and aluminum layers with the span for 1000 A is given in Fig. 71. For the spans 200 m and 250 m when aluminum is under compression, the temperature rise is calculated with the assumptions introduced in the Radial Conduction Model. One would expect that the temperature rise would be larger when the aluminum layers are exposed to compressive forces, as the air gap thickness or the distance between metal asperities would be larger, and consequently

convection heat transfer would be smaller. Although for spans of 200 and 250 m it is taken that the air gap thickness is ten times larger, the resulting temperature rise of aluminum layers is still smaller than when there is no compression, for example for a span of 300 m. It is seen again that the hypotheses that the air gap thickness is 10δ and that the area of the metal contacts is based on the maximum conductor stress are not adequate, as evidenced by the calculated radial temperature differences which are underestimated, see sections 4.1 and 4.2.

The same can be concluded from Fig. 72 where the variation of the temperature difference between the king wire and the surface of the conductor with span and current is presented. The temperature difference decreases from 8.2 °C to 6.8 °C, or 1.7 % of the surface temperature rise for 300 m, when the span increases from 300 m to 600 m for 1000 A. As a consequence of the aforementioned assumptions, the temperature differences for 1400 A are almost constant for the range from 400 m to 600 m.

It is seen from Fig. 73 that both steel and aluminum stresses increase with increasing span. The steel stress increases from 294.0 MPa to 385.0 MPa, or 30.9 %, and aluminum stress from -3.2 MPa to 4.6 MPa for the current 1000 A, when the sag increases from 200 m to 600 m.

Fig. 74 shows the variation of the horizontal conductor tension with span and the current. The horizontal tension increases from 20.5 kN to 32.0 kN, or an increase of 55.8 %, when the span increases from 200 m to 600 m, for 1000 A.

The variation of the sag of the conductor with span and current is presented in Fig. 75. The sag increases with the span at a lower rate than square due to the increase of both steel and aluminum stresses. For the current 1000 A, the sag increases from 5.4

m to 31.6 m, or for 485.2 %, when the span increases from 200 m to 600 m. For a fixed current, the span increases at a higher rate than linear with an increase of current.

Fig. 76 shows the variation of the loss of tensile strength of the inner aluminum layer with span and current. The loss of tensile strength remains almost constant for all spans, as the radial temperature difference within the conductor does not change profoundly with span.

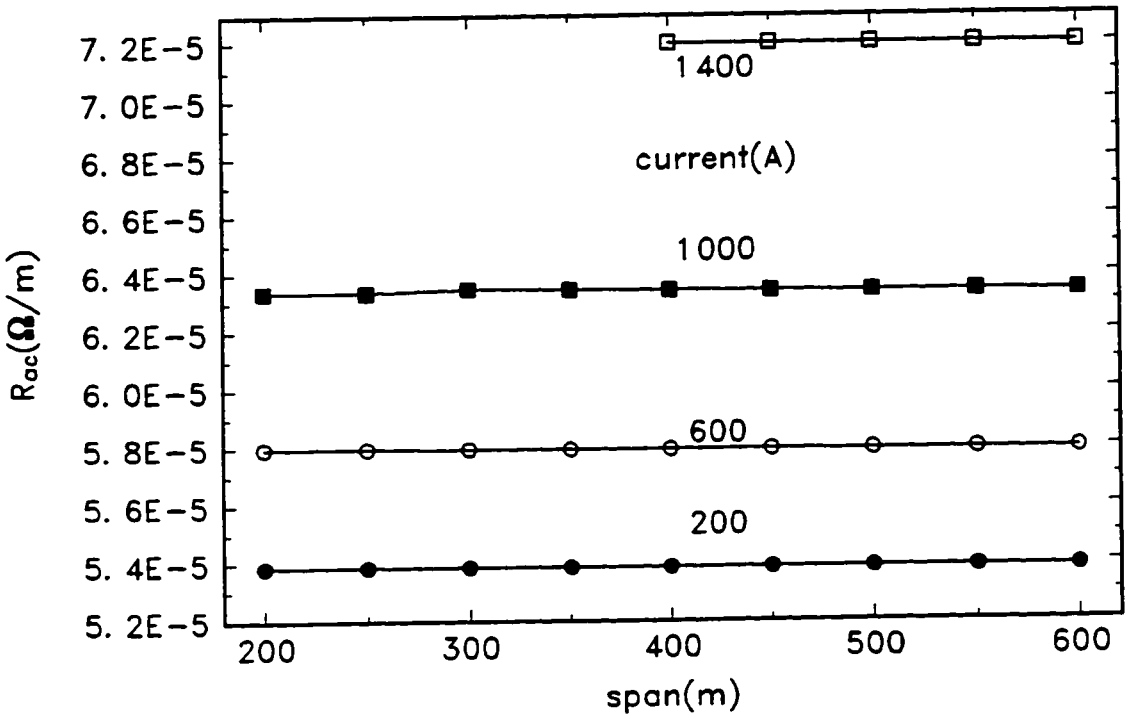

Figure 69 Variation of the ac resistance of the conductor with the span and current.

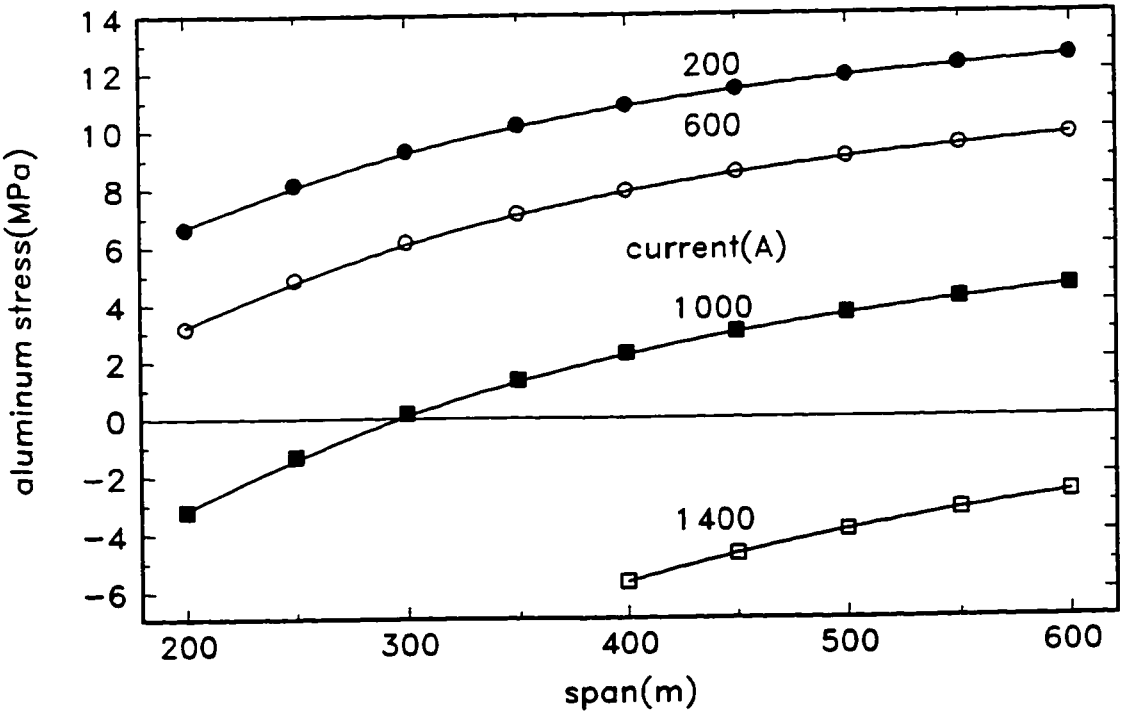

Figure 70 Variation of the aluminum stress with the span and current.

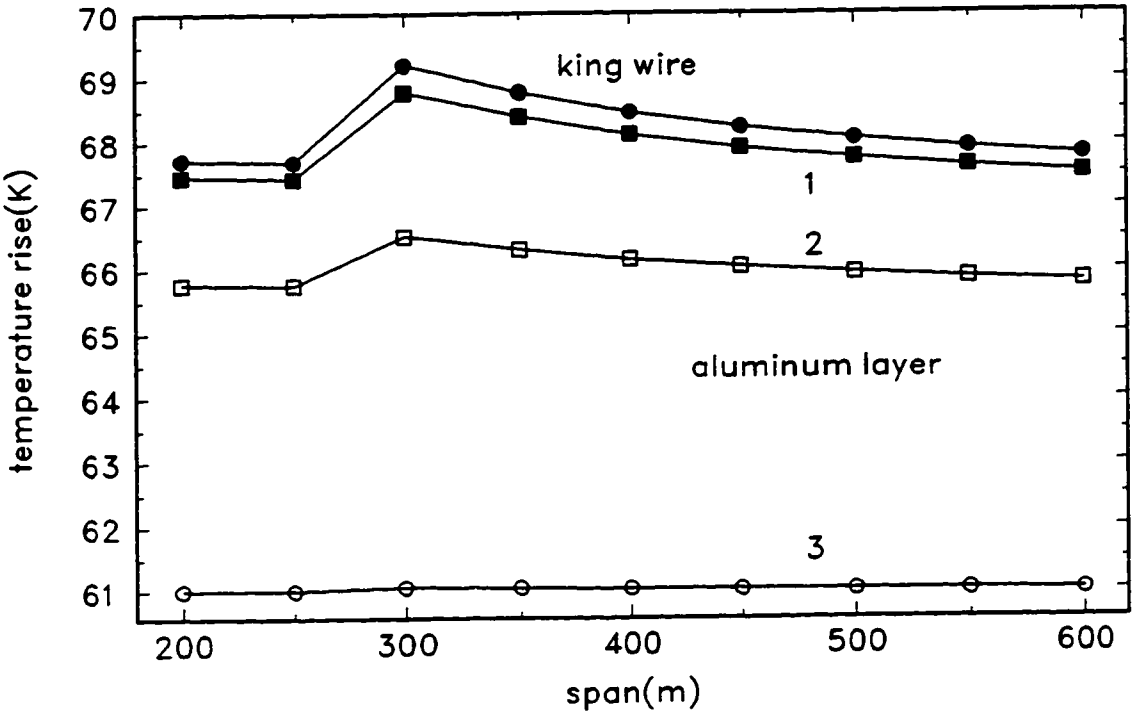

Figure 71 Variation of the temperature rise of the king wire and aluminum layers with the span for the current 1000 A.

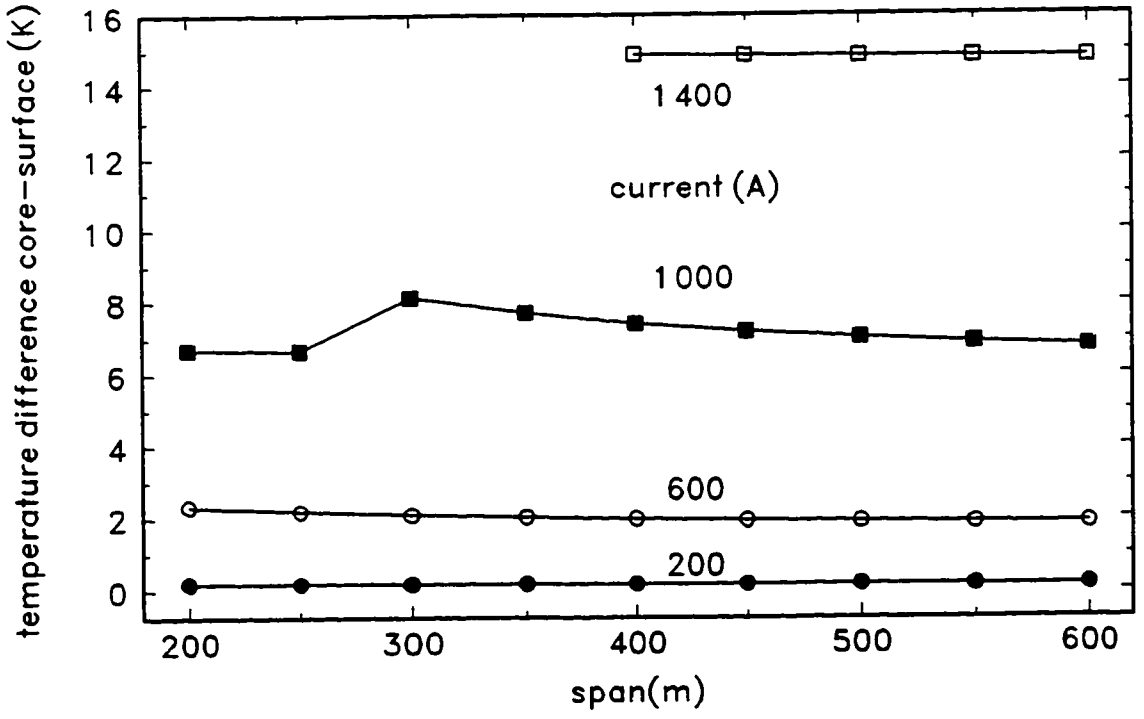

Figure 72 Variation of the temperature difference between the king wire and surface of the conductor with the span and current.

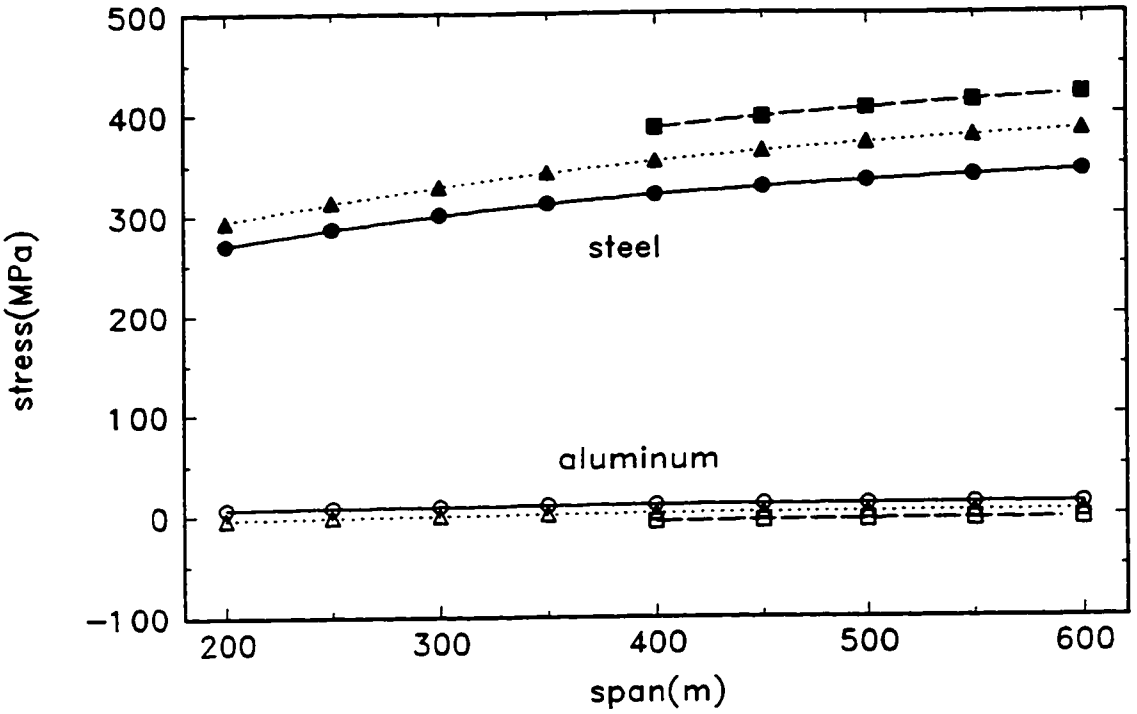

Figure 73 Variation of the steel and aluminum stress with the span. Current
_____ 200 A ..... 1000 A _ _ _ 1400 A

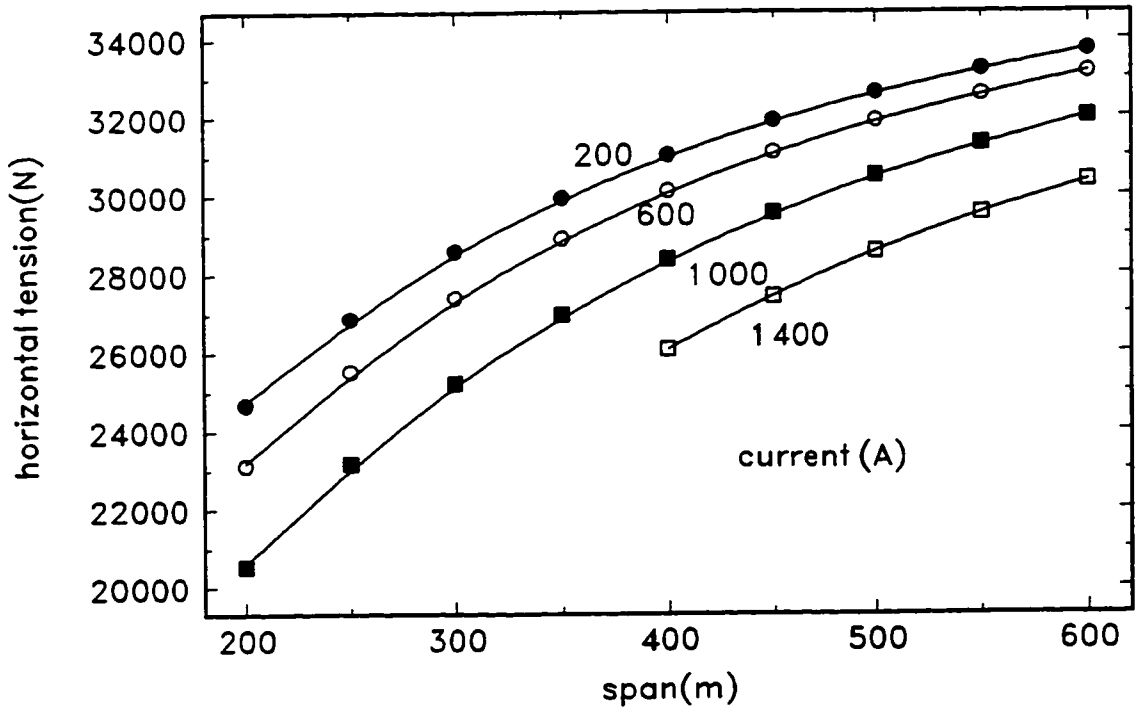

Figure 74 Variation of the horizontal tension of the conductor with the span and current.

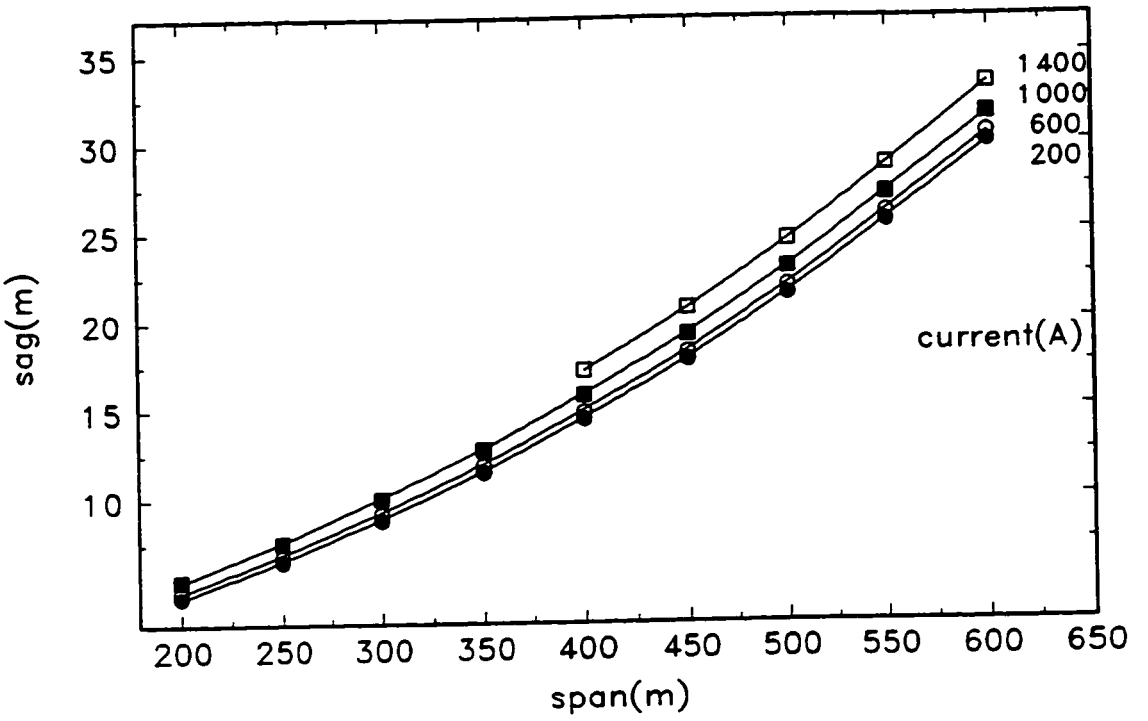

Figure 75 Variation of the sag of the conductor with the span and current.

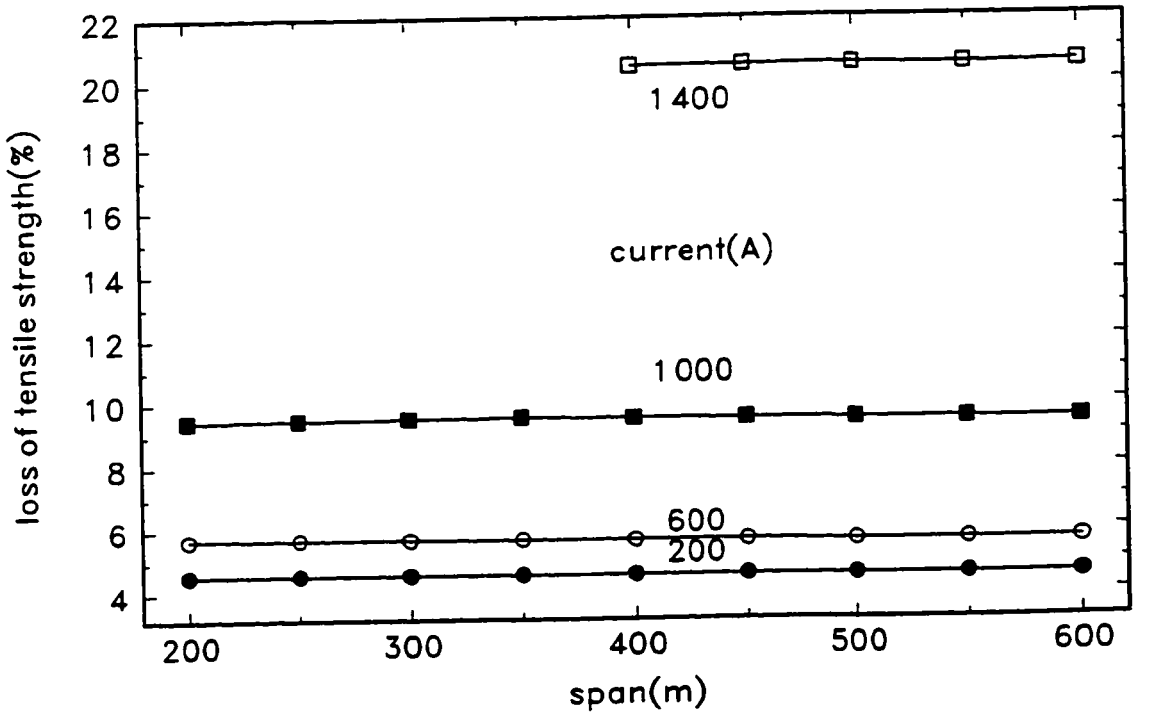

Figure 76 Variation of the loss of tensile strength of the inner aluminum layer with the span and current.

CHAPTER 5

DISCUSSION OF THE RESULTS

An increase in ambient temperature of 10 °C increases Joule losses by approximately 2.8 % for 1000 A and 2.3 % for 1400 A, since both surface temperature and the radial temperature difference within the conductor increase. The temperature rise of the layers above ambient declines slightly with increasing ambient temperature for the same current and thus lowers somewhat the increase of power losses with increasing ambient temperature. However, the benefits are small, since the increase of ambient temperature for 10 °C raises the temperature of the inner aluminum layer by 9.8 °C and of the outer aluminum layer by 9.1 °C for 1000 A. The economical consequences of bigger losses in the areas with higher ambient temperature can be significant during the lifetime of the transmission line.

Results show that the current distribution is not affected significantly by the increase of the ambient temperature.

Table 10 presents magnitudes of layer currents for various ambient temperatures and ranges for which different permeability curves are used, based on steel temperatures T_S. The differences in current distribution can be attributed to the wide range of steel temperatures, for which only three permeability curves are used. However, this shows that the steel temperature for which the permeability data are used affects the current

distribution more than the different temperatures of the aluminum layers. Had we used the permeability curves for actual temperatures there may have been some change of the current distribution. The accurate prediction of the current distribution and ac resistance of the conductor requires data for the variation of the relative complex permeability of the steel cores of the ACSR conductors with temperature, steel wire diameter and the stress.

Table 10 Variation of layer currents and steel temperature with ambient temperature and current.

Curr. (A)	Ambient temp.= 0°C				Ambient temp.= 10°C				Ambient temp.= 20°C			
	T_s (°C)	Curr. in layer (A)			T_s (°C)	Curr. in layer (A)			T_s (°C)	Curr. in layer (A)		
		3	4	5		3	4	5		3	4	5
200	32	43	68	88	41	42	67	88	50	43	67	88
400	36	86	135	175	48	83	135	174	54	86	135	175
600	43	128	206	261	52	123	206	260	62	119	232	246
800	53	167	283	344	64	145	318	323	73	155	317	324
1000	68	186	406	400	78	175	406	398	88	186	406	400
1200	88	214	499	474	99	203	499	473	106	209	511	467
1400	111	237	606	541	120	228	602	540	129	240	599	544

The ratio of ac to dc resistance decreases slightly (third decimal) with an increase of ambient temperature. The dc resistance is calculated from the actual temperatures of the layers so that the resistance ratio can not be used in practice for the simplified prediction of the ac resistance. The ac resistance depends on the temperatures of the layers, and the accurate temperatures can not be calculated when the aluminum layers are under compression. For the accurate calculation of the ac resistance, accurate data for the complex relative magnetic permeability and further development of the Radial Conduction Model for the cases when the aluminum layers are under compression are necessary.

The sag increases with increasing ambient temperature. This means that for the same current rating the height of the transmission line towers in areas with the larger ambient temperatures must be higher. This would mean greater capital cost of the line.

The loss of tensile strength of the aluminum layers due to annealing is affected greatly by ambient temperature. This may prove to be the limiting criterion for the determination of the current rating of transmission lines in some areas with higher ambient temperature.

The exposure time does not greatly affect the current redistribution within layers, ac resistance of the conductor, or power losses, under the assumption that the permeability curves are chosen only on temperature ranges of the steel core and not on the stress (Fig's. 38, 39, 40).

The temperature difference between the king wire and the surface of the conductor increases with time of exposure, as the aluminum transfers tension on the steel portion of the conductor due to settling and metallurgical creep. This decreases the

radial forces on the aluminum layers and the total contact area between them (Fig. 41).

The sag increases with the time of exposure since the steel and aluminum strains grow, but the most of the increase occurs in the first year of the operation (Fig. 41). The increase of the radial temperature difference within the conductor with time contributes to the increase of the sag caused by the creep and settling strains.

If it is assumed that the conductor lifetime is 30 years, most of the loss of tensile strength of aluminum layers due to annealing occurs in ten years (Fig. 47). However, the loss of tensile strength of aluminum layers reaches significant levels after thirty years and can negatively influence the safety factors of the conductor. For that reason the rated tensile strength of the conductor should be decreased to take account of the loss of tensile strength so that the safety factors of the conductor, especially for the maximum load case, are maintained over the whole lifetime.

The intensity of the additional load case affects the aluminum and steel stresses and horizontal tension, but it does not affect the electrical characteristics of the conductor under the assumption that the permeability curves do not depend on stress.

The temperature difference between the king wire and surface increases slightly with the additional load, as the aluminum stress decreases to 0 MPa. However, when the aluminum comes under compression the Radial Conduction Model may be used only with certain assumptions. It is assumed that the metal to metal area is calculated from the maximum aluminum stress that occurs during the conductor lifetime. The maximum stress increases with the increase of ice thickness and, as a result, temperature difference decreases. If the introduced assumption is true, that would mean that the increase of additional loads decreases the temperature difference within the conductor when

compression of the aluminum occurs. Contrarily, larger currents might result in a somewhat smaller sag of the conductor.

The duration of the particularly selected additional load does not affect the mechanical and electrical characteristics of the conductor. Apparently selected additional load affects the permanent elongation and consequently the aluminum and steel stresses and the temperature rise of the layers for the same amount as it is influenced by the high temperatures at the probability based period. However, it has to be born in mind that the additional load is applied before the probability based period that influences the calculation of the permanent elongation.

For the conventional practice of design of transmission lines, the duration of the additional load is important. The results suggest that the duration of the additional loading case is not important as long as the probability based approach is taken. Nevertheless, the increase of the duration of the additional load case automatically decreases the duration of the high temperatures in the probability based period, which results in a decrease of the loss of tensile strength of aluminum layers due to annealing.

The air gap thickness does not significantly alter the electrical and mechanical characteristics of the conductor for currents up to 1000 A. For larger currents, such as 1400 A, the more conspicuous increase of the air gap thickness increases radial temperature difference within conductor, so that the temperatures of the inner and middle aluminum layers and steel layers are bigger. That causes a change in current distribution, decreases slightly the steel stresses, increases the sag of the conductor and increases the loss of tensile strength of the inner aluminum layers. This suggests that the air gap thickness is not a major factor for currents less than the rated current.

Although the stresses, horizontal tension and sag change significantly with span, the electrical characteristics of the conductor remain almost the same, under the assumption that the permeability does not depend on stress. The radial temperature difference between layers decreases slightly with increasing span and an increase of steel and aluminum stresses. However, the sensitivity of the radial temperature difference between layers on the change of the stresses does not appear to be very great.

The assumptions that the metal to metal contact area can be calculated from the maximum stress which occurred in a conductor during the previous exposure period, and that the air gap thickness is ten times the standard air gap thickness, are introduced in the Radial Conduction Model for birdcaging. Calculated radial temperature differences for the spans where aluminum compression occurs show that the assumptions are not adequate. These assumptions underestimate the radial temperature difference within the conductor even when the results are compared with the cases without aluminum compression. It seems logical to expect that the radial temperature differences within the conductor with the aluminum layers under compression, should be even higher then those without the aluminum compression.

The radial temperature differences within the conductor influence the current redistribution among layers and the mechanical characteristics of the conductor. Application of the Unified Model at higher currents may suggest that the aluminum compression may occur. This is of the particular interest. Hence, further research and improvement of the Radial Conduction Model would enhance the reliability of the model.

The radial temperature difference within the conductor affects the current distribution within layers, and, consequently the ac resistance of the conductor, in two

ways. The first effect results from the different temperatures of aluminum layers giving rise to differing dc resistances of the strands in a given layer. The second is through the dependence of the complex relative magnetic permeability of the steel core on the steel core temperature. The second effect is more significant.

The current density in the middle aluminum layer is the greatest, in the outer layer less, and in the inner layer the least (Fig. 23). The significant increase in the radial temperature difference, such as is shown in Fig. 64 due to the increase of the air gap thickness for the 1400 A current, decreases the current in the middle layer and increases the current in the outer layer, Fig. 62, and so decreases the current distribution. It can be concluded that the larger radial temperature difference such as occurs at higher currents, ameliorates somewhat the current redistribution within layers and decreases the difference between the current densities in the middle and outer layer. Judging on the results obtained for the current redistribution for the various ambient temperatures, that change in current distribution within layers is caused mainly by the effects which an increase of radial temperature difference has on the magnetic properties of the steel core, and not by larger temperature differences between aluminum layers. However, this effect is not pivotal, and for the smaller radial temperature differences, such as for the variation of the air gap thicknesses for 1000 A, the current redistribution within layers remains almost unaffected.

The ac resistance of the conductor is more affected by the absolute temperatures of the layers than by the radial temperature differences within the conductor. Results show that, for the permeability data taken for a wide range of steel temperatures, when the radial temperature differences increase the ac resistance is more affected by the

absolute temperatures of the aluminum than by the increase of the steel temperature and the change in the complex magnetic permeability.

The electrical characteristics of the conductor are not affected conspicuously by the change of the steel and aluminum stresses. With increasing time of exposure, for instance, the mechanical characteristics of the conductor change significantly without any effects on the electrical characteristics of the conductor.

The surface conductor temperature remains constant when the Joule losses do not change. So the variation of the mechanical characteristics do not affect the surface temperature of the conductor, but affect the radial temperature difference.

The results of the probability based Unified Model are affected by the order in which the load periods and intervals within the periods are taken.

IMPLEMENTATION OF MECHANICAL MODEL

Although the Mechanical Model has been proven through various tests, there are some drawbacks which have to be considered. When the sequence of the cumulative loadings is changed, the predicted results change. The sag and tension calculation is already uncertain when the periods with different loads, tensions and temperatures, which determine the permanent elongation of the conductor, have to be assumed. The uncertainty is increased with the dependence of the calculation on the sequence in which the loads are applied.

Although the transfer of the stress from aluminum to steel due to high temperatures and creep is considered, the transfer of the stress between aluminum layers at differing temperatures and stresses cannot be predicted. The model should be

developed further to allow prediction of the strains and stresses within layers and to enable more accurate calculation of the conductor sag. The stress-strain curves for each layer would have to be checked and the set of nonlinear equations would have to be solved for the layer stresses for each interval. Even if the steel layers were to be calculated together and represented by one strain summation equation, the number of nonlinear equations would be equal to the number of aluminum layers in a conductor plus that for the steel core.

COMPARISON OF THE PROBABILITY BASED UNIFIED MODEL AND THE CONVENTIONAL DESIGN PRACTICE

The most common procedure, here called the conventional design practice, used for the prediction of the characteristics and the behaviour of the conductor nowadays is compared with the probability based Unified Model. An overview of the conventional design practice and its input data used for the purpose of comparison is given below.

Usually the Radial Conduction Model is not taken into consideration when the conservative static rating is employed. The radial temperature differences and the increased higher sag are neglected with the explanation that the radial temperature differences for currents less than the traditional thermal rating are smaller than 10 °C, and therefore negligible.

In conventional design practice, the ac resistance of the conductor is usually taken from published tables, such as given in [28], where it is calculated from the dc resistance of the conductor for a given conductor temperature. The corrections for the skin effect are included in ac resistances given in tables. For ACSR conductors with an odd number

of aluminum layers, the additional correction for the magnetizing effects of the core need to be applied [28]. The ac resistances for low temperatures, such as 20 °C and high temperatures usually pertaining to the traditional current rating and conductor temperature 75 °C are determined as above. The ac resistances for temperatures in between are calculated by linear extrapolation and are claimed to be slightly higher then they really are and thus conservative for the rating calculations. The ac resistances of conductors above 75 °C obtained in this way are deemed to be somewhat lower and non-conservative for the rating calculations.

The method, usually used in conventional design practice, for the calculation of the steady-state current ratings is given in ANSI/IEEE Standard 738-11/89. For the purpose of comparison, the parameters for the wind speed and direction, emissivity and absorptivity of the conductor, altitude, azimuth, and latitude are imputed in the IEEE method of calculation for the ambient temperature of 20 °C at solar noon and with clear sky, the same as in Table 5. The ac resistance for the conventional design practice is calculated from [28] for 20 °C and 75 °C, and linearly interpolated for other temperatures.

The same Mechanical Model is employed within the Unified Model and for the conventional design practice for the purpose of comparison. However, the probabilistic approach for the thermal history of the conductor is introduced in the Unified Model. The conductor history for the conventional design practice for the exposure time of 10 years is usually assumed as: running out period at ambient temperature 20 °C and at 20 % of RTS for one hour, stringing at ambient temperature 20 °C and at 20 % of RTS for one hour, additional load case with ice thickness of 6.35 mm and wind pressure of 385

MPa for 0.1 year, conductor temperature 20 °C for 9.8 years, and maximum conductor temperature calculated from the IEEE method for the given current for 0.1 year. The sag of the conductor and the stresses are then calculated after 0.5 hour after the assumed period of approximately 10 years.

The procedure chosen to show the conventional design practice is conservative, and it is claimed that the power losses and sag obtained in this way are larger than they are in reality for temperatures less than 75 °C, and only somewhat smaller for temperatures greater than 75 °C.

The comparison of the heat losses and gains obtained by Unified Model with the probabilistic approach and conventional design practice for various currents is shown in Fig. 77. Joule losses for 1000 A from the probability based Unified model are 63.4 W/m, which is 4.5 % more than predicted by the conventional procedure. That difference is the consequence of the conventionally calculated ac resistance which is claimed to be exact for the current of 1000 A where the calculated temperature of the conductor surface is 75 °C. Besides, the solar heating obtained by the Steady-State Model [14-16] is higher than that obtained by the IEEE method. The conventional approach predicts the Joule losses which are less than predicted by the probability based Unified Model.

Fig. 78 shows the variation of the heat gains and losses with the surface conductor temperature from both the probability based Unified Model and the conventional approach. For the fixed surface temperature of the conductor, the conventional approach outputs bigger Joule losses than the probability based Unified Model, the absolute difference being less for the bigger surface temperature of the conductor. However, the

surface temperatures and surface temperature rises are bigger when calculated by the probability based Unified Model than when calculated by the conventional way for the same current, what is shown in Fig. 79. For the current 1000 A, the probability based Unified Model predicts a surface temperature rise of 61.0 °C and the conventional method 56.3 °C.

As shown in Fig. 80 the ac resistance predicted by the probability based Unified Model is larger than that calculated by the conventional approach for the fixed current. For 1000 A the difference is 4.5 % and increases with increasing current. For the conventional approach the ac resistances for the currents larger than 1000 A, meaning the temperatures greater than 75 °C, are claimed to be bigger than shown. At the same time the calculation of the ac resistance for currents 1200 and 1400 A in the probability based Unified Model is based on the assumptions introduced in the Radial Conduction Model for the cases of aluminum compression. It can be expected that the values of ac resistances would be larger than shown if the radial temperature differences within the conductor are not underestimated. This suggests that the difference between ac resistances for the currents larger than 1000 A calculated by the two methods may even increase with increasing current. The conventional method underestimates ac resistance of the conductor significantly.

The variation of the steel and aluminum stresses and the horizontal tension of the conductor with the current for the probability based Unified Model and the conventional approach are presented in Fig. 81 and Fig. 82. The conventional approach predicts bigger horizontal tension for the fixed current. The difference increases from 2.5 % of the horizontal tension predicted by the probability based Unified Model for 200 A to 3.5

% for 1400 A. The reasons are the smaller surface temperatures obtained by the conventional approach, neglecting the radial temperature differences, and the assumed deterministic thermal history of the conductor in the conventional approach.

As shown in Fig. 83, the sag of the conductor is significantly bigger when predicted by the probability based Unified Model than by the conventional approach for the same current. The differences are the consequence of the higher horizontal tensions predicted by the conventional approach. The sag of the conductor calculated by the probability based Unified Model is bigger for 0.43 m for 1000 A and 0.58 m for 1400 A. The conventional approach significantly underestimates the conductor sag.

The differences between the results of the probability based Unified Model and the conventional approach are caused by simplified IEEE method for the calculation of the steady state used in conventional approach, the deterministic assumptions employed in the conventional method versus the probabilistic approach introduced within the Unified Model, omittance of the radial temperature differences in a conventional approach, conventional calculation of the ac resistance by correction factors versus the Electromagnetic Model embedded in the Unified Model, and separate use of only two models versus the interactive combination of all four models within the Unified Model. The probability based Unified Model predicts electrical, thermal and mechanical characteristics taking account of the realistic history of the conductor and all the interdependences between the variables and phenomena within all four models.

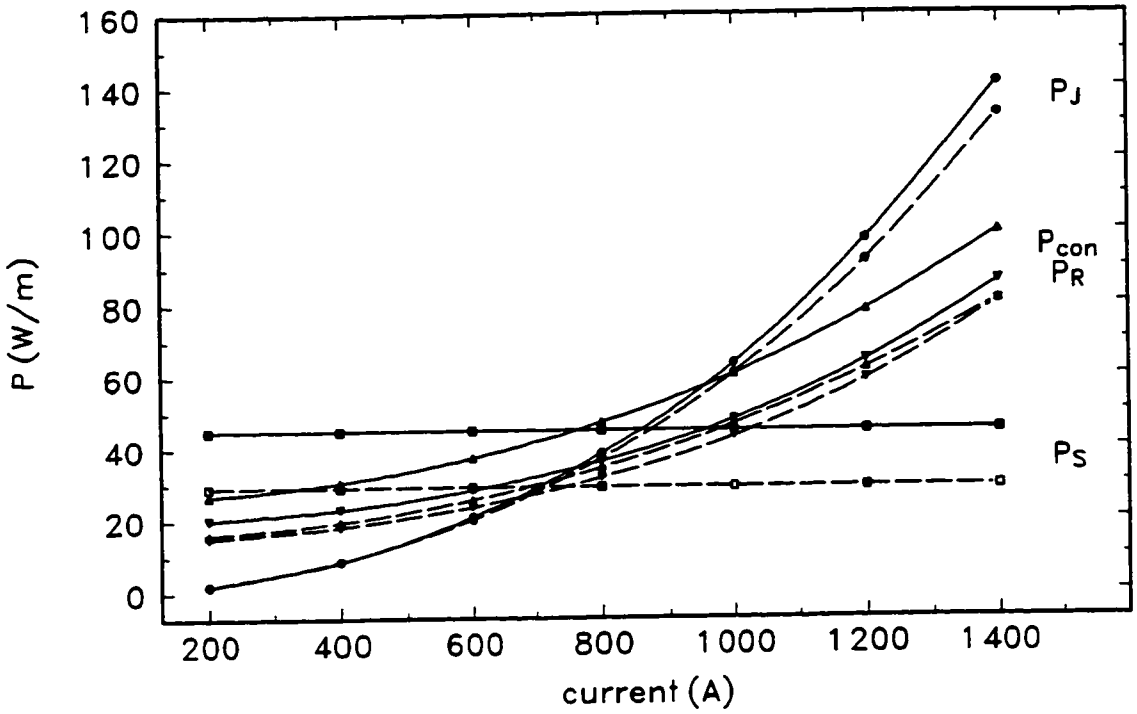

Figure 77 Variation of the heat gains and losses with current.
_____ probability based Unified Model
_ _ _ conventional approach

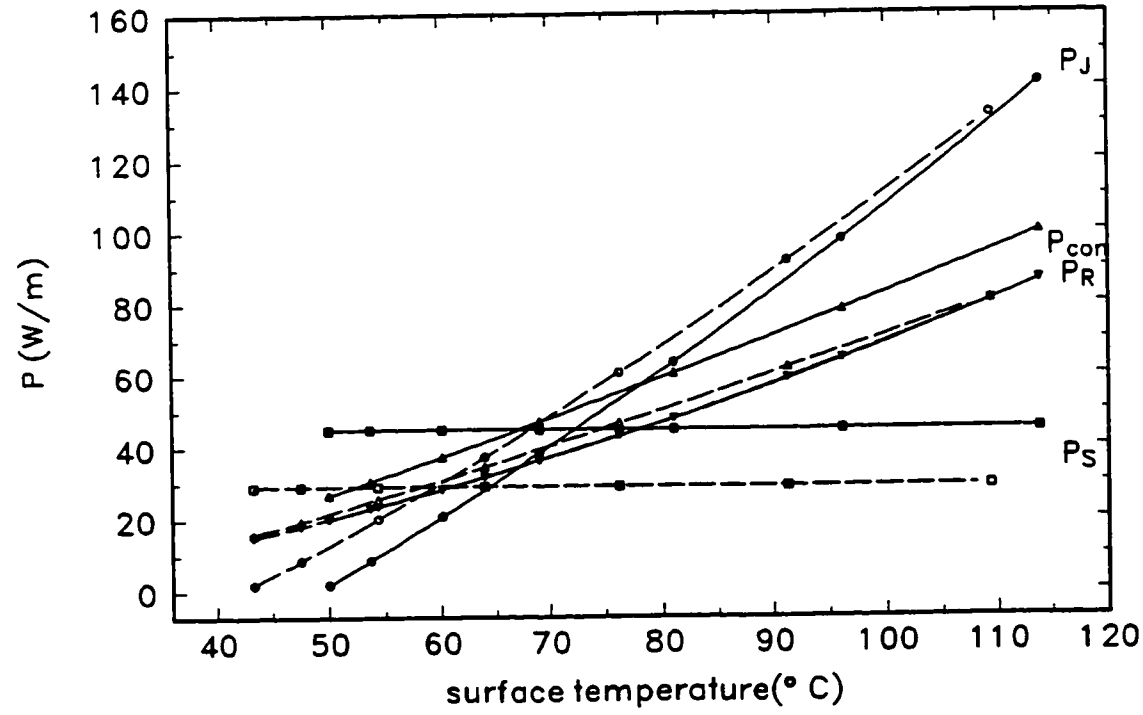

Figure 78 Variation of the heat gains and losses with the surface temperature of the conductor.
_____ probability based Unified Model
_ _ _ conventional approach

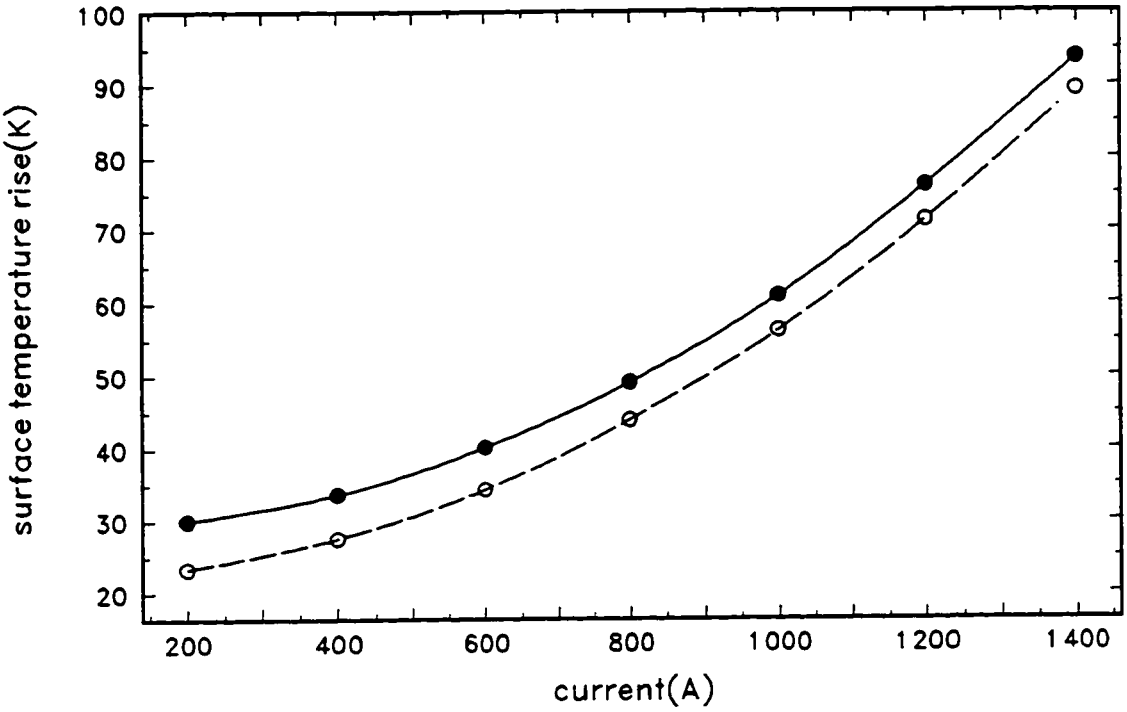

Figure 79 Variation of the surface temperature rise of the conductor with current.
_____ probability based Unified Model
_ _ _ conventional approach

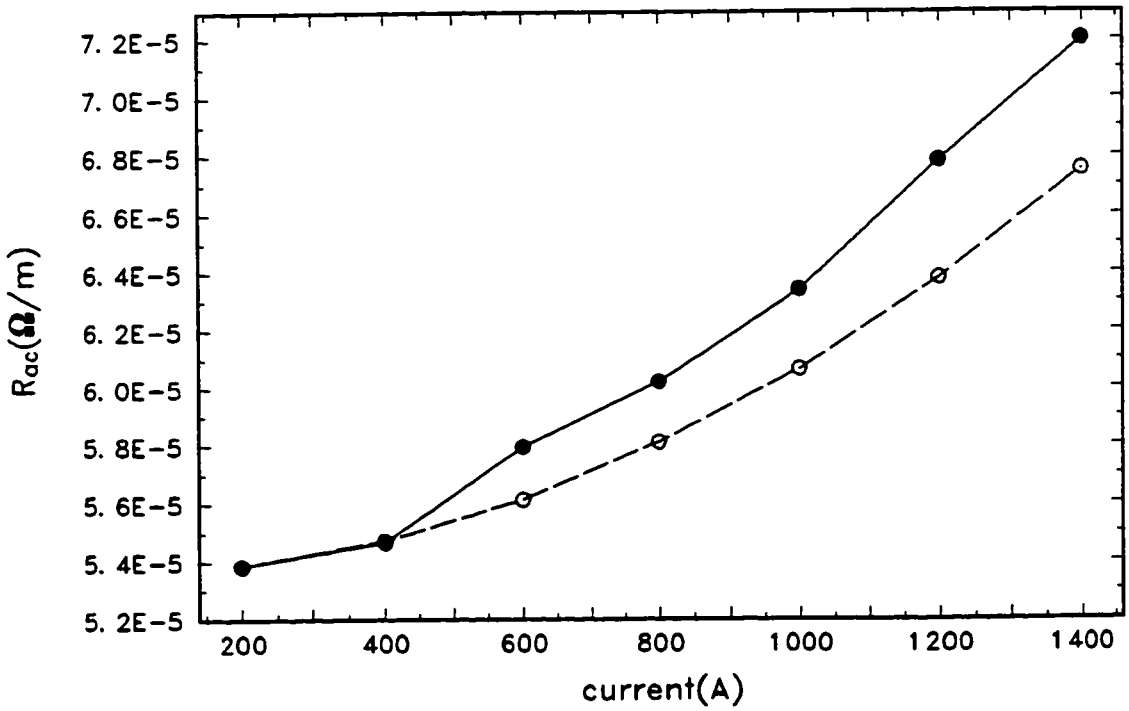

Figure 80 Variation of the ac resistance of the conductor with current.
_____ probability based Unified Model
_ _ _ conventional approach

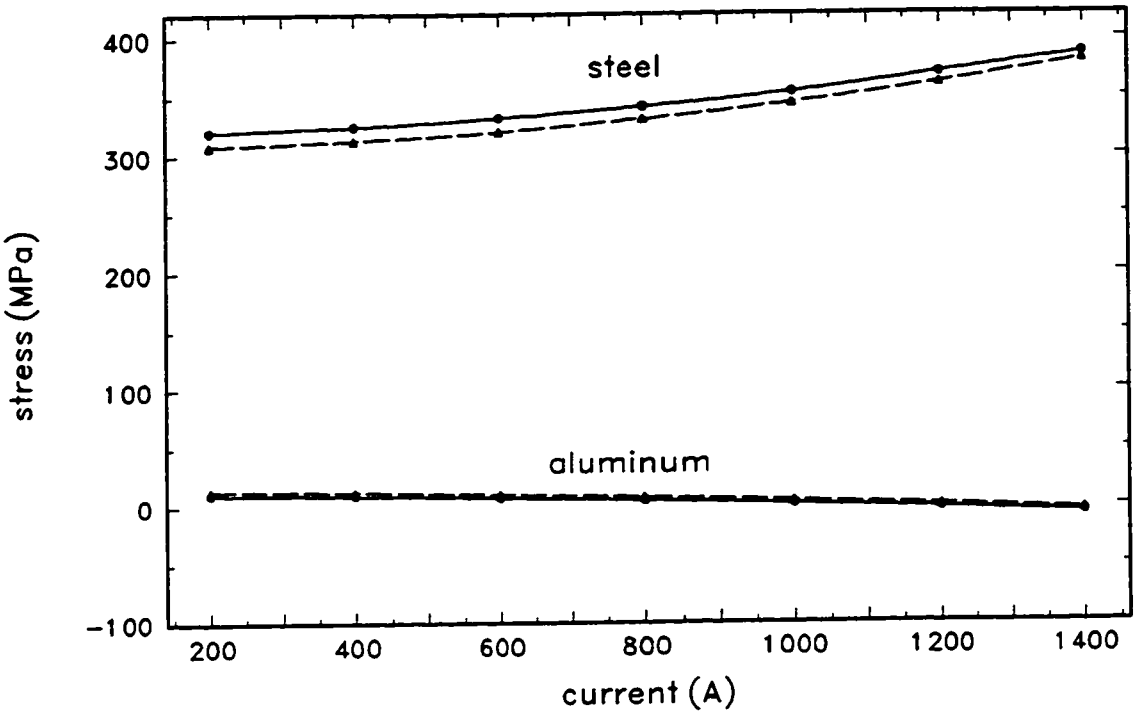

Figure 81 Variation of the steel and aluminum stresses with current.
_____ probability based Unified Model
– – – conventional approach

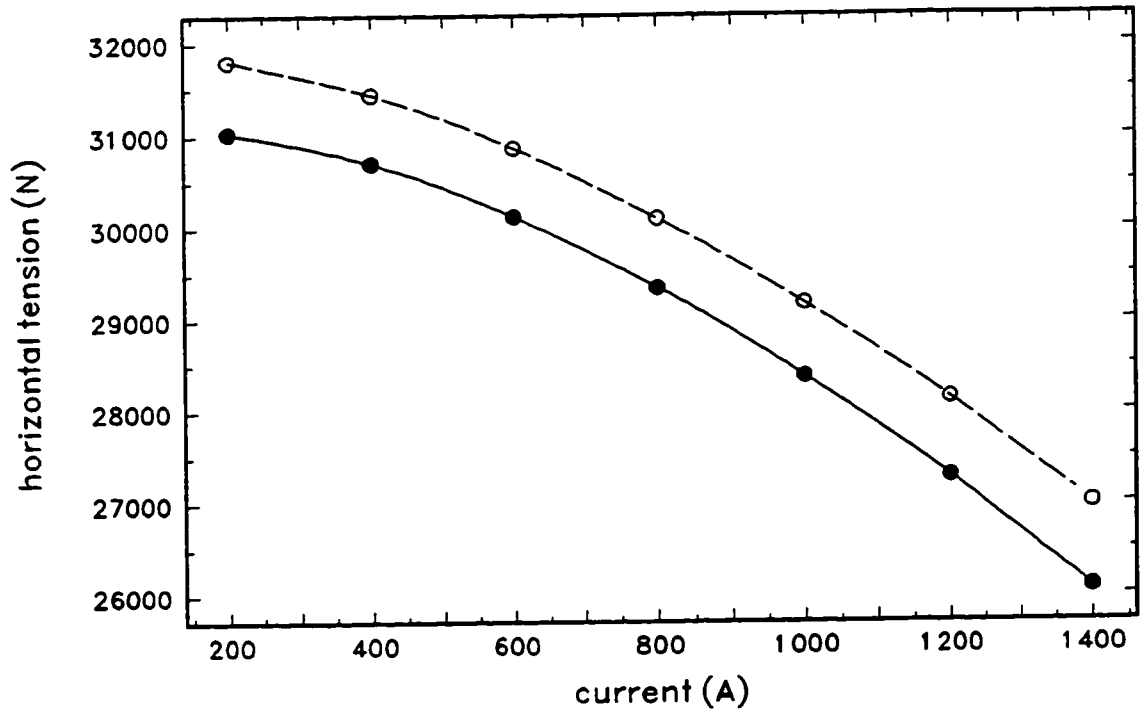

Figure 82 Variation of the horizontal tension of the conductor with current.
_____ probability based Unified Model
– – – conventional approach

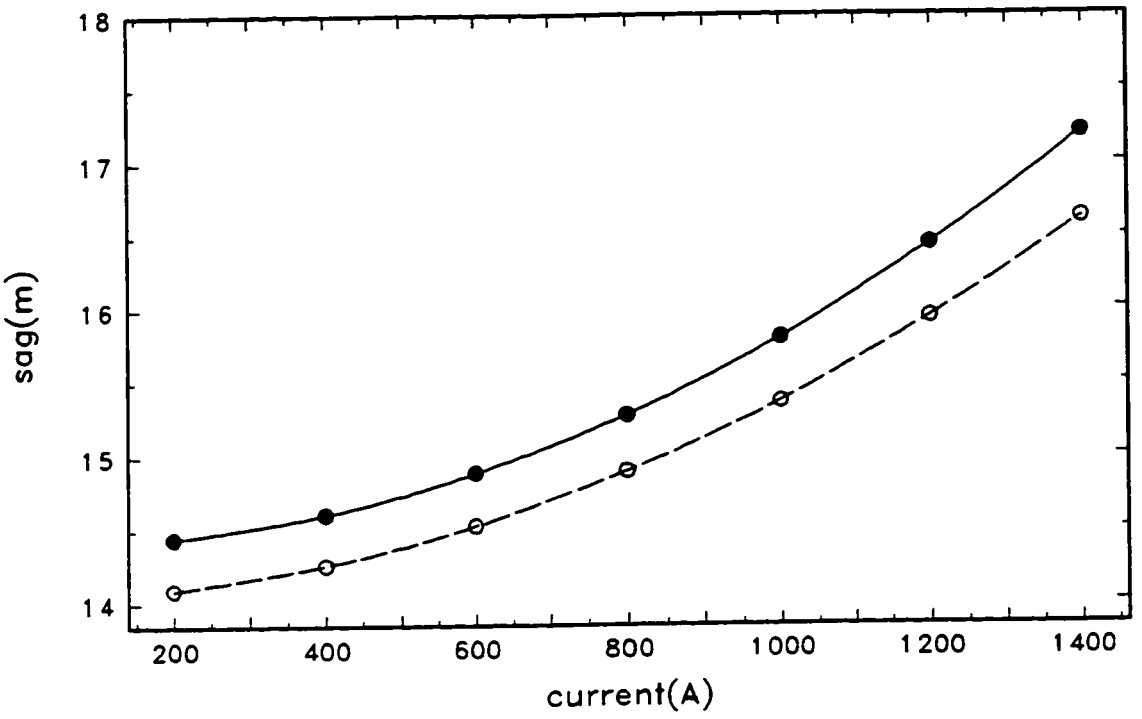

Figure 83 Variation of the sag of the conductor with current.
_____ probability based Unified Model
_ _ _ conventional approach

CHAPTER 6

CONCLUSIONS

The Unified Model, an original work that enables the simultaneous prediction of all aspects of the behaviour of the overhead conductor in a seamless fashion, is developed. For the first time, electromagnetic, mechanical, steady-state transfer, and radial conduction models, that were separately used in the past, are combined and their mutual influences are taken into consideration. This is of particular importance for accurate prediction of the conductor behaviour at high temperatures where the dependencies between the models are not negligible any more. Relations between existing models are explicitly defined. Although interdependencies between models were known, they have never been explicitly stated. In addition, the probabilistic approach is introduced in the Unified Model which, in combination with overall prediction of the characteristics of the conductor, enables realistic evaluation of the conductor thermal history and, for the first time, the realistic prediction of mechanical characteristics such as birdcaging, annealing, etc. The calculation of the loss of tensile strength of the nonferrous layers due to annealing is included into the Unified Model and will be incorporated in design practice for the first time.

This work created a general procedure that successfully couples four models and

gives results from all models by equilibrating common variables. The Model is especially applicable to ACSR conductors. Complete software has been developed to accomplish the above. In order to connect the four existing models, each of them has been developed further. Combination of steady-state thermal model and electromagnetic model that calculates surface temperature corresponding to power losses from both models represents an improvement in the integrated Model compared to results from separate models. The mechanical model is extended to apply the probabilistic approach and to include annealing.

The Model is applied to ACSR Grackle conductor. Results reveal relations among coupling variables; most of them are given for the first time. All aspects of the conductor behaviour are now predicted simultaneously, these studies were not possible without the Unified Model. For example we can now predict the occurrence of birdcaging when a realistic history is considered. As well, we can predict the power loss relation with the radial temperature differences within the conductor after a period of exposure. The Model enables accurate prediction of the temperatures of the layers, power losses, currents in layers and ac resistance of the conductor, stresses and tension in the conductor, sag of the conductor, loss of tensile strength of the nonferrous layers due to annealing ,etc.

The Unified Model should prove to be a powerful tool for manufacturers in the design of new conductors and improvement of existing conductors for the reduction of losses, optimization of electrical and mechanical characteristics, etc. The application of the probability based Unified Model can be used to investigate other effects in conductor design, such as the reduction of the calculated Rated Tensile Strength (RTS) of the

conductor to allow for the predicted loss of tensile strength of aluminum wires for the lifetime of the conductor.

The Model will also be very useful in operations, for accurate prediction of the characteristics of the conductor at increased temperatures in order to improve safety through accurate evaluation of the sag and annealing, to decrease power losses, to determine maximum transmissible power. The Unified Model can be readily applied for estimation of the conductor lifetime and for the real-time prediction of the maximum permissible transfer based on weather forecasting within the SCADA.

It will also be very applicable for the design and optimization of the overhead transmission and distribution lines, since it predicts mechanical, electrical, electromagnetic, and thermal characteristics or the conductor in a seamless fashion. Accurate prediction of the sag and power losses are also very important for the economic evaluation of the design and for operational practice.

The sensitivity of the conductor parameters to atmospheric variables, such as wind speed and solar irradiation, can be readily determined. The probability based Unified Model fully describes the conductor as used in shorter lines and, together with the stability analysis, for longer lines.

Application of the probability based Unified Model to ACSR Grackle conductor shows the relations among electrical, thermal and mechanical parameters of the conductor and the effects which the ambient temperature, time of exposure, additional loads, air gap thickness, and span have on them. The main results of the application can be summarized as follows:

1. The radial temperature differences within a conductor affects the current distribution and the ac resistance of the conductor more through the change of the complex magnetic permeability with increasing steel temperature than through increased temperatures of the inner aluminum layers.

2. The changes in aluminum and steel stresses do not significantly affect the electrical characteristics of the conductor.

3. Radial temperature differences within the conductor are not very sensitive to changes in the aluminum and steel stresses.

4. The surface temperature of the conductor is not significantly affected by the mechanical stresses in aluminum and steel.

5. The loss of tensile strength of aluminum layers due to annealing reaches a significant level during the lifetime of the conductor, and thus may have a major impact on the reliability of the line.

6. When the aluminum layers are under compression, either the air gap thickness is greater than ten times the air gap thickness under tension or the metal to metal contact area is smaller than that formed by the maximum stress which occurs during the conductor lifetime, or maybe both.

7. Air gap thickness does not seriously affect the mechanical and electrical characteristics of the conductor for currents less than the conventional current rating.

8. The conventional design practice significantly underestimates power losses, ac resistance and the sag of the conductor.

RECOMMENDATIONS

Some observations regarding the design of the overhead line conductors are:

1. The rated tensile strength of the conductor used in design practice should be decreased to account for the loss of tensile strength of the aluminum for the whole predicted lifetime of the conductor. The safety factors for the conductor will be maintained in this way.

2. The probability based Unified Model should be employed instead of the conventional approach to ensure safety (sag), reliability (loss of tensile strength), and economical assessment (power losses) of overhead lines.

3. There is not enough statistical information from any published source to verify the Model. The Unified Model should be implemented as a part of SCADA to collect statistical operations data during longer period of time to verify the Model.

FURTHER WORK

More work on the separate models is necessary. For example, the Radial Conduction Model is experimentally verified only when the layers are not under compression. For the application of the Unified Model at larger currents and thus higher temperatures, the Radial Conduction Model should be extended and verified for the prediction of both the case with aluminum stresses less than zero before birdcaging occurs and during birdcaging.

The Mechanical Model should be developed further to predict the strains and

stresses in each layer.

Data on the complex relative magnetic permeability of the steel core of the conductors and its variation with temperature, steel wire diameter and stress should be obtained. This information is a prerequisite for the wider use of the Unified Model. Alloys for the steel wires should be standardized.

Further development of the Unified Model should include statistical variation of the current, ambient temperature, solar radiation intensity , and wind speed and direction, and their simultaneous Monte Carlo treatments. The purely random values of these parameters will be used simultaneously for the evaluation of the conductor history and the prediction of conductor parameters.

REFERENCES

[1] V.T Morgan and C.F. Price, "Magnetic Properties in Axial 50 Hz Fields of Steel Core Wire for Overhead-Line Conductors", Proc. IEE, Vol. 116, 1969, pp. 1681-1694.

[2] J.S. Barrett, O. Nigol, C.J. Fehervari and R.D. Findlay, "A New Model of AC Resistance in ACSR Conductors", IEEE Trans. on Power Delivery, Vol. PWRD-1, 1986, pp. 198-208.

[3] T. Varney, "ACSR, Graphic Method for Sag-Tension Calculations", Aluminum Company of America, June 1927.

[4] C.A. Jordan, "A Simplified Sag-Tension Method for Steel-Reinforced Aluminum Conductors", AIEE Trans. Pt. III, Vol. PAS-71, 1952, pp. 1108-1118.

[5] CIGRE WG 22-05, "Predictor Equations for Creep of Conductors", Electra, No.75, 1981, pp. 63-98.

[6] O. Nigol and J.S. Barrett, "Characteristics of ACSR Conductors at High Temperatures and Stresses", IEEE Trans. on Power Apparatus and Systems, Vol. PAS-100, 1981, pp. 485-493.

[7] J.S. Barrett, S.Dutta and O.Nigol, "A New Computer Model of ACSR Conductors", IEEE Trans. on Power Apparatus and Systems, Vol. PAS-102, 1983, pp. 614-621.

[8] J.S. Barrett, "Optimization of Conductor Design", IEEE Trans. on Power Delivery, Vol. PWRD-4, 1989, pp. 453-460.

[9] V.T. Morgan, "The Radial Temperature Distribution and Effective Radial Thermal Conductivity in Bare Solid and Stranded Conductors", IEEE Trans. on Power Delivery, Vol. PWRD-5, 1990, pp. 1443-1452.

[10] V. T. Morgan and R.D. Findlay, "Effects of Axial Tension and Reduced Air Pressure on the Radial Thermal Conductivity of Stranded Conductors', IEEE Trans. on Power Delivery, Vol. PWRD-8, 1993, pp. 553-558.

[11] B.Yu Makhlin, "Conductor Heating and its Effect on Their Mechanical Strength", TSNIEL Trudy, Vol. 5, 1956, pp. 186-202.

[12] H.E. House and P.D. Tuttle, "Current-Carrying Capacity of ACSR", AIEE Trans. Pt. III, Vol. PAS-77, 1958, pp. 1169-1178.

[13] A. Webs, "Dauerstrombelastbarkeit von nach DIN 48201 gefertigten Freileitungsseilen auf Kupfer, Aluminium und Aldrey", Elektowirts, Vol. 62, 1963, pp. 861-872.

[14] V.T. Morgan, "Rating of Bare Overhead Conductors for Continuous Currents", Proc. IEE, Vol. 114, 1967, pp. 1473-1482.

[15] V.T.Morgan, "The Thermal Rating of Overhead-Line Conductors. Part 1, The Steady-State Thermal Model", Electr. Power Syst. Res., Vol. 5, 1982, pp. 119-139.

[16] V.T. Morgan, *Thermal Behaviour of Electrical Conductors*, Research Studies Press (John Wiley, New York), 1990.

[17] V.T. Morgan, "Effect of Elevated Temperature Operation on the Tensile Strength of Overhead Conductors ", IEEE PES Winter Power Meeting, New York, January, 1995.

[18] V.T. Morgan and D.K. Geddey, "Temperature Distribution within Overhead ACSR Conductors", CIGRE, Paris, 1992, Paper 22-101.

[19] V.T. Morgan, "The Loss of Tensile Strength of Hard-Drawn Conductors by Annealing in Service", IEEE Trans.on Power Apparatus and Systems, Vol. PAS-98, 1979, pp. 700-709.

[20] R. Billington, C. Singh, "System Load Representation in Generating Capacity Reliability Studies, Part II; Applications and Extensions", IEEE Trans. on Power Apparatus and Systems, Vol. PAS-91, 1972, pp. 2133-2141.

[21] Environment Canada, "Principal Station Data", 1983.

[22] V.T. Morgan, "Statistical Distribution of the Temperature Rise of an Overhead-Line Conductor Carrying Constant Current", Electr. Power Syst.Res., Vol. 24, 1992, pp. 237-243.

[23] A.E. Kennelly, F.A. Laws, P.H. Pierce, "Experimental Researches on Skin Effect in Conductors", AIEE Trans., Vol. 34, 1915, pp. 1953-2021.

[24] A.E. Kennelly, H.A. Affel, "Skin-Effect Resistance Measurements of Conductors at Radio Frequencies up to 1000,000 Cycles per Second", Trans., Institute of Radio Engineers, New York, N.Y., 1916, pp. 523.

[25] J. Zaborszky, "Skin Effect and Spiralling in Stranded Conductors", Trans. AIEE, Vol. 72, Part III, August 1953, pp 599-603.

[26] H.B. Dwight, *Electrical Elements of Power Transmission Lines*, The Macmillan Company, New York, 1954.

[27] W.A. Lewis, P.D. Tuttle, "The Resistance and Reactance of Aluminum Conductors, Steel Reinforced", AIEE Paper 58-1029, Trans., III, 1958, Vol. 77, pp. 1189-1210.

[28] Aluminum Electrical Conductor Handbook, the Aluminum Association, Second Edition, 1982.

[29] V.T. Morgan, "Electrical Characteristics of Steel-Cored Aluminum Conductors", Proc. IEE, Vol. 112, No. 2, February, 1965.

[30] R.D. Findlay, "Analysis of Two Layer Aluminum Conductor Steel Reinforced", Paper C73 172-4, IEEE Winter Power Meeting 1973.

[31] R.D. Findlay and H. Riaz, "An Analysis of the Jarvis Crossing Conductor", Paper C72 191-0, IEEE Winter Power Meeting 1972.

[32] V.T. Morgan, "Some Factors Which Influence the Continuous and Dynamic Thermal Rating of Overhead-Line Conductors", CIGRE 06-85, 1985, Paper 230-08.

[33] V.T. Morgan, "The Current-Carrying Capacities of Overhead-Line Conductors", IEEE Paper A 78 575-3, IEEE PES Summer Meeting, 1978.

[34] S.D. Foss, S.H. Lin, R. Carberry, "Significance of the Conductor Radial Temperature Gradient Within a Dynamic Line Rating Methodology", IEEE Trans. on Power Delivery, Vol. PWRD-2, No. 2, April 1987.

[35] W.Z. Black, S.S. Collins, J.F. Hall, "Theoretical Model for Temperature Gradients Within Bare Overhead Conductors", IEEE Trans. on Power Delivery, Vol. 3, No. 2, April 1988.

[36] S. Conte, C. deBoor, *Elementary Numerical Analysis*, McGraw Hill, 1972.

[37] V.T. Morgan, "Rating of Bare Overhead Conductors for Intermittent and Cyclic Currents", Proc.IEE, Vol. 116, 1969, pp. 1361-1376.

[38] J.R. Harvey, "Effect of Elevated Temperature Operation on the Strength of Aluminum Conductors", IEEE Trans. on Power Apparatus and Systems, Vol. PAS-91, 1972, pp. 1769-1772.

[39] D.O. Koval, R. Billington, "Determination of Transmission Line Ampacities by Probability and Numerical Methods", IEEE Trans. on Power Apparatus and Systems, Vol. PAS-89, 1970, pp. 1485-1492.

IMAGE EVALUATION
TEST TARGET (QA-3)

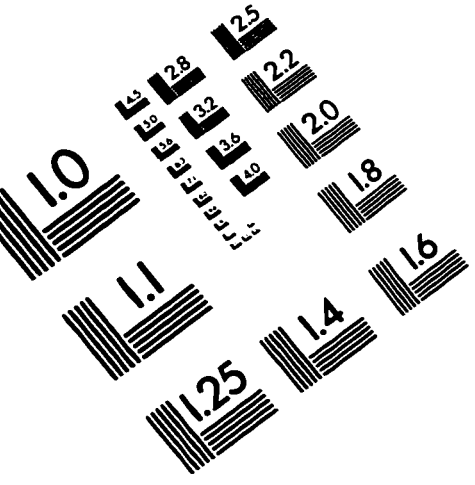

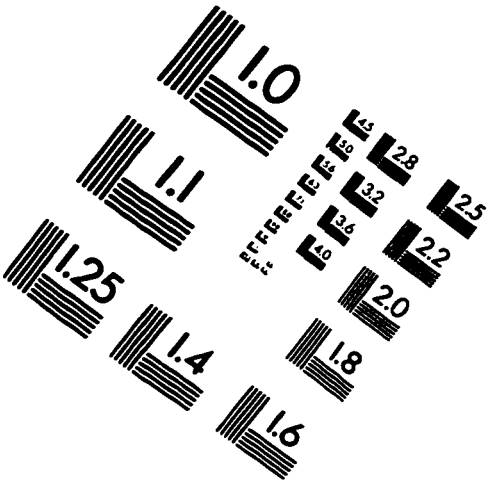

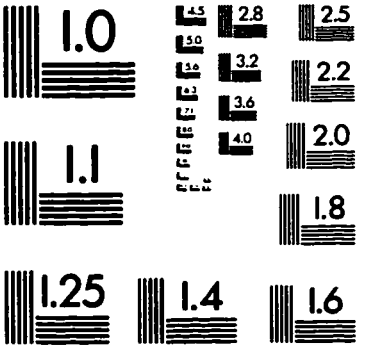

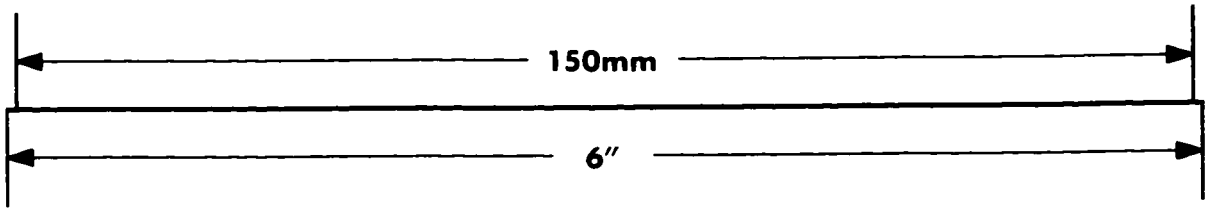

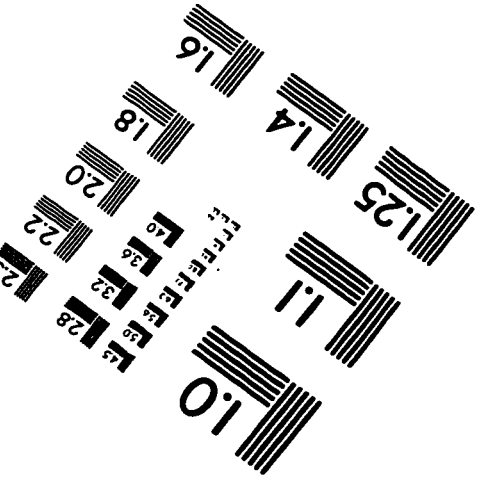

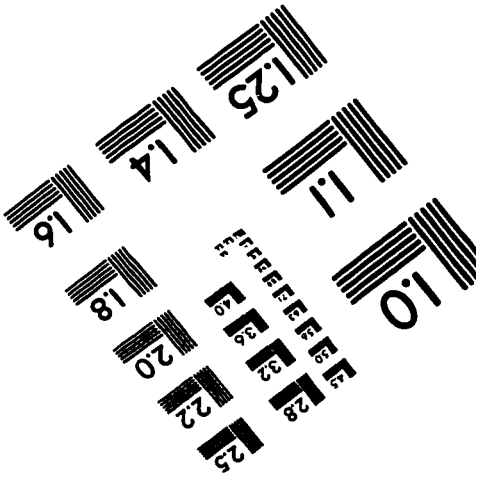

APPLIED IMAGE, Inc
1653 East Main Street
Rochester, NY 14609 USA
Phone: 716/482-0300
Fax: 716/288-5989